SAPIENZA
UNIVERSITÀ DI ROMA

Characterisation of SiPM detectors for dark matter detection with the liquid-argon time-projection chamber of the DarkSide prototype

Facoltà di Scienze Matematiche, Fisiche e Naturali

Corso di Laurea Magistrale in Fisica

Candidate

Ludovico Luzzi

ID number 1655136

Thesis Advisor

Prof. Valerio Ippolito

Academic Year 2019/2020

Thesis defended on 25 May 2020
in front of a Board of Examiners composed by:

(chairman)

Characterisation of SiPM detectors for dark matter detection with the liquid-argon time-projection chamber of the DarkSide prototype
Master thesis. Sapienza – University of Rome

This thesis has been typeset by LaTeX and the Sapthesis class.

Version: May 5, 2020

Author's email: Ludovico.Luzzi@roma1.infn.it

Contents

Introduction

About a century ago, astronomers speculated that non-baryonic and invisible matter existed in the entire electromagnetic spectrum: dark matter. The observations made to date indicate that dark matter constitutes approximately 86% of the mass of our universe; its presence determines in an extremely significant way the motion of galaxies and clusters of galaxies and therefore its role in the formation and evolution of the universe has become a paradigm in the field of cosmology.
On a galactic scale, astronomers are of the opinion that our galaxy is surrounded by an extended halo of dark matter. From a microscopic point of view, weakly interacting massive particles, the WIMPs, represent the most promising candidates for the role of non-baryonic dark matter particles, favored by different theories that go beyond the Standard Model, such as Supersymmetry (SUSY).
Direct revelation techniques today seem the most promising in highlighting the presence of dark matter in our galaxy and consist in the detection of nuclear recoil in the scattering process between a WIMP and a target nucleus. The number of events expected in such interactions is very low and this requires an in-depth study of the sources that generate background noise for this to be minimized. The residual noise is given by the contribution of cosmic neutrinos, neutrons and *gamma* rays coming from the surrounding environment and from the detectors themselves.

Liquid argon (LAr) is a particularly favorable target for the detection of WIMPs thanks to its excellent event discrimination capabilities. Scintillation light initiated by particles recoiling from atomic electrons (ER), the primary source of background in a WIMP direct detection experiment, has a time constant of approximately a microsecond. This is in stark contrast to the nanosecond time constant of scintillation light emitted during an expected WIMP-nuclear recoil event (NR). This effect has been exploited by the argon-based detector DarkSide-50 (DS-50) via pulse shape discrimination (PSD).
Since a detection of dark matter has not yet taken place, the race to carry out new generation experiments is very active today, leading to the building of detectors with tens of tonnes of active target mass. For this reason, a two-phase liquid argon time projection chamber of 20t active mass, capable of collecting an exposure of 200 t yr, has been proposed by the DarkSide Collaboration. This detector is called DarkSide-20k and it will be located at Laboratori Nazionali del Gran Sasso (LNGS). DS-20k is designed to operate with zero backgrounds, meaning that all sources of instrumental background are reduced to <0.1 events over a 200 t yr exposure is expected to operate in a so-called background free regime, so that a positive claim can be made with as few events as possible. During the total exposure, 3.2 nuclear

recoil events are expected from the coherent scattering of atmospheric neutrinos, making DS-20k the first ever direct dark matter detection experiment to reach this milestone.
One of the key parameters of DS-20k is light detection: DS-20k will use the Silicon PhotoMultipliers (SIPMs) instead of the standard PhotoMultipliers (PMTs). SiPMs have a number of performance advantages over traditional PMTs, including higher photon detection efficiency (PDE) and much better single- photon resolution, all while operating at much lower bias voltage. SiPMs can also be efficiently integrated into tiles that cover large areas and feature better radio-purity than PMTs. DS-20k photosensor unit is a Photo Detector Module (PDM), consisting of a tile of 24 SiPMs. The PDMs are assembled in a MotherBoard (MB), an array of 25 PDMs, and the DS project foresees a total of 344 MBs covering the top and bottom of the TPC.
To fully validate the new DS-20k technologies for their integrity in both mechanical and functional aspects, the DarkSide collaboration have planned to construct and test a prototype detector of intermediate size ($\sim$1 t), in a project called DS-Proto. The DS-Proto TPC mechanics, including the structural elements and the SiPM PDM assemblies will all be built utilizing, on a scaled down overall dimension, the same design and construction techniques foreseen for DS-20k. The prototype photosensors design consists of 250 PDM (top and bottom the TPC) contained in 10 MotherBoards.
Pending the construction of all the parts that will make up the final prototype, a small-sized TPC has already been built to test the optimization of the photosensors response to scintillation signals in liquid argon. Proto-0 with only one MB above the TPC anode has been built and is undergoing test in LAr, at CERN. A second MB will soon be installed under the cathode in order to carry out an even more accurate study of the ionization signal S_2.

My thesis work is discussed in chapters 5 and 6, regarding the study of the response of the SiPM constituting the PDMs of Proto-0 MotherBoard, for the calibration of these modules, a fundamental procedure since it will be applied to the thousands of photosensors of DarkSide-20k. The success of this operation is crucial for maximizing the efficiency of the detector to identify a WIMP signal. In November 2019, a data acquisition took place at CERN to test the response of the PDM to the scintillation pulses produced in liquid argon from gamma sources such as laser and ^{241}Am. The first step is to reconstruct the signal through an ARMA algorithm that filters the acquired waveforms and identifies the peaks corresponding to signal events. From the analysis of the signals produced by the laser source, a study is carried out aimed at optimizing the filter performance, so as to improve the reconstruction phase of the events: through a fit procedure, the parameters of the PDM response template are measured and an asses is performed on them by studying the *signal-to-noise ratio* (SNR) of all channels of the MotherBoard.
I therefore investigated the effect that the template parameters have on the signal charge measurement and on the reconstruction of the relative height (*prominence*) of the peaks by the algorithm. From the charge and prominence distribution I describe the procedure with which to extract the gain parameter and the average number of photoelectrons (*occupancy*) seen by each channel of the MB.
The *dark count rate* (DCR) is the main source of noise in a silicon photomultiplier

and depends on both the temperature and the bias voltage of each cell: through the calculation of the SNR it is possible to verify the growth of the DCR as the power supply voltage increases.
By accessing the data collected with americium it is possible to observe events characterized by the presence of signals S_1 and S_2. For the moment I have limited myself to the simple observation of these phenomena which will be studied in depth in the future.
In chapter 6 I wanted to validate the investigation performed on the data through a Monte Carlo simulation. The simulation allows the faithful reproduction of the response of a SiPM considering both the parameters of the template and the DAQ and the physical nature of the signal to be generated. The 25 channels of the Proto-0 MB are therefore simulated, creating laser-type events on which the fit procedures implemented on the data are applied, so as to measure the template parameters and the SNR. If the SNR level measured with the data is reproduced with the simulation, then the correct operation of the followed procedures is confirmed.
Finally, through simulation, I studied the efficiency of the peak finder algorithm both in identifying the hits over time, if they were very close to each other, and in reconstructing them at varying the minimum prominence threshold.

Chapter 1

The problem of the Dark Matter

The dark matter problem has its roots in the 1930s, but it's only from the 1970s that this issue becomes a real challenge for modern physics. Many problems, once separate from each other, were brought together and brought back to one and only anomaly: the missing mass in our universe.

1.1 The birth of the problem

At the beginning of the 20th century, physicists and astronomers tried to estimate the density of matter present in the universe.
Some objects can be detected as they emit electromagnetic radiation. The stellar mass density ρ_* in a portion of the universe is given by the relationship

$$\rho_* =< M/L_B > j_{*,B}. \tag{1.1}$$

where $j_{*,B}$ is the total luminosity density of stars emitted in the B-band ($4.0 \cdot 10^{-7}m < \lambda < 4.9 \cdot 10^{-7}m$) in that part, and $< M/L_B >$ is the $mass - to - light\ ratio$ for the stars in the considered zone[1].
Following theoretical considerations and experimental measurements, today the mass density of the stars in the universe is

$$\rho_{vis} =< M/L > J \approx 5 \cdot 10^8 M_{\odot} Mpc^{-3}. \tag{1.2}$$

Total density parameter Ω is defined as the dimensionless quantity $\Omega = \rho/\rho_c$, where ρ is the mass density of the universe, while ρ_c is the density of critical mass of the universe, equal $\rho_c = 3H_0/8\pi G$ (H_0 is the Hubble constant and G is the universal gravitation constant). The value of H_0 currently is estimated around $67.15km/s/Mpc$ and from this derives the current estimate of the critical mass density of the universe[1]

$$\rho_{c,0} = 1.4 \cdot 10^{11} M_{\odot} Mpc^{-3}. \tag{1.3}$$

The current density parameter of stellar mass is determined from the quantities (1.2) and (1.3)

$$\Omega_{vis,0} = \frac{\rho_{vis}}{\rho_{c,0}} \approx 0.004. \tag{1.4}$$

If we compare this value with the current total density parameter, which from recent measurements turns out to be $\Omega_0 \approx 1$ (flat universe), we can deduce that the stars constitute less than 0.5 % of the total density of the universe.
However, galaxies also contain baryonic matter that does not emit electromagnetic radiation in the visible spectrum, such as white dwarfs, brown dwarfs, black holes, interstellar gas, etc. The density of baryonic matter in the universe is therefore expected to be greater than the density of luminous objects only, and therefore $\Omega_{B,0} > \Omega_{vis,0}$. The estimates of $\Omega_{B,0}$ come from several independent methods. The most efficient is based on the primordial nucleosynthesis process: it is possible to determine the relative abundances of the elements present in the stellar nuclei by studying their production, which occurred through nuclear reactions in the primordial universe (nucleosynthesis). In-depth studies reveal that the current baryonic matter density parameter $\Omega_{B,0}$ is[1]

$$\Omega_{B,0} = 0.04 \pm 0.01. \tag{1.5}$$

From the observations just made it is therefore deduced that not only most of the baryonic matter is not visible, but even most of the matter that constitutes the universe is not even baryonic. It is non-baryonic dark matter, which does not absorb, emit or diffuse light of any wavelength.
One way to determine the presence of dark matter is to study the gravitational influence it has on visible matter. In the 1930s several physicists noticed an inconsistency between the velocity dispersion of galaxies observed in galaxy clusters and the same dispersion calculated on the basis of light matter. In the early 70s, some astronomers also found a strong discrepancy between the "flat" rotation curve observed for a spiral galaxy and the "decreasing" one expected on the basis of the motion of the stars that made it up. These results from two different branches of astronomy indicated unexpectedly large galactic masses, confirming the hypothesis of a preponderance of matter still unnoticed.

1.2 Rotation curves of spiral galaxies

To determine the presence of dark matter in the universe we can proceed with the observation of the orbital speeds of stars in spiral galaxies, such as the Milky Way or M31. Spiral galaxies have the shape of a flattened disk, with a spheroidal part in their center. The stars that are part of the disk have almost circular orbits around the center of the galaxy.
Consider a test star that describes a circular orbit around the center of the galaxy it is part of. If the radius of the orbit is R and the orbital velocity is v, then the star is subjected to an acceleration

$$a = \frac{v^2}{R} \tag{1.6}$$

headed for the center of the galaxy. If this acceleration is caused by the gravitational actraction of the galaxy, then

$$a = \frac{GM(R)}{R^2}, \tag{1.7}$$

where $M(R)$ is the mass contained in the sphere of radius R centered in the center of the galaxy. By equating the expressions (1.7) and (1.8) we obtain the relationship between v and $M(R)$

$$\frac{v^2}{R} = \frac{GM(R)}{R^2} \Rightarrow v = \sqrt{\frac{GM(R)}{R}}. \tag{1.8}$$

Brightness is defined as the energy collected per unit of time, surface, frequency and solid angle around the direction of origin and it is used in the case of radiation from extended sources (eg galaxies, interstellar medium). The surface brightness I of a spiral galaxy in general has an exponential dependence on the distance from the center:

$$I(R) = I(0)e^{-\frac{R}{R_s}}, \tag{1.9}$$

with scale length R_s in the order of a few kpc (for our galaxy $R_s \approx 4kpc$, while for M31 and other larger galaxies $R_s \approx 6kpc$). If it is assumed that the average density in a certain region of the galaxy is proportional to $I(R)$ at that point, then it is already at a distance R^* equal to some R_s the mass of the stars present in R^* can be approximated to a constant. So if the stars were the only contribution to the mass of the galaxy, the velocity would decrease as $v \propto 1/\sqrt{R}$ with increasing R (Keplerian rotation). The trend of the velocity of the stars constituting a galaxy as a function of the orbital radius is called the textit rotation curve of the galaxy.
The rotation curve of a galaxy can be determined on the basis of direct observations [1]. The first astronomer to measure the orbital velocities of the stars of the M31 galaxy was Vesto Slipher in 1914, through the redshift of the stellar spectra, taking into account the relative speed of the galaxy with respect to the solar system. However, given the difficulty in measuring low surface brightness spectra, the orbital velocity measurements v could therefore not be accurate for $R > 3R_s = 18kpc$. In 1970 Vera Rubin and Kent Ford studied emission lines from hot ionized gas regions in M31, managing to determine $v(R)$ up to $R = 24kpc = 4R_s$. Their results showed no Keplerian decrease in orbital velocity. In 1975 M.Roberts and R.Whitehurts, studying the emission line at $\lambda = 21cm$ of the neutral hydrogen present at $R > 4R_s$, found that at $R \approx 30kpc \approx 5R_s$ the orbital velocity remained at the almost constant value $v(R) \approx 230km/s$ (fig.1.1). Since the orbital velocity of gas and stars at large distances ($R > 3R_s$) turns out to be greater than what would be had if stars and gas were the only matter present, it can be deduced the presence of a halo of dark matter that encompasses the visible galaxy. The mass of this *dark halo* represents the gravitational anchor necessary to hold together gases and stars having such a high orbital speed.
M31 is not the only spiral galaxy to have this characteristic; most spiral galaxies have highlighted the presence of dark matter halos. Measurements carried out on thousands of cases reveal values of $v(R)$ which remain constant for $R > R_s$. Our galaxy also has an orbital velocity that seems to grow slightly compared to the Keplerian one, for $R > 15kpc$[1].

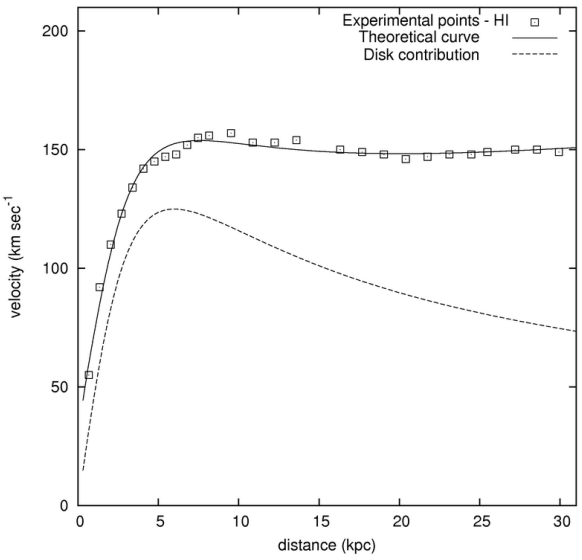

Figure 1.1. Comparison between the rotation curve expected for the spiral galaxy NGC 9831 and the rotation curve obtained from direct measurements[1].

1.3 Velocity dispersion in galaxy clusters

The first astronomer to devote more attention to the case of the existence of dark matter in the universe was Fritz Zwicky in the 1930s. When studying the galaxy cluster of Coma, it was noted that the radial velocity dispersion of the cluster galaxies was very large (around 1000 km/s) and the stars and visible gas present in the galaxies were not able to gravitationally hold the whole cluster together. For this to be possible, Zwicky concluded that the cluster had to contain a large amount of dark matter.
Zwicky's reasoning was as follows. Suppose that a cluster of galaxies consists of N galaxies, each of which has a point mass m_i $(i = 1.2, ..., N)$, a position $\vec{x_i}$, and a speed at $\dot{\vec{x}}_i$. The galaxies within a cluster move with non relativistic velocity and it is for this reason that we can study the dynamics of the Coma cluster, and of other clusters, through Newtonian dynamics. The acceleration of the i -th galaxy in the cluster is given by the Newtonian formula

$$\ddot{\vec{x}}_i = G \sum_{i \neq j} m_j \frac{\vec{x_j} - \vec{x_i}}{|\vec{x_j} - \vec{x_i}|^3}. \tag{1.10}$$

Equation (1.11) assumes that the cluster is an isolated system and therefore the contribution to gravitational acceleration due to other distant clusters is neglected. *The gravitational potential energy* of a system of N galaxies is

$$W = -\frac{G}{2} \sum_{i,j(i \neq j)} \frac{m_i m_j}{|\vec{x_j} - \vec{x_i}|}, \tag{1.11}$$

which, for a spherical symmetry system, can also be written in the form

$$W = -\alpha \frac{GM^2}{r_h}, \tag{1.12}$$

where $M = \sum m_i$ is the total mass of all galaxies in the cluster, α is a numerical factor of the order of unity ($\alpha \approx 0.4$ for many observed clusters) which depends on the density of the cluster, and r_h is the *half - mass* radius of the cluster (radius of a sphere centered in the center of the cluster containing a mass equal to $M/2$).
The kinetic energy associated with the relative motion of galaxies in the cluster is

$$K = \frac{1}{2} \sum_i m_i |\dot{\vec{x}_i}|^2, \tag{1.13}$$

which can be rewritten as

$$K = \frac{1}{2} M < v^2 >, \tag{1.14}$$

where

$$< v^2 > \equiv \frac{1}{M} \sum_i m_i |\dot{\vec{x}_i}|^2 \tag{1.15}$$

is the mean quadratic velocity of all galaxies in the cluster.
The *moment of inertia* of the cluster is defined as

$$I \equiv \sum_i m_i |\vec{x_i}|^2. \tag{1.16}$$

We now introduce an important relationship, known as *virial theorem*, according to which

$$\ddot{I} = 2W + 4K. \tag{1.17}$$

It perfectly applies to a self-gravitating system of point masses and is particularly useful if applied to static systems, with a constant moment of inertia. If $I = constant$, the virial theorem in the *stationary case* is

$$0 = W + 2K \Rightarrow K = -\frac{W}{2}. \tag{1.18}$$

Substituting equations (1.13) and (1.15) now in equation (1.19) we obtain

$$\frac{1}{2} M < v^2 > = \frac{\alpha}{2} \frac{GM^2}{r_h}. \tag{1.19}$$

We can therefore use the virial theorem to estimate the mass of a cluster of galaxies:

$$M = \frac{< v^2 > r_h}{\alpha G}. \tag{1.20}$$

In the case of Coma $< v^2 > = 2.32 \cdot 10^6 Km^2 s^{-2}$ and $r_h \approx 1.5 Mpc \approx 4.6 \cdot 10^{24} cm$, and it's therefore possible to estimate the mass of the whole cluster[1]:

$$M_{Coma} = \frac{< v^2 > r_h}{\alpha G} \approx \frac{(2.32 \cdot 10^{12} m^2 s{-}2)(4.6 \cdot 10^{22} m)}{(0.4)(6.67 \cdot 10^{-11} m^3 s^{-2} kg{-}1)} \approx 4 \cdot 10^{45} kg \approx 2 \cdot 10^{15} M_{\odot}. \tag{1.21}$$

It is therefore, on the basis of experimental measurements [1], that less than 2% of the mass of Coma is made up of stars ($M_{Coma,*} \approx 3 \cdot 10^{13} M_{\odot}$), and only 10% consistes of intergalactic hot gas ($M_{Coma,gas} \approx 2 \cdot 10^{14} M_{\odot}$). From this we can deduce, as Zwicky did in his time, that most of the mass that constitutes the Coma cluster is dark matter.
Between the 1950s and 1960s several studies were conducted, based on Zwicky's work, on many other galaxy clusters, and all resulted in an obvious mass discrepancy between expected values and experimental observations. It was concluded that generally a regular galaxy cluster is basically made of dark matter.

1.4 Gravitational lensing

So far, I have illustrated the classical methods for detecting dark matter by its gravitational effects on luminous matter.
However, as Einstein understood, dark matter would impact not just the direction of matter, but also the motion of photons. Dark matter can bend and concentrate light, acting like a *gravitational lens*. The effects of dark matter on photons have been used to search for dark matter in the halo of our own Galaxy, as well as in distant clusters of galaxies.
Let's assume that Milky Way is surrounded by a dark matter halo. Some of this invisible matter might consist of massive compact objects such as brown dwarfs, white dwarfs, neutron stars, and black holes. These objects have been collectively called MACHOs, an acronym for MAssive Compact Halo Objects. If a photon passes such a compact massive object at an impact parameter b, as shown in Figure 1.2, the local space-time curvature would allow the photon to be deflected by an angle

$$\alpha = \frac{4GM}{c^2 b}, \tag{1.22}$$

where M is the mass of the compact object.
Since a star, or a brown dwarf, can deflect light, it can acts as a lens. Suppose a MACHO in the halo of our Galaxy passes between an observer in the Milky Way and a star in the Large Magellanic Cloud. Figure 1.3 shows this situation: MACHO is halfway between the observer and the star. As the MACHO deflects the light from the distant star, it creates an impression of the object that is both warped and intensified. If the MACHO is precisely along the line of sight between the viewer and the lensed star, the generated picture is a perfect ring, with angular radius

$$\theta_E = \left(\frac{4GM}{c^2 d} \frac{1-x}{x} \right)^{1/2}, \tag{1.23}$$

where M is the mass of the lensing MACHO, d is the distance from the observer to the lensed star, and xd (where $0 < x < 1$) is the distance from the observer to the MACHO. The angle θ_E is the *Einstein radius*.

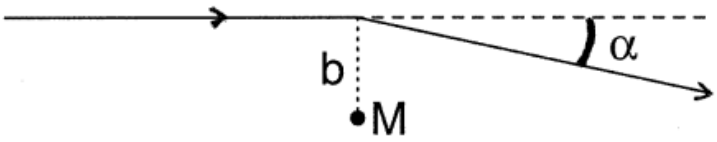

Figure 1.2. Deflection of light by a massive compact object.

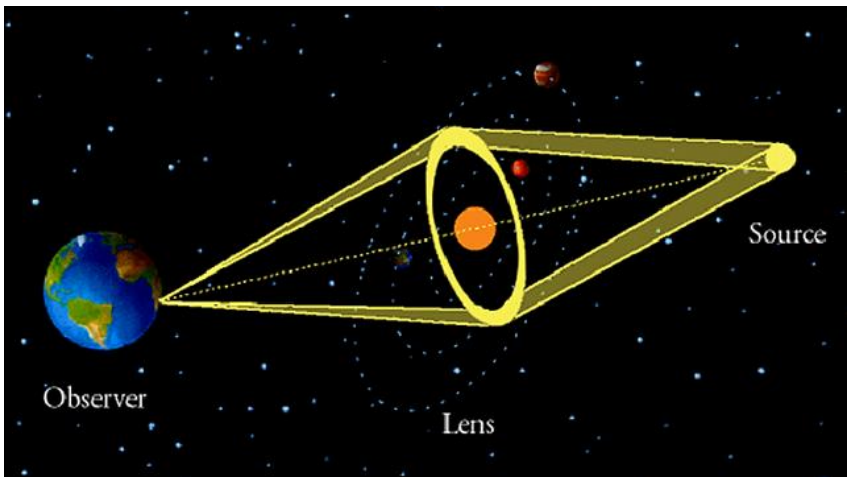

Figure 1.3. Comparison between the rotation curve expected for a spiral galaxy and the rotation curve obtained from direct measurements[2].

If the MACHO does not lie perfectly along the line of sight to the star, then the image of the star will be distorted into two or more arcs instead of a single unbroken ring.
Since the Einstein radius of the LMC star lensed by the MACHO is too small to be determined, it's possible to observe an increase of the flux of the light. To order for the amplification to be important, the angular gap between the MACHO and the lensed light, as seen from Earth, must be similar to, or smaller than, the Einstein radius.
In order to detect MACHO lens, various research group have monitored millions of stars in the LMC to observe changes in their flux. Due to the constant relative motion between stars in the LMC and MACHOs in our dark halo, the usual signature of a "lensing event" is a star that becomes brighter as the angular distance between the two objects decreases, then becomes faint as the angular distance increases again. This distance is equal to θ_E as seen from Eart, and the typical time scale for a lensing event is the time takes a Macho to travel through it. More massive MACHOs generate larger Einstein rings and thus will amplify the lensed star for a longer time. The total number of lensing events which research groups detected suggest that

as much as 20% of the halo mass could be in the form of MACHOs. However it's possible that a certain quantity of the observed lensing events could be due to lensing objects within the LMC itself.
Anyway, the search for MACHOs suggests that most of the matter in the dark halo of our galaxy is due to a smoothly distributed component, instead of being congealed into MACHOs of roughly stellar mass.

1.5 Cosmological evidence

Dark matter evidences are such that the most accepted model that describes our interpretation of the origin of the Universe -the Lambda Cold Dark Matter (ΛCDM) model- includes dark matter as a main component: Λ refers to the cosmological constant (i.e. the energy density or the dark energy of the vacuum) and " Cold Dark Matter" accounts for slowly flowing particles that compensate for the variety of cosmological measurements that suggest the existence of *missing mass*.
Established in the late 1990s this hypothesis is the simplest parametrization of the Big Bang cosmological model that is largely compatible with many observations, including the presence and properties of the Cosmic Microwave Background (CMB), the large - scale galaxy distribution structure, the abundance of hydrogen (including deuterium), helium and lithium, and the rapid expansion of the universe observed in the light from distant galaxies and supernovae.
According to this hypothesis, the structures that arose in the early Universe are generated by the clustering of a non-interacting, slow-moving and undetected part of matter[4], typically referred to as Cold Dark Matter. The assumption that dark matter interacts only by gravitational force (or by very weak one) means that it began to collapse gravitationally earlier in cosmic time than baryonic matter. After they were docoupled baryons fall into the gravitational wells created previously by DM structers. Without dark matter, the baryonic matter in the Universe could not have enough time to collapse to form the range of gravitationally bound objects that we see today[4, 5].
A especially important technique for determining the contribution of dark matter to the energy balance of the Universe is the measurement of the temperature anisotropies of CMB photons (electromagnetic radiation left over from the early stage of the universe in Big Bang cosmology), observed today at a mean temperature of $2.726 \pm 0.010K$. While the CMB is mainly isotropic, demonstrating that the universe is mostly homogeneous, minor anisotropies are present almost exclusively due to the temperature fluctuations in the early universe caused by under -and over-density in various regions as particles began to freeze out at different times. The intensity and magnitude of these variations depend largely on the different elements and species present at the time, making the CMB susceptible to the quantity of dark matter present in the early universe. The Planck experiment measured the angular power spectrum of these CMB temperatures anisotropies: the amplitude of the power spectrum at various values of l, the angular size (π/l) of a given spherical harmonic, provides a quantitative measurement of anisotropies in the CMB, which enables the determination of the relative abundance of different types of particles in the universe after freezing, as well as several other properties (figure 1.4 shows the

2018 results of these measurements, as well as the best fit using the six parameters ΛCDM model, while in Tab. 1.1 the obtained Cosmological parameters - see Ref. [[3], Planck 2018 results]).

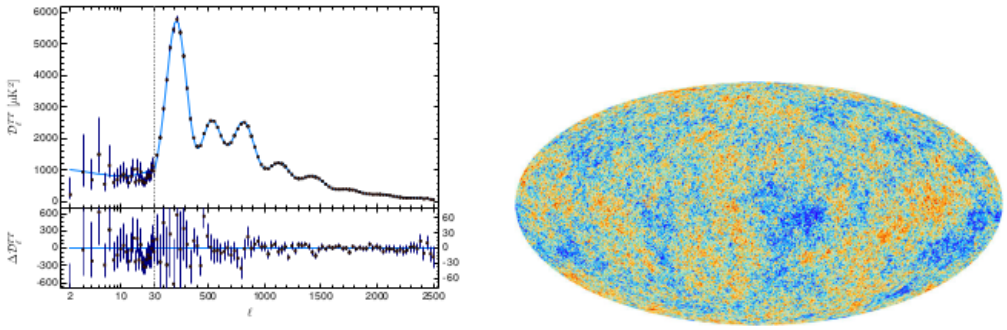

Figure 1.4. *Left*: Angular power spectrum of CMB temperature anisotropies as measured by the Planck satellite (2018). Data are shown as blue points with the best fit ΛCDM cosmological model shown as a red line. *Right*: Cosmic Microwave Background as observed by the Planck satellite. Figures from Ref. [3]

Parameter	68% limits
H_0[km s^{-1}Mpc^{-1}]	67.66 ± 0.42
Ω_Λ	0.6889 ± 0.0056
Ω_m	0.3111 ± 0.0056
$\Omega_b h^2$	0.02242 ± 0.00014
$\Omega_c h^2$	0.11933 ± 0.00091

Figure 1.5. Density parameters (Ω_-) of dark energy/cosmological constant (Λ), baryonic (b) and cold dark matter (c) components with Hubble parameter as $h = H_0/(100 kms^{-1}Mpc^{-1}$); Planck Collaboration (2018 results) [[3], Table 2.].

The succes of the ΛCDM model is also attributed to the effects of the so-called N-body simulations, computational simulations that include a huge number of particles interacting according to simple physical laws and are used to monitor the evolution of the system in the Universe: millions of particles are formed according to the initial density distribution and are allowed to interact according to the laws of gravity. Simulation can control the growth of the structures in the system model. Based on the initial density distribution and the cosmological parameters selected, various structures emerge at different stages of evolution. Consistent picture has appeared from a variety of N-body simulations: the distribution of galaxies observed in large scale systems matches that expected by N-body simulations over a wide range of distance scales[6]. In addition, simulations have started to precisely replicate the observed populations of elliptical and spiral galaxies[7], like the Milky Way[8]. This ability of simulations containing DM to reproduce the structures observed in the Universe is further strong evidence in support of the DM paradigm.

Chapter 2

Dark Matter direct search

The existence of dark matter in the Universe is commonly accepted as the explanation of many astrophysical and cosmological phenomena I just discussed. It is accepted today in the scientific community that roughly 85% of the matter in the universe is in some non-baryonic form that neither emits nor absorbs electromagnetic radiation. Alternatives, such as theories involving modifications to Einstein's theory of gravity, have not been able to explain the observations across all scales. A favored hypothesis that explains these observations is that dark matter is made of weakly interacting massive particles (WIMPs). However, no such particles exist in the Standard Model and none have been directly observed at particle accelerators or elsewhere.
Hence the nature of the dark matter remains unknown.

2.1 The WIMP solution

According to the *Supersymmetric Model* (SUSY, *supersimmetry*)[24] our galaxy is surrounded by an extensive halo of WIMP (*Weakly Interacting Massive Particles*), elementary particles massive ($\approx 100 GeV/c^2$) that interact with other particles only through the force of gravity and a force of intensity very weak and therefore they are very difficult to detect. WIMPs belong to the category of "cold" dark matter, particles that have decoupled from the thermal equilibrium of the primordial universe in a non-relativistic regime. And it is for reasons of compatibility with the cosmological structures that are observed today on a very large scale that WIMPs are considered the main candidate for dark matter.
The techniques of direct revelation seem today the most promising in highlighting the presence of dark matter in the Milky Way. The basic idea is quite simple: if WIMPs permeated the galaxy, then many of them should cross the Earth making their revelation possible by interacting with ordinary matter particles. The experiments that take place in this field consist in measuring the recoil energy of the nuclei in the scattering processes that take place between WIMP and matter. Scattering processes can be classified into two categories: *elastic scattering* and *inelastic scattering*[22]. The first is to hit a WIMP with the entire target core recoiling. The second is instead characterized by the interaction between WIMP and nucleus: the latter, after the collision, is in an excited state and subsequently emits a photon of certain energy. The following only analyzes the case of *elastic scattering*.

The number of scattering events in the unit of time R depends on the local density ρ_0 and the velocity distribution at $f(v)$ of the WIMPs in the Milky Way, from the mass m_χ of the WIMP in question, and from the cross section $\sigma_{\chi n}$ in the target WIMP-core interaction[14]:

$$R \propto N_t \frac{\rho_0}{m_\chi} \sigma_{\chi n} < v > \equiv R_0, \tag{2.1}$$

where N_t is the number of nuclei in the target and $< v >$ is the average speed of the WIMP in the laboratory reference system , given by the expression $< v >= \int_0^\infty v f(v) dv$. You can rely on the following estimates of density and average speed[14]:

$$\rho_0 \approx 0.3 GeV/cm^3 \tag{2.2}$$

$$< v > \approx 270 km/s. \tag{2.3}$$

Most theoretical models predict a cross section of less than $10^{-42} cm^2$ (until $10^{-48} cm^2$) for almost all possible WIMP masses (fig.2.1).

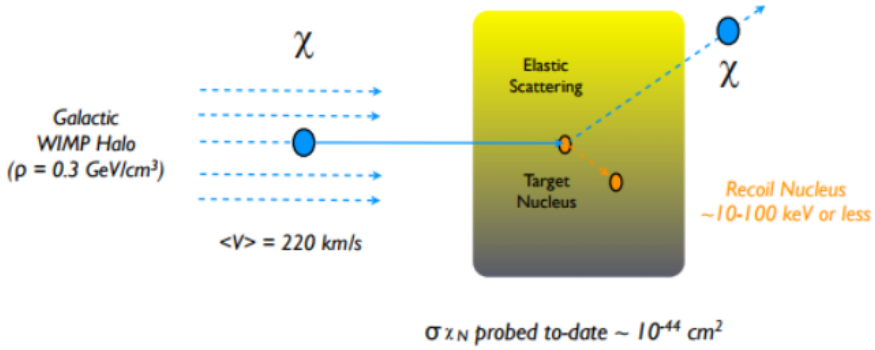

Figure 2.1. WIMP Elastic scattering Scattering on a target nucleus.

The differential event rate calculated with respect to the recoil energy E_r, considering that only $< v >$ depends on E_r, is:

$$\frac{dR}{dE_r} \propto N_t \frac{\rho_0}{m_\chi} \sigma_{\chi n} \frac{d}{dE_r} < v > . \tag{2.4}$$

In order to calculate the value of $\frac{dR}{dE_r}$, it is necessary to make some corrections to the expression (2.4) first, based on the following considerations:
1. integration limits for $< v >$ are actually to be considered v_{min} and v_{esc}, and represent respectively the lower and upper limits for the speed. v_{esc} is the escape velocity of the WIMP from the halo, it depends on the properties of the halo itself and usually $498 km/s < v_{esc} < 608 km/s$. v_{min} is the minimum speed of the WIMP to produce recoil energy E_r detectable. If we consider the collision between WIMP χ and nucleus N as a non relativistic collision, the expression of the recoil energy in the laboratory reference system turns out to be:

$$E_r = \frac{\mu^2 v_\chi^2 (1 - \cos\theta)}{m_N}, \tag{2.5}$$

where m_N is the mass of the target nucleus, v_χ is the WIMP speed, $\mu = \frac{m_\chi m_N}{m_\chi + m_N}$ is the reduced mass and θ is the angle between the direction of $\vec{v_\chi}$ and the horizontal axis. Equation (2.5) takes its maximum value for $\cos\theta = -1$ ($\theta = \pi$):

$$E_r^{max} = \frac{2\mu^2 v_\chi^2}{m_N}, \tag{2.6}$$

from which it is obtained

$$v_{min} = \sqrt{\frac{E_r^{max} m_N}{2\mu^2}}, \tag{2.7}$$

which represents the expression of the minimum speed that WIMP can assume. If we consider, for example, a mass WIMP $m_\chi = 100 GeV/c^2$ and speed $v_\chi = 300 km/s$, a mass xenon nucleus $m_N \approx 122 GeV/c^2$ will be spread with maximum energy $E_r^{max} = 49.5 keV$, obtained from the relation (2.6). The expression of $\frac{dR}{dE_r}$ therefore becomes

$$\frac{dR}{dE_r} \propto N_t \frac{\rho_0}{m_\chi} \sigma_{\chi n} \frac{d}{dE_r} \int_{v_{min}}^{v_{esc}} v f(v) dv; \tag{2.8}$$

2. to calculate the differential rate it is necessary to know the velocity distribution function at $f(v)$. If we assume the model of *isothermal sphere halo*, $f(v)$ has a Maxwellian trend

$$f(v) = \frac{1}{\sqrt{2\pi} v_0} e^{-v^2/v_0^2}. \tag{2.9}$$

of amplitude $v_0 = \frac{K_B T}{m_\chi}$, where $K_B = 8.6167 \cdot 10^{-5} eVK$ is the Boltzmann constant and T is the temperature in kelvin. If we consider the expression (2.9) and if we assume for semplicity $E_r = 2\mu^2 v^2 / m_N$[22], defining the characteristic energy of WIMP $E_0 = m_\chi v_0^2/2$ and the amount $k = 4\mu/(m_\chi + m_N)$, the differential event rate is found to depend exponentially on E_r:

$$\frac{dR}{dE_r} \approx \frac{R_0}{kE_0} e^{-E_r/kE_0}, \tag{2.10}$$

where R_0 is given by equation (2.1);

3. we consider the dynamics that characterizes the motion of the Earth in the Milky Way. The motion of the Earth with respect to the galaxy is due both to the motion of the Sun with respect to the galactic center and to the motion of the Earth with respect to the Sun; this involves both a seasonal variation in the event rate and an asymmetry in the direction of the signal. These observations lend to the correction of the equation by adding two constants that are determined experimentally;

4. until now the target nucleus has been considered as a point object, but it has an internal structure whose effect cannot be neglected. We then introduce the form factor $F(E_r)$, and the final equation turns out to be:

$$\frac{dR}{dE_r} = c_1 \frac{R_0}{kE_0}(F(E_r))^2 e^{-c^2 E_r/kE_0}. \tag{2.11}$$

Figure 2.2 shows the trend of the total rate of events expected for some types of target material.

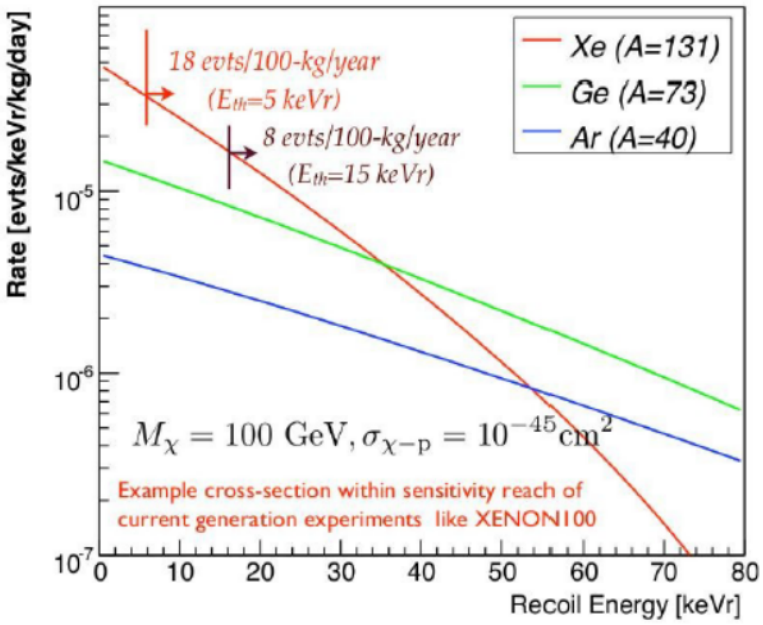

Figure 2.2. Scattering rate for a mass WIMP $m_\chi = 100GeV$ and cross section $\sigma_{\chi n} = 10^{-45} cm^2$[15].

Scattering processes can be divided according to another criterion with respect to the classification discussed above: *spin independent scattering* and *spin dependent scattering*[22]. In the case of *spin-independent scattering* the cross section increases drastically with the mass of the target nuclei (proportional to A^2, with A nucleus mass number) and typically dominates the scattering dependent on spin in experiments that use targets made up of very heavy atoms. As for the *spin-dependent scattering*, the cross sections that characterize the WIMP-nucleon interactions are proportional to $J(J+1)$, where J is the quantum number currently associated total angular of the target nucleus, and, contrary to the previous case, do not depend on the mass number of the nucleus; in this case the use of heavy nuclei does not guarantee an increase in the number of events. Spin dependency can be verified by choosing targets with different spins.

2.2 Annual modulation

The annual modulation is a marking - originally suggested in the mid-80s - independent of theoretical models hypothesized a priori, and has the purpose of giving an answer on the presence of dark matter particles in the galactic halo.
As a consequence of the revolution of the Earth around the Sun, which in turn moves in the Milky Way, the Earth itself should be crossed by a large flow of WIMPs which changes cyclically every year. In particular, the flow is maximum around June 2, when the component of the speed of the Earth parallel to the speed of the Sun in the galactic reference is maximum, and decreases until it reaches the minimum six months later, around December 2nd. The marking of the annual modulation is very distinctive and extremely effective since the effect induced by the dark matter particles must satisfy many requirements at the same time:

1. the counting rate must vary cyclically in accordance with a cosine-type function;
2. must vary with period of one year;
3. must have a maximum around June 2nd;
4. must only concern particles that release little energy into the detector, as WIMPs do;
5. must concern only the events in which only one of the detectors of the apparatus produces a signal, since the probability that a dark matter particle interacts with multiple detectors is negligible.

All this makes this strategy very competitive, as long as you carry out a large mass experiment, high radiopurity and with a high control of the measurement conditions.

2.3 Experiments

WIMP-nucleus interactions are characterized by small recoil energies and, as seen above, by a very reduced cross section. These two factors mean that, for equation

(2.11), the expected number of events is very limited. The direct detection of WIMP therefore requires that very massive detectors are used and that the experiments take place in a context in which the signals due to the background are as small as possible. The main component of the background events are cosmic rays and to minimize this noise all direct detection experiments are located in underground laboratories. The remaining background is made up of neutrons and γ rays coming from the surrounding environment and from the detectors themselves: to suppress the external background, a passive screen is positioned around the detector, while materials of high radiopurity are used for its construction. in order to minimize the dangerous internal noise. Despite the precautions that can be taken to avoid contamination, in all cases a residual background remains. It is therefore necessary to adopt discrimination techniques to separate the background from the signal, taking advantage of the different response of the detectors to particles of different nature.
For a WIMP with a mass between 1 and 1000 GeV/c^2, the typical recoil energy of the atomic nucleus is in the range $1 - 100keV$. The nuclear recoil energy can then be converted into thermal motion (phonons), ionization or scintillation of photons. For example, semiconductor detectors can detect electrons from the ionization of heavy ions and, if operating at extremely low temperatures, they can be used as bolometers for the measurement of phonons produced by atomic collisions. Experiments that simultaneously reveal two types of signals are typically more efficient in differentiating the nuclear recoil signal from background events.
What is discussed below is based on Ref.[24].
The use of *noble gases* is the most promising technique for the construction of large mass detectors. The target is constituted for example by Xe, Ar or Ne in liquid phase (detectors with *single phase*) or in liquid and gaseous phase (detectors with *double phase*). The dual phase dark matter detectors based on the use of xenon have reached a remarkable level of development in direct detection technology, managing to push the sensitivity of the spin independent elastic scattering to a wide range of WIMP masses, above $5GeV/c^2$. Natural xenon does not have very long-lived radioactive isotopes, except for ^{136} Xe, of which the double-beta decay represents a negligible contribution in the current generation of experiments. The aim of this type of experiments, the first of which was XENON10, is to reveal the charge and the small light signal emitted following an interaction between a dark matter particle and a xenon nucleus in a time projection chamber (TPC) double phase, liquid-gas.

Today there is a continuous and heated competition between experiments that use xenon. LUX, an experiment using $250kg$ of xenon, located in the USA, started data acquisition in 2013 and ended it in May 2016. Combining the data taken in 95 days in 2013 and the data taken in 332 days since 2014 as of 2016, the experiment reported a minimum in the exclusion limit of the WIMP-nucleon cross section equal to $1.1 \cdot 10^{-46} cm^2$ at a mass of WIMP equal to $50GeV/c^2$. The PandaX-II experiment, located in the JinPing underground laboratory (CJPL), China, is characterized by the largest detector in the world that uses dual-phase xenon. The results were obtained following a total exposure of $3.3 \cdot 10^4 kg \cdot d$, with an unprecedented background level of $2 \cdot 10^{-3}$ events $kg^{-1}d^{-1}keV^{-1}$ in the energy region between 1.3 and 8.7 keV. The lowest exclusion limit obtained for the cross section is $2.5 \cdot 10^{-46} cm^2$

at a mass of WIMP of $40 GeV/c^2$. PandaX-II will continue the data collection until 2018. Among the other experiments that exploit the xenon in the liquid and gas phase we can mention XENON100, located in the Gran Sasso National Laboratories (LNGS), in Italy, and XMASS, in the Kamioka mine, Japan.

Argon is another noble element used in large mass direct WIMP detection experiments. Compared to xenon, due to its very low cost, argon can be used for the construction of even more massive detectors (argon detectors of a few hundred tons will be built in the near future). The DarkSide-50 experiment placed at LNGS uses a dual phase argon detector. For detectors that use natural argon, ^{39}Ar represents an irreducible and very long-lived background signal. To reduce this disturbance, the DarkSide initiated the extraction of underground Argon, showing that the level of ^{39}Ar can be reduced by a factor of $1.4 \cdot 10^3$. A limit on spin-independent DM-nucleon scattering was derived asssuming the standard isothermal WIMP halo model ($v_{esc} = 544 km/s$, $v_0 = 220 km/s$, $v_{Earth} = 232 km/s$, $\rho_{DM} = 0.3 GeV/c^2 cm^3$). The result is obtained background free with a 90% C.L. and it corresponds to an upper limit on the spin-independent scattering cross-section at $1.14 \cdot 10^{-44} cm^2$ ($3.79 \cdot 10^{-44} cm^2$, $1.10 \cdot 10^{-44} cm^2$) for 100 Gev/c^2 (1 Tev/c^2, 126 Gev/c^2) dark matter particles (fig. 2.6)[42]. Another significant result obtained with DarkSide-50 is the ability to explore the mass range below 20 Gev/c^2, performing an analysis based only on the ionization signal. Light WIMPs, with masses down to 1.8 GeV/c^2, produce low energy nuclear recoils for which detection efficiency for scintillation signals (S_1) is very low. On the contrary, exploiting the gain due to the electroluminescence mechanism, it is possible to detect ionization signals (S_2). The outcome of this "S_2-only" analysis is a 90% C.L. exclusion limit above 1.8 GeV/c^2 for the spin-independent cross section of WIMPs on nucleons (fig. 2.5), extending the exclusion region for dark matter below previous limits in the range 1.8-6 GeV/c^2[42].

DEAP-3600 at SNOLAB in Sudbury, Canada is another experiment that uses argon, but unlike Darkside it operates in a single phase.
The *scintillation experiments* constitute another area of great interest in the direct detection of WIMP: dark matter particles interact with crystals such as NaI, CsI, CaF_2 or with noble gases in phase liquid such as Xe, Ar, Ne, inducing the emission of photons that can be detected by photomultipliers. Experiments of this type are DAMA, NAIAD, ANAIS, KIMS and DEAP.

An important frontier in the direct detection of dark matter is the search for WIMP in the range of some GeV/c^2, with the production of a rather low recoil energy. The key problem in carrying out these experiments is the use of detectors with a very low threshold energy, hundreds of eV or less. This is the case of *cryogenic experiments*, in which crystals of Ge, Si, Al_2O_3 or TeO_2 are used kept at low temperatures. The interactions of the WIMPs with the targets generate heat and the small temperature variations can be measured to obtain an indication of the energy involved in the observed event. It is also possible to use the same crystal simultaneously as a bolometer and as a solid state detector (or scintillator): as a bolometer it is able to measure all the energy of the particles, while as a solid state detector it only reveals the energy lost by ionization. The SuperCDMS experiment, conducted in the

Soudan mine in Minnesota, USA, uses cryogenic semiconductor detectors equipped with the iZIP (interleaved Z-sensitive ionization phonon), a technique capable of simultaneously detecting phonon and ionization signals at low temperatures of ≈ 40-50mK. SuperCDMS collaboration published the results of the experiment in 2014 with the use of 15 iZIP modules, each with a mass of $0.6kg$. The minimum cross section to be excluded has been reached for WIMP with mass between 1.6 and 5.5 GeV/c^2. The CRESST experiment, located at LNGS, uses crystal modules $CaWO_4$ operating at extremely low temperatures (10mK) to reveal together the thermal excitations and the scintillations resulting from nuclear recoils. The CRESST-II experiment, which ended in 2015, extended the cross section limit for WIMP masses below 1 GeV/c^2. Other experiments for the detection of low-mass WIMP include CDEX, located in the CJPL laboratories, and CUORE, located at the LNGS.

A category of experiments of considerable importance is finally represented by the *supercooled liquid detectors*. At SNOLAB, the PICO experiment operates through the bubble chamber technique: the detection medium is made up of a metastable liquid, that is, a liquid that has been brought above its boiling point. The phase transition occurs thanks to heat peaks produced by the energy deposited along the track by the particle that crosses the medium; thus there is the formation of bubbles along the track upon exceeding a certain energy threshold. Currently PICO operates through two different chambers. One is called PICO-2L with $2.9kg$ of C_3F_8. The other, PICO-60, is the largest bubble chamber used in the search for dark matter, filled with $36.8kg$ of CF_3I for the first data capture, and with an equal quantity of C_3F_8 in the second. Due to the total spin of the non-zero ^{19}F PICO has excellent sensitivity to spin-dependent WIMP-proton scattering.

The recent advances that characterize WIMP's direct detection experiments have been exposed to date. Although until now there has been no solid evidence of real events, the development in this field is aimed at improving sensitivity in research experiments, which one day could reveal for the first time an authentic signal of WIMPs. Future experiments are planned to push their sensitivity down to the irreducible neutrino background in almost the entire mass range of the WIMPs.

In figures 2.3, 2.4 and 2.6, relative respectively to the spin-dependent (SD) WIMP-nucleon and spin-independent (SI) interactions, the trend of the exclusion limits for the cross sections according to the mass of the WIMP is reported , with a 95% confidence level. These curves represent the minimum cross sections to be excluded in the WIMP-nucleon scattering detection experiments. It should be noted that the exclusion curves for the PANDAX-II and LUX experiments show a rise in correspondence with very small masses ($< 10GeV/c^2$) due to the fact that the recoil energy emitted after the collision it is so low that the used detector proves to be inefficient for these values of the mass of the WIMP, since it is not able to detect any signal. Figure 2.3 also shows the background curve due to solar neutrinos: the neutrinos from the Sun arrive on Earth and interact with matter through weak nuclear force characterized by very small cross sections, and for these values the neutrino-nucleus scattering it represents a not negligible background with respect to the WIMP-nucleus interaction events. As previously mentioned, there are several factors that determine the WIMP signal: the motion of the Sun in the Milky Way,

the local density of WIMP and the profile of the local velocity distribution of WIMPs all have a effect on the rate of events in direct dark matter detection experiments and therefore they will modify the shape of the *neutrino floor*[24] (pink region in the figure).

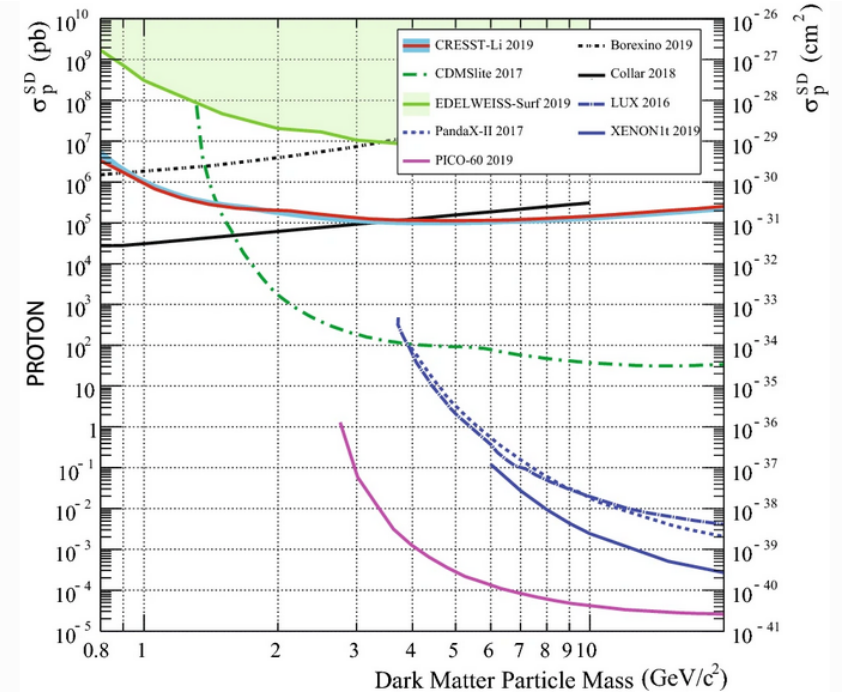

Figure 2.3. Trend of the cross section limits as a function of the mass of the WIMPs in the spin-dependent WIMP-proton scattering (SD)[23].

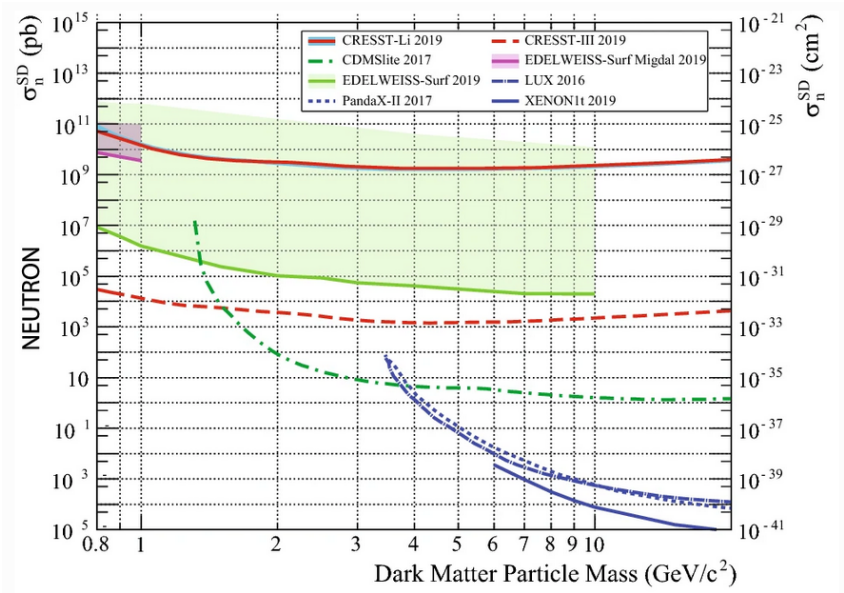

Figure 2.4. Trend of the cross section limits as a function of the mass of the WIMPs in the spin-dependent WIMP-neutron scattering (SD)[23].

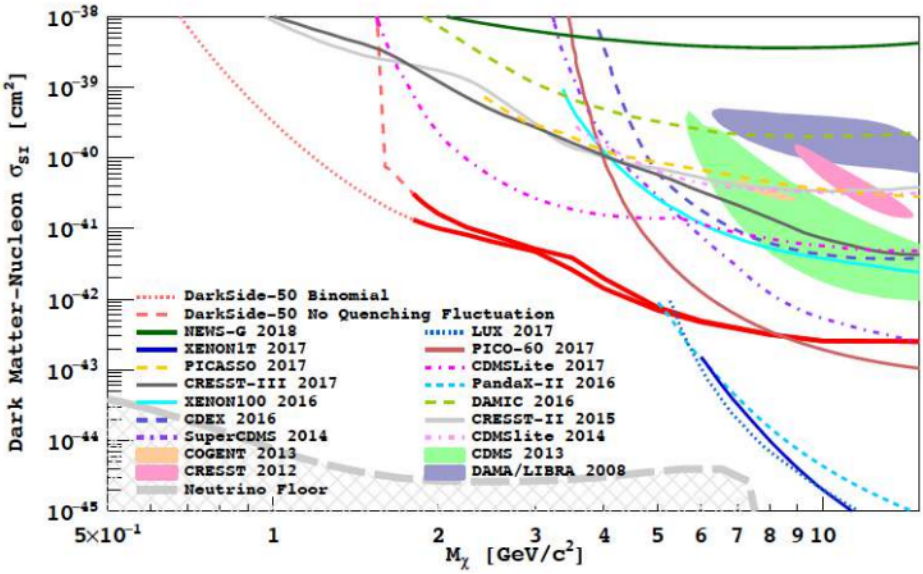

Figure 2.5. Upper limits on the WIMP-nulceon cross section in the low mass region above 1.8 Gev/c^2. The DS-50 results, obtained from the analysis of the ionization signals, are plotted in red.[42].

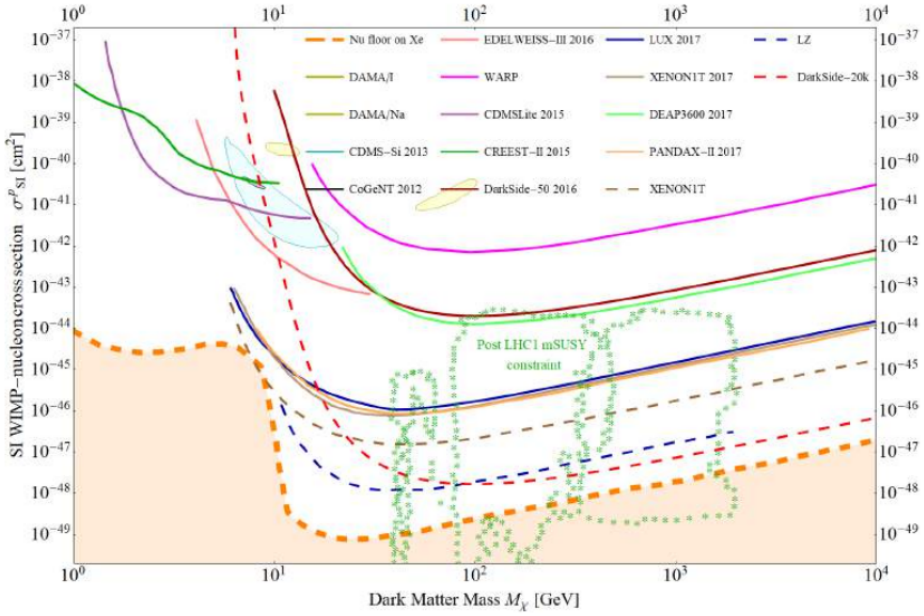

Figure 2.6. Exclusion limit on the WIMP-nucleon cross section with spin-independent interaction. DS-50 latest result is shown with the black solid line. Dashed lines represents projections for future experiments.[42].

Chapter 3

The DarkSide-20k experiment

Detection of WIMPs is a real challenge for researchers at the present day, since they are particles that interact very weakly with ordinary matter. It is crucial in this sense for the experiments involved in this field to improve their sensitivity by many orders of magnitude: for direct research experiments this means being able to operate in a background-free regime, a fundamental point for a possible discovery of dark matter.
In order to achieve this, the world's top four dark matter experiments with argon (ArDM at LSC, DarkSide-50 at LNGS, DEAP-3600 at SNOLab and MiniCLEAN at SNOLab) joined forces to create a unified program for LAr direct dark matter direct detection: the DarkSide-20k project. In December 2015, the DarkSide Collaboration submitted a proposal to Istituto di Fisica Nucleare (INFN) and to the National Science Foundation (NSF) for the funding the experiment. The DarkSide-20k experiment aims to achieve an important improvement in sensitivity for direct detection of WIMPs, reaching $1.2 \cdot 10^{-47} cm^2$ for WIMPs of 1 TeV/c^2 mass. It is proposed to accomplish this purpose with a liquid argon dual-phase time projection chamber (LAr TPC) experiment with a fiducial mass of 20t, for a total exposure of 100 t yr to be accumulated in a run of 5 yr[34]. The DS-20k liquid argon time projection chamber will be deployed at LNGS in the underground Hall C, at the center of the newly constructed active veto system. The DS-20k experiment is designed to mantain an irreducible background level in the WIMP search region of less the < 0.1 events for the total exposure. Thanks to its straordinary low instrumental background, DarkSide-20k could extend its sensitivity to $7.4 \cdot 10^{-48} cm^2$ for 1 TeV/c^2 WIMPs for ten years run with a 200 tyr exposure.[27].

The following two sections are based on Ref. [28].

3.1 Dual-phase LAr TPC

A particle that interacts in a noble liquid generates atomic ionization and excitation. In liquid argon an accited atom forms a dimer with a neutral atom (diargon) and decays subsequently emitting radiation:

$$Ar^* + Ar \rightarrow Ar_2^* \rightarrow 2Ar + \gamma \tag{3.1}$$

In the case of nuclear recoil the collision between two excitons can take place and

it can cause the emission of an electron with low energy, which is lost even before it can recombine:

$$Ar^* + Ar^* \rightarrow Ar^+ + Ar + \gamma \tag{3.2}$$

This process clearly reduces the number of photons emitted by scintillation as two excitons generate only one photon. This phenomenon is the mainly responsible for damping signals due to nuclear recoil. The situation is different for electron recoils, for which the emission efficiency (ratio of photons emitted per exciton) is ~ 1.
In the event of ionization, the positive ions form a charged dimer with neutral atoms. The free electrons thermalize and can recombine with the charged dimers. This mechanism leads to the formation of excited dimers which, as seen above, de-energize by emitting scintillation light:

$$Ar^+ + Ar \rightarrow Ar_2^+ \tag{3.3}$$

$$Ar_2^+ + e^- \rightarrow Ar_2^* \rightarrow 2Ar + \gamma \tag{3.4}$$

Both atomic excitation and ionization lead to the same excited state Ar_2^*, therefore the energy of the emitted photon is the same 3.2.

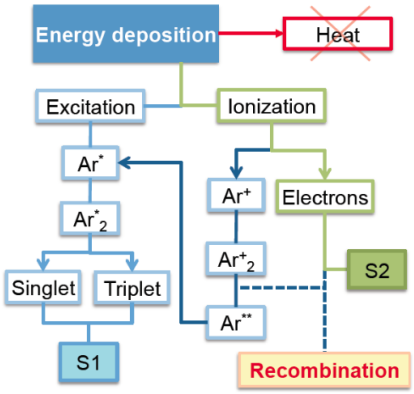

Figure 3.1. Scintillation and ionization mechanisms in liquid argon.

Gamma rays are emitted in the VUV (Vacuum UltraViolet) range with a peak at 128 nm (E$\sim$9.7 eV). The relationship between excitons and ion pairs is defined as $\alpha = N_{ex}/N_{ion}$, assumed constant with respect to the recoil energy. If this parameter is small then most of the scintillation light comes from the recombination of ions and free electrons. Then, based on the considerations made above, the electron recoils will show an higher α than nuclear recoils. An external electric field can accelerate the electrons to drift away from the interaction region, so that they can be measured. Usually in dual-phase liquid argon TPC this field is of the order of hundreds V/cm. Only free electrons that escape the recombination process contribute to the ionization signal, so ionization and scintillation are anti-correlated. If the electric field is turned on it can influence the ratio between scintillation and ionization, since the greater its intensity is, the lower is the probability of recombination of the electrons.

The ionization electrons, removed to avoid their recombination with the positively charged dimers, are extracted in a layer of gas on top of the liquid: this process takes place through the presence of a second electric field of much greater intensity (order of kV/cm) which accelerates the electrons in the gas producing a scintillation signal here. The scintillation signal that occurs in the liquid is called S_1, while the delayed signal that occurs in the gas due to the ionization electrons is the signal S_2 (fig. 3.2). The gaseous region is some mm thick and it is created on top of the liquid by heating the liquid itself, while a transparent grid of a few mm is positioned below the surface of the liquid in order to provide the creation of the two electric fields.
To detect the light emitted by the two scintillation signals, arrays of photosensors are installed above and below the TPC. Thet detect light in the visible spectrum, but the scintillation light in the argon liquid is emitted with a wavelength peaked in 128 nm (VUV light): in order to reveal it a wavelenght shifter that covers the internal walls of the TPC is necessary.
The light detectors consist of the union of single units and thanks to this technical feature it is possible to localize the interaction on the orthogonal plane respect to the electric fields direction. The measurement of the time interval between the signals S_1 and S_2 allows the reconstruction of the event along the vertical axis, known the electron drift speed in the liquid argon. Vertical reconstruction is a very effective tool for background rejection: multiple events induced by multiple ionizations are identified because they occur at different vertical positions.

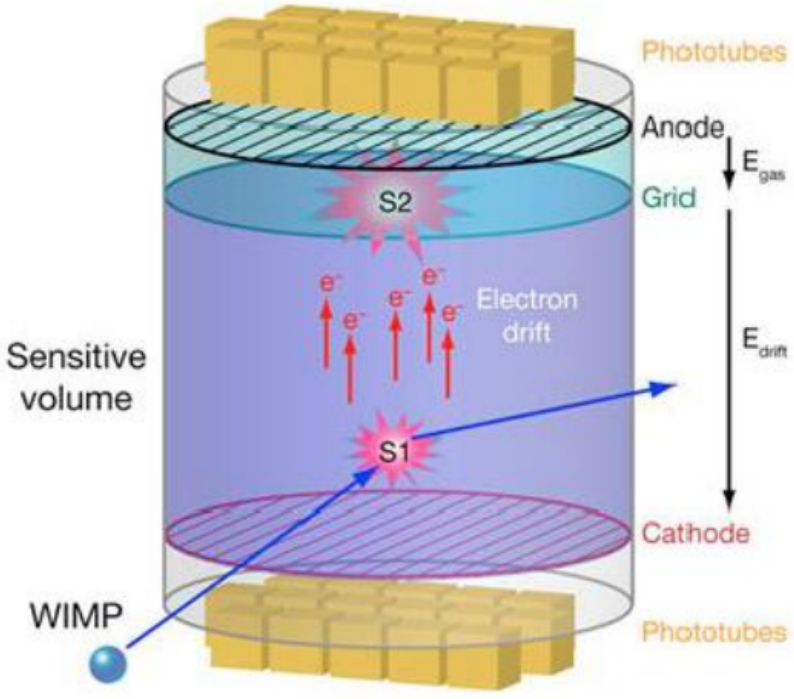

Figure 3.2. Operating principle of dual-phase TPC[29].

3.2 Pulse shape discrimination

The excitement of argon - but applies to all noble elements, involves two states, a singlet and a triplet. The two states cannot be spectroscopically distinguished since their difference in energy is minimal. However, they de-energized exponentially with very different time constants τ, and it is precisely τ that allows their distinction in an important manner: $\tau_s \sim$ 7 ns and $\tau_t \sim$ 1.6 μs. In-depth studies have shown that the singlet component is present in a smaller quantity for greater quantities of energy deposited in the medium. The singlet fraction that characterizes electron recoils is about 0.3, while for nuclear recoils it is about 0.7, in liquid argon. So it is reasonable to expect a scintillation signal that decreases very quickly for nuclear recoils, and a much slower pulse for electron recoils (fig.3.3).
To discriminate nuclear and electron recoil events it is then possible to calculate the singlet component present in a scintillation pulse. The singlet states completely decay in a few tenths of nanoseconds and therefore one can compute the ratio between the integral of the signal in the first tenths of nonoseconds and the total integral. The parameter that estimates this quantity has been defined as f_{90}:

$$f_{90} = \frac{\int_0^{90ns} S(t)dt}{\int_0^{7\mu s} S(t)dt} \tag{3.5}$$

This is true with fast light detectors, such as PMTs. It can be noted that the separation between the two states decreases sharply when the energy deposited is lower ($\sim$ few keV$_{ee}$), since the singlet state is more closely related to high energies, so the singlet fraction tends to 0.5 for both recoils. For high energies, however, the difference between these quantities is more important.
The pulse shape discrimination (PSD) is a prerogative of liquid argon and offers a unique tool for the background rejection. In argon detectors contributions from β and γ sources can be suppressed to unprecedented levels[28].

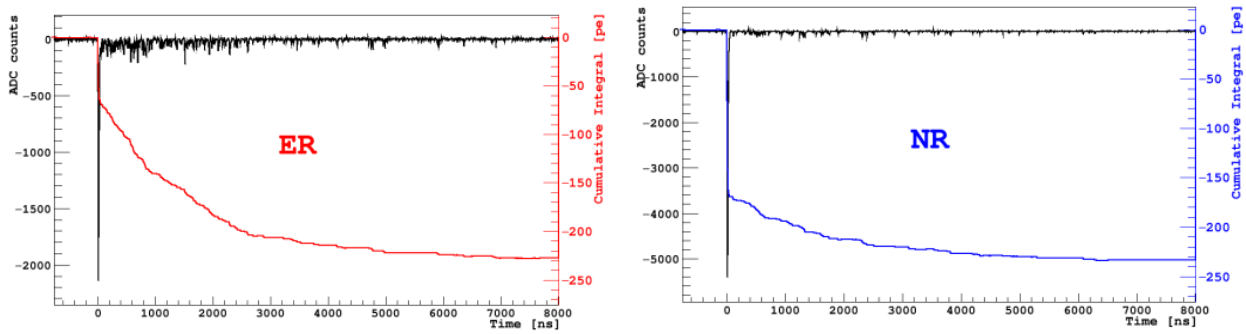

(a) (b)

Figure 3.3. Comparison of two typical waveforms for ER (left) and NR (right) in liquid argon. The two examples are chosen to have approximately the same integral: in the ER case, the prompt fraction of the signal is smaller with respect to the NR case. The solid curves represents the cumulative integral of the waveforms in both the cases[28].

3.3 A background-free search for dark matter

The goal of DarkSide-20k is to discover dark matter. WIMPs are expected to interact with the nuclei of the target, inducing low energy (< 100 keV) nuclear recoils. Since dark matter interactions are very rare, a direct detection experiment must have a low energy detection threshold and excellent background rejection (few interactions per yr for each ton of target). In order to achieve a result free from the instrumental background, the experiment aims to completely eliminate or minimize the background coming from the following sources:

- **nuclear recoils**: neutrinos, α surface particles, radiogenic neutrons, cosmogenic neutrons and cosmic muons;
- **electron recoils**: β and γ radiation.

Neutrinos : atmospheric neutrinos and diffuse supernova neutrinos are the only sources of background that are sufficiently energetic to produce nuclear recoils: the coherent scattering of neutrinos with the argon nuclei in the target causes nuclear recoils indistinguishable from those due to the WIMPs. Although these events constitute an irreducible background (3.2 events over the 200 tyr exposure[34]) in the research of WIMPs, they are also part of a physical signal component still undetected.

α **surface particles** : they come from the ^{238}U and ^{232}Th chains. They represent a dangerous background as they can create signals of nuclear recoils in many ways similar to those caused by WIMPs. Through the study of radioactive chains present in the apparatus this background source can be recognized and removed from the data. In addition these particles lose energy by ionization in a few tens of μm near the surface of the experimental devices: they can be eliminated therefore with appropriate geometric cuts that define the fiducial region of the detector[30].

Radiogenic neutrons : radiogenic neutrons represent the most dangerous type for research of WIMPs together with cosmogenic neutrons. The scattering between a neutron and a nucleus produces a nuclear recoil of with energy spectrum very similar to the WIMP case. They come from decays and from the spontaneous nuclear fissione of the radioactive isotopes present in the materials with which the experimental apparatus is built. One way to help rejection of these neutrons are multiple nuclear recoils, which a WIMP won't never do because to the low probability of interaction. Two more methods are the passive shield and the active veto.

Cosmogenic neutrons and cosmic muons : they can come directly from the space and for this reason the experiment is located underground. However muons can also reach an underground laboratory because produced in the interaction of neutrinos in the rock. They are rejected by the presence of Cherenkov light detectors in water. They are dangerous because they give rise to neutrons and others particles that can reach the internal detector[30]. Cosmogenic neutrons are revealed in the same way.

β and γ radiation : these kind of radiations are two further source of background. The β is one of the most important in the search for dark matter both for the high rate and for the high penetration into matter. This radiation produce an electron of moderate energy (a few hundred keV) and it comes from the radioactive isotopes present in the structure, such as ^{238}U and ^{232}Th chains. Another source of β radiation is ^{39}Ar present in atmospheric argon (AAr) due to cosmogenic activation from ^{40}Ar. For this reason DS-20k will use undergrond argon (UAr) which will be purified after cryogenic distillation to a sample 99.95% pure.
Gamma rays are produced from all this surrounding the apparatus, from the structures themselves and from the radioactive decays natural; thay can produce electrons interacting with the detector materials such as structures or the possible scintillators. To reduce these kind of contaminations requires special precautions are required, such as shield, veto systems, PSD[30].

In the multitude of detector technologies, TPCs with noble liquid, which detect both the scintillation light and the ionization electrons produced by recoiling nuclei, have important advantages for the direct search of dark matter. In the case of liquid argon (LAr), effective discrimination against the background using the time-developing primary scintillation signal (PSD), the exact identification of event locations in all three dimensions given by the TPC, and the effectiveness of the chemical and cryogenic purification of the argon have all been demonstrated. Analysis made on exposure of large amounts of atmospheric (AAr) and underground argon (UAr) predict that a result free from the instrumental background can also be obtained using a detector with a multi-tonne mass[27].
The choice to use dual-phase geometry is given by the need to obtain the best performance in the search for dark matter WIMP. The detector DarkSide-50 has demonstrated an impressive permormance in background rejection. No single-phase detector has yet produced a comparable result in this research area, due to the lack of S_2 signal[27].
On this basis, the DarkSide Collaboration proposes the construction of DarkSide-20k, a direct WIMP search using a LAr TPC with a fiducial mass of 20t of UAr. As shown in Fig. 3.4, the DarkSide-20k TPC will be placed underground at LNGS. DarkSide-20k will be a detector with ultra-low background levels and the ability to measure its backgrounds *in situ*[34]. It is designed to achieve an exposure of 200 t yr, accumulated during a run of approximately 10 yr, free of instrumental background, giving a sensitivity to WIMP-nucleon interaction cross sections of $7.4 \cdot 10^{48} cm^2$ ($6.9 \cdot 10^{-47} cm^2$) for WIMPs of 1 TeV/c^2 (10 TeV/c^2) mass. The projected sensitivity of DarkSide-20k is compared with other current and planned projects in Table of fig. 3.5.
The daunting presence of the background due to neutrons that recoiling on the nuclei gives rise to an event that is confused with a typical WIMP signal. To face this challenge there is a veto detector made of passive Gd-loaded acrylic Shell (GsAS) surrounding the inner detector and between two active AAr layers. The Gd-loaded PMMA shell moderates neutrons emitted in the LAr TPC, by emission of scintillation light. Both TPC and veto dector will be hosted in a ProtoDune-like cryostat surrounded by layers of plastic to moderate cosmogenic and radiogenic

neutron from the rocks surrounding Hall C in the underground LNGS[34]. The LAr TPC will be instrumented with Silicon PhotoMultipliers (SiPMs) as photosensors: their higher radiopurity and a more efficient assembly are fundamental for DS-20k, since the Pulse Shape Discrimination (PSD) is strictly related to the light yield[35]. DarkSide-20k photosensor unit is a Photo Detector Module (PDM), consisting of a tile of 24 SiPM (this important topic will be further investigated in chapter 4). The Aria and Urania projects, associated with the DarkSide Collaboration, deal with the extraction, purification, transport and storage of low-radioactivity argon at the multi-tonne level, in order to obtain UAr as the target of the experiment. In short, DarkSide-20k will perform the most sensitive search for dark matter yet proposed and will also provide a convincing foundation for a 100 t-scale detector[27].

3.4 Experimental design of DarkSide-20k

Many of the key design parameters for DarkSide-20k are based on the successful experience of the DarkSide collaboration in the construction and operation of the DarkSide-50 detector in a background-free mode. The DS-20k experiment is designed to operate for a minimum of 10 yr while maintaining an irreducible background level in the WIMP search region of less than <0.1 events for the total exposure. To achieve this goal, the design parameters of the DS-20k experiment have been taken directly from DS-50, where possible. Design changes have been made where needed in order to accommodate for the much larger size of DS-20k and to allow the experimental design to be scalable to a detector at the multi-hundred tonne scale. The LAr TPC will also be deployed at LNGS, in the underground Hall C, in the center of an active veto system. Fig. 3.4 shows the project of the experiment. This section, based on Ref.[34], describes the design of the project and introduces the features of the experiment.

3.4.1 Liquid Argon TPC

The DarkSide-20k LAr TPC is the dark matter detector and the central element of the experiment, with all auxiliary detectors and systems specified and designed in support of it. The DS-20k LAr TPC will use some 50 t of LAr extracted from an underground source as the target material for WIMP detection. An ultra-pure acrylic vessel is used to contain the LAr. Features directly fabricated onto the inner surfaces of the acrylic vessel will form the TPC itself. These feature are the TPC field cage system, the anode and the cathode and are implemented on the acrylic panels with a commercial conductive polymer coating, called Clevios™. Use of this coating eliminates the use of conductive metals materials. The DS-20k LAr TPC design parameters are summarized in table of fig. 3.6.

The same pure acrylic material, in the form of 4 mm thick sheets, is used to hold the Enhanced Specular Reflector (ESR) reflector foils installed to maximize light collection. The TPC is designed such that all the inner surfaces facing the active volume are coated with TPB, a wavelength shifter, to ensure the complete conversion of the 128 nm argon scintillation light to 420 nm, where the SiPMs peak in their PDE. Two identical photosensor arrays of 4140 channels each are placed on top and bottom of the TPC, but outside of the acrylic vessel. The TPC is

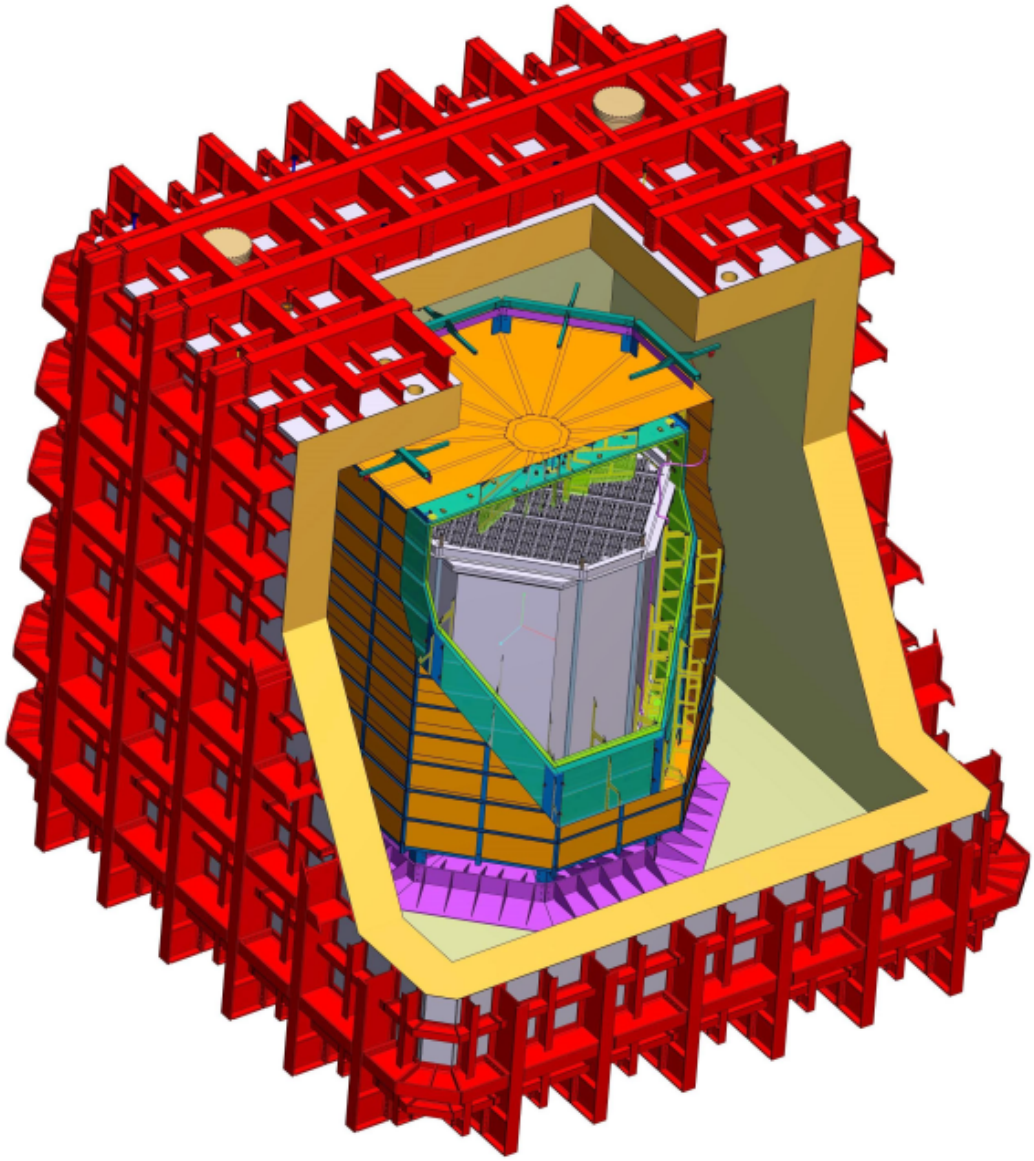

Figure 3.4. Cross sectional view of the DarkSide-20k experiment, showing the acrylic (PMMA) sealed TPC filled with UAr (grey), its top plane equipped with photo detectors, surrounded by the veto detector consisting of a Gd-loaded acrylic Shell (GdAS) (green) sanwiched beetween two atmospheric argon (AAr) active layers, all contained in the ProtoDune-like cryostat (red).

mounted inside a neutron veto detector, whose most important component is a 10 cm thick, gadolinium loaded, acrylic shell that completely encapsulates the TPC. This plastic shell defines two 40 cm thick active volumes, respectively named the inner and outer buffer, filled with liquid AAr. The buffers are further segmented with ESR, also coated with TPB. The whole apparatus is placed inside a light and electromagnetic shield barrier, contained in the ProtoDUNE-like cryostat filled with AAr.

Experiment	Target	Exposure/[t yr]	$\sigma/[\mathrm{cm}^2]$ @1 TeV/c^2	$\sigma/[\mathrm{cm}^2]$ @10 TeV/c^2
DarkSide-50	Ar	0.011	9×10^{-44}	8×10^{-43}
XENON-100	Xe	0.021	2×10^{-44}	2×10^{-43}
LUX	Xe	0.092	1×10^{-45}	1×10^{-44}
ArDM	Ar	1.5	8×10^{-45}	7×10^{-44}
DEAP-3600	Ar	3.0	5×10^{-46}	5×10^{-45}
XENON1T	Xe	2	1×10^{-46}	1×10^{-45}
LZ	Xe	15	3×10^{-47}	3×10^{-46}
XENONnT	Xe	20	2×10^{-47}	2×10^{-46}
1 ν-induced	Xe	34	5.9×10^{-48}	5.8×10^{-47}
nuclear recoil	Ar	52	1.6×10^{-47}	1.5×10^{-46}
DarkSide-20k	UAr	100	1.2×10^{-47}	1.1×10^{-46}
DarkSide-20k	DAr	200	7.4×10^{-48}	6.9×10^{-47}
Argo	DAr	1000	2.7×10^{-48}	2.5×10^{-47}

Figure 3.5. Comparison of sensitivity for current dark matter experiments leading the search for high mass WIMPs and of future approved and proposed experiments[27].

Parameter	Value
TPC drift length	350 cm
Octagonal inscribed circle diameter (87 K)	350 cm
Total LAr mass	51.1 t
Active LAr mass	49.7 t
Fiducial cut distance (vertical)	70 cm
Fiducial cut distance (radial)	30 cm
Fiducial LAr mass	20.2 t
Drift field	200 V/cm
Extraction field	2.8 kV/cm
Luminescence field	4.2 kV/cm
Cathode operating voltage	−73.8 kV
Extraction grid operating voltage	−3.8 kV
Anode operating voltage	ground
Gas pocket thickness	(7.0 ± 0.5) mm
Grid wire spacing	3 mm
Grid optical transparency	97 %

Figure 3.6. DarkSide-20k TPC parameters.

Sealed PMMA Vessel

An acrylic (PMMA) vessel will be used to confine the UAr in order to use it more efficiently. PMMA is extremely radiopure, resulting in a residual neutron background estimated to be $<10^{-3}$ for the exposure of 200 t yr. The TPC active volume is confined in all directions by the sealed PMMA vessel that is formed by bonded plates or panels (fi. 3.7). The body of the PMMA vessel will be made of 5 cm thick acrylic plates fused together, and then flanged and sealed with the top and the bottom lid, that serve as the anode plate and cathode plate of the TPC, respectively. The ESR-acrylic reflector panels are located inside the acrylic vessel. The top and bottom PDM arrays are placed outside of the acrylic vessel, immersed in the AAr of the neutron veto detector. PDM arrays will be isolated from any light generated in the veto detector.
A commercial conductive and transparent Polymer coating, Clevios™being used in industrial applications such as transparent electrodes for touch panels and printed electronics. The main advantage of Clevios™is its composition. Being a water-based

solution, the large-area coating needed for the anode and cathode will be easier to accomplish. In terms of the optics, three coating samples with thickness 4 μm, 8 μm and 12 μm, respectively, will be applied on acrylic plates.

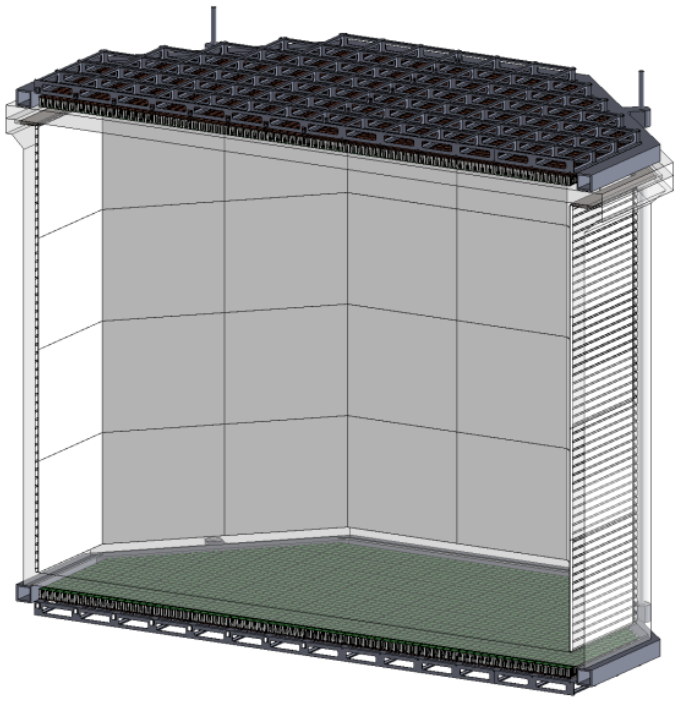

Figure 3.7. Recostruction of the PMMA vessel and the TPC[34].

LAr TPC Size Consideration

Since the SiPM tiles are all square shaped, the DS-20k TPC will be an octagonal shape to best fit the coverage of the PDMs. The size of the TPC is determined by the patterning strategy of the SiPMs, driven by the design size of the square motherboards (SQB). There are 156 fully populated SQBs containing 25 PDMs, as well as 16 modified SQBs which have only 15 PDMs positioned toward one corner (fig. 3.8). The edge of the active volume of the TPC will shrink about 2.7 cm from the edge of the SiPM array, the distance from edge to edge of the octagonal active volume will be 350 cm. The height of the TPC will be 350 cm. With this design, the total mass of LAr in the active volume and fiducial volume (with 70 cm vertical and 30 cm lateral cuts) are 49.7 t and 20.2 t respectively.

Reflector Panels

The ESR is a thin layer foil which has reflectivity of 98% for 420 nm light, with a thickness of only 50 μm. In order to hold the ESR foils in place and maintain their flatness during the operations, 4 mm thick UVT acrylic sheets will be used. The surface of each ESR foil facing the active LAr volume will be coated with TPB (fig. 3.9).

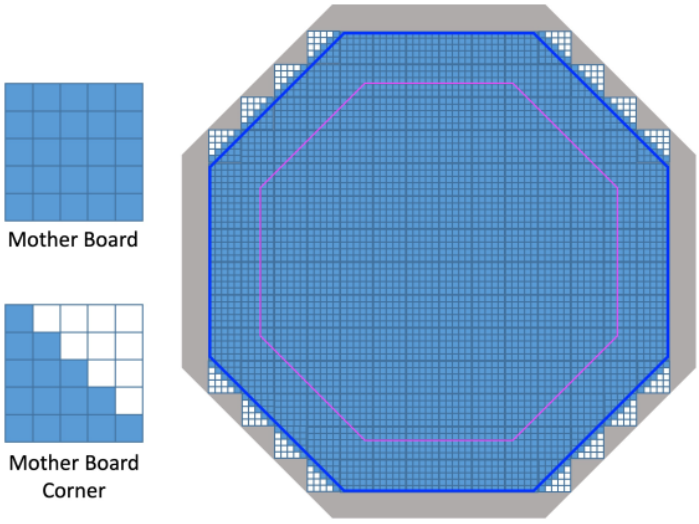

Figure 3.8. Patterning scheme for the PDMs. Pink lines indicarw the edges of the TPC active voulme[34].

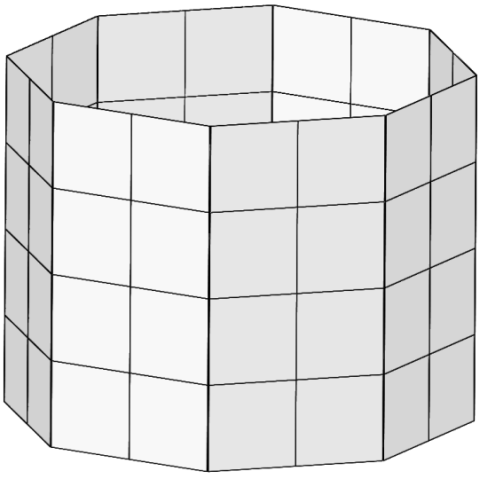

Figure 3.9. 3D model of the full DS-20k LAr TPC reflector panels system[34].

Field Region

Within the sealed acrylic vessel, the electrode features of the TPC are realized using the Clevios™conductive polymer coated directly onto the acrylic vessel. The inner surface of the acrylic vessel will be machined with grooves such that recessed areas have geometries similar to an electrode ring, and when coated with the Clevios™comprise the TPC field-shaping rings that are highly uniform across the height of the TPC. The relative permittivity of LAr and GAr are 1.54 and 1.03 , respectively. By applying electric potentials of zero, -3.8 kV, and -73.8 kV to the anode, extraction grid and cathode, respectively, three different field regions are formed in the TPC:

- The uniform drift field of 200 V/cm in the liquid phase, formed by the geometry

of the field cage. The drift distance between the cathode Clevios TM layer and the extraction grid is 350 cm;

- The extraction field in the liquid phase above the grid is 2.8 kV/cm. The distance between the extraction grid and the surface of the LAr is 3 mm;
- The electroluminescence field in the gas phase is 4.2 kV/cm. The gas gap between the surface of the LAr and the Clevios™layer acting as the anode is (7.0 ± 0.5) mm thick.

As the top boundary of the active volume, a 5 cm thick acrylic window serves as the diving bell to maintain a stable gas pocket. A thin layer of Clevios TM conductive polymer is coated on the inner surface to act as the anode and a layer of TPB coated onto the Clevios™layer to shift the scintillation light wavelength (fig. 3.10). Right below the liquid surface is the extraction grid, composed of stainless steel wires (not shown in figure) stretched in parallel with 3 mm spacing and held in place via small posts set into a stainless steel frame. The bottom boundary of the active volume, shown in the right panel fig. 3.10, is a 5 cm thick acrylic window coated with a thin layer of Clevios™on both sides. A layer of TPB will be coated on the top Clevios™layer for wavelength shifting.

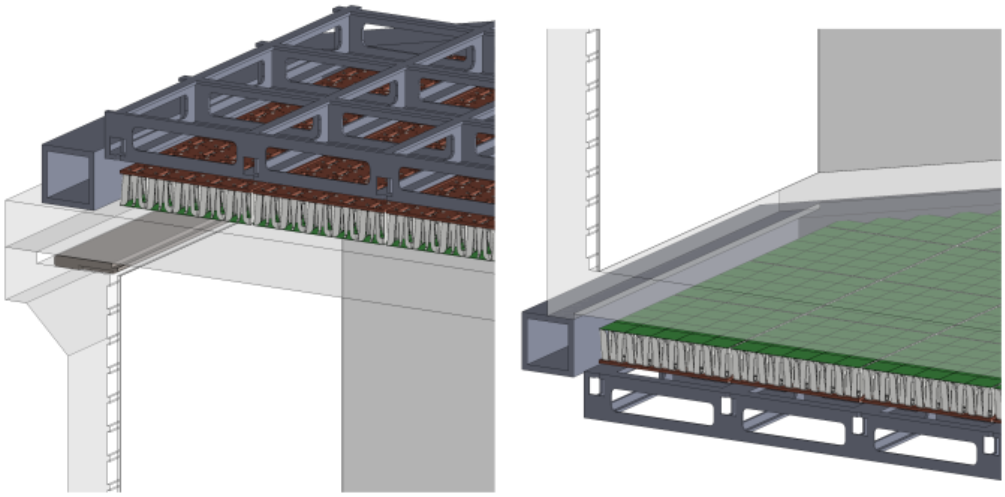

Figure 3.10. 3D model of the LAr TPC anode and extraction (left) and 3D model of the LAr TPC cathode region (right)[34].

Gas Pocket

The gas pocket in DS-20k LAr TPC is the gaseous argon region with (7.0 ± 0.5) mm thickness under the anode, where the electroluminescence process occurs. The uniformity of the electroluminescence field is essential for the S_2 resolution, resulting in a critical requirement of the anode flatness, which can be achieved by precisely maintain the pressure balance between UAr in the TPC and AAr in the Veto. With the nominal AAr pressure of 1075 mbar, the nominal UAr pressure in the gas pocket is derived as 19.6 psia. The gas pocket will be generated and maintained by two

means: a bubbler and a gas feed-in. The bubbler is a unit containing plenty of Pt-100 RTDs with adjustable heating power to boil off LAr. The gas feed-in method will introduce a gas line from the UAr cryogenic system to the TPC and regulate the pressure.

Cryogenic System

The cryogenics system is derived from the successful scheme of the DS-50 cryogenics and gas handling system. There are two major cryogenic systems: one for the AAr in the veto shield inside the ProtoDUNE cryostat and one for the UAr in the sealed acrylic vessel for the LAr TPC. The AAr cryogenics system can be an optimized version specific for the LNGS installation including liquid re-circulation in order to guarantee a safe and homogeneous liquid volume with a pressure and vacuum relief valve, and a warm purification performed in gas phase for efficient impurity trapping as for the UAr system described in detail here below. The UAr cryogenics system for the TPC will be an upgraded system based on DS-50. Liquid nitrogen is the primary cooling source of the entire cryogenics system.
Heat exchangers are strategically placed throughout the system for LAr filling and LAr removal at the various required speeds for the different operational modes. The continuous argon circulation for purification is driven by a set of specialized gas argon pumps. Combined with the integrated heat exchanger systems, the system can handle high circulation rates drawing either, or both, liquid and gas phase argon to effectively remove electronegative impurities. The designed system allows the use of SAES hot getter to remove N_2 , CO_2 , and O_2 . The purification capabilities of DS-20k are further enhanced by the addition of a parallel continuous LAr cryogenic circulation system whose baseline use will be the removal of radon from the LAr TPC volume. The total cooling power of the cryogenics system is designed to handle the total heat load from the power dissipated by the cold electronics operating inside the liquid argon volume.

3.4.2 Veto Detector

Benefiting from the implementation of a ProtoDUNE-like AAr cryostat, the veto detector utilizes AAr as the scintillation material. The veto detector is composed of three separate volumes: a passive octagonal shell made of Gd-loaded PMMA (acrylic) called GdAS, mounted around the TPC and providing to the TPC a 4π coverage; a 40 cm thick inner volume of active liquid AAr called the Inner Argon Buffer (IAB) and sandwiched between the TPC vessel and the GdAS; a 40 cm thick outer active volume of AAr called the Outer Argon Buffer (OAB) contained between the GdAS and the outer copper Faraday cage. The Faraday cage contains the veto and TPC detectors, and insulates them optically and electrically from the remaining, outermost AAr volume contained within the cryostat (fig. 3.11).

The required thickness of the GdAS is of about 10 cm. The GdAS moderates neutrons emitted from all of the detector materials, particularly from the ones which make-up and surround the LAr TPC, while also enhancing the neutron capture probability with the inclusion of the Gd. The capture of the neutron on a Gd nucleus results in the emission of multiple γ-rays. These γ-rays interact in the IAB and OAB

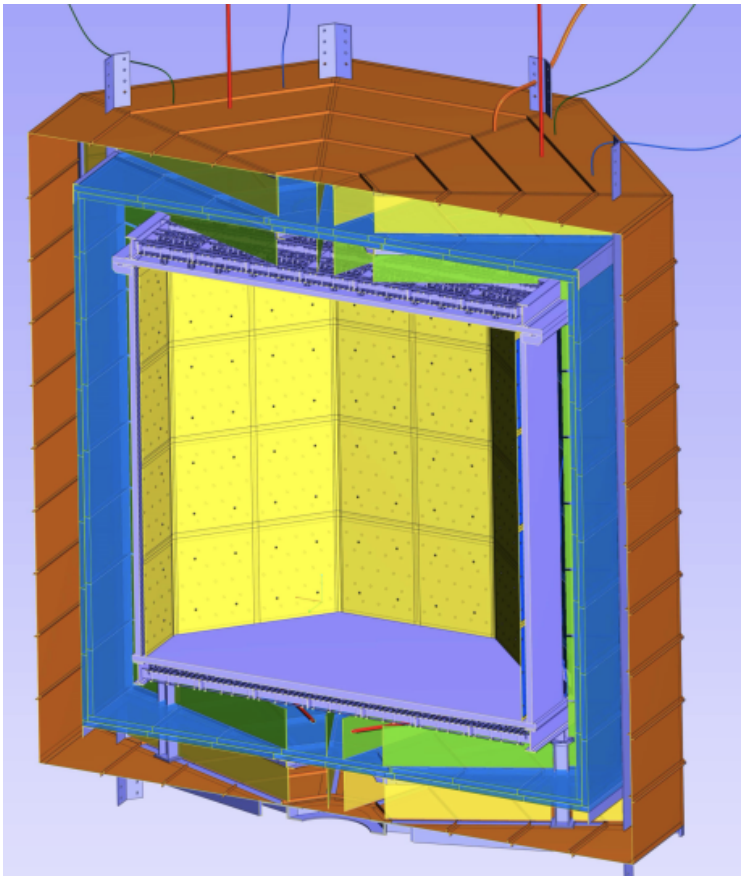

Figure 3.11. View of the DS-20k veto detector. In blue are the Gd-loaded PMMA elements composing the GdAS. The farady cage is depicted in brown. The subdivision panels segmenting the IAB are shown in green. The subdivision panels segmenting the OAB are shown in yellow)[34].

and are detected by use of scintillation light emitted by the liquefied AAr in both the IAB and OAB. In order to optimize the light readout and minimize the overall ^{39}Ar rate in each detector element, the IAB is segmented into 8 by subdivision plates coated with a light reflector and a wavelength shifter. Similarly, the OAB is segmented into 8. The GdAS will be built coupling two layers of Gd-loaded PMMA plates with thickness of 5 cm, which is half of the total 10 cm GdAS thickness. The total number of Gd-loaded PMMA plates is of about 450 half of them facing the IAB and half the OAB.
SiPMs will be mounted on the two sides of the GdAS such that they are facing both the IAB and OAB: we foresee about 3000 SiPM tiles in total, 2000 of them facing the IAB and 1000 the OAB. The basic optical detector element is a SiPM tile with a front end board (FEB) coupled to it that is optimized for the geometry and the electronics of the veto detector. Figure 3.12 shows the drawing of the prototype FEB developed for the veto detector coupled to the tile, the core of the veto cryogenic photodetector modules (VPDMs). Approximately 10 VPDMs will be mounted on each GdAS plate facing the IAB, and approximately 5 VPDMs will be installed in the plates facing the OAB. eam. Two couple GdAS plates, one facing the IAB and

one facing the OAB, equipped with their VPDMs and associated electronics and with reflectors coated with wavelength shifter as described below, represent the basic modular unit of the veto detector, which we call veto detector unit (VDU).

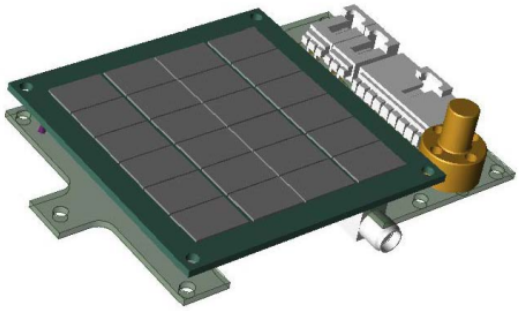

Figure 3.12. Design of the test front end board coupled with the tile to be used in the veto detector[34].

All of the inner surfaces of the veto detector, namely the external walls of the TPC, the walls of the vertical sectors and the inner walls of the Faraday cage, will be covered with reflectors and a wavelength shifter, so that the 128 nm argon scintillation light is shifted to longer wavelengths where the LAr is very transparent. The use of enhanced specular reflector (ESR) foils coated with tetraphenylbutadiene (TPB) is a well-proven technology.

Chapter 4

Silicon Photomultipliers

The goal of the DarkSide experiment is to make a direct detection of Weak Interacting Massive Particles (WIMPs) which are considered as possible candidates for dark matter. One of the key parameters is light detection: DS-20k will use the Silicon PhotoMultipliers (SIPMs) instead of the standard PhotoMultipliers (PMTs) as in DS-50.
The following section is based on Ref.[32].

4.1 SiPM technology

The silicon photomultiplier is a radiation detector with extremely high sensitivity, high efficiency, and very low time jitter.
It is based on reversed biased p/n diodes: a photodiode is formed by a silicon p-n junction that creates a depletion region that is free of mobile charge carriers. When a photon is absorbed in silicon it will create an electron-hole pair. Applying a reverse bias to a photodiode sets up an electric field across the depletion region that will cause these charge carriers to be accelerated towards the anode (holes), or cathode (electrons). Therefore an absorbed photon will result in a net flow of current in a reverse-biased photodiode. The absorption depth of a photon in silicon depends on its energy (or wavelenght). Silicon can directly detect light from near ultra violet to near infrared.
When a sufficiently high electric field ($> 5 \cdot 10^5$ V/cm) is generated within the depletion region of the silicon, a charge carrier created there will be accelerated to a point where it carries sufficient kinetic energy to create secondary charge pairs. In this way, a single absorbed photon can trigger a cascade that will spread throughout the silicon volume subjected to the electric field. The silicon will break down and become conductive, effectively amplifying the original electron-hole pair into a macroscopic current flow. This process is called *Geiger discharge*. A photodiode operated in Geiger mode employs this mechanism of breakdown to achieve a high gain and is referred to as a SPAD (Single Photon Avalanche Diode). Once a current is flowing it should then be quenched. Passive quenching is achieved through the use of a series resistor R_Q which limits the current drawn by the diode during breakdown. This lowers the reverse voltage seen by the diode to a value below its breakdown voltage, thus halting the avalanche. The diode then recharges back to the bias

voltage, and is available to detect subsequent photons. The time it takes for the diode to recharge to the full operating voltage is called the *recovery time*.
The Silicon Photomultiplier (SiPM) integrates a dense array of small, independent SPAD sensors, each with its own quenching resistor (fig. 4.1.a). Each independently operating unit of SPAD and quench resistor is referred to asa "microcell". A typical SiPM has microcell densities of between 100 and several 1000 per mm^2 , depending upon the size of the microcell. Each microcell detects photons identically and independently. The sum of the photocurrents from each of these individual microcells combines to form a quasi-analog output, and is thus capable of giving information on the magnitude of an instantaneous photon flux (fig. 4.1.b)[32].

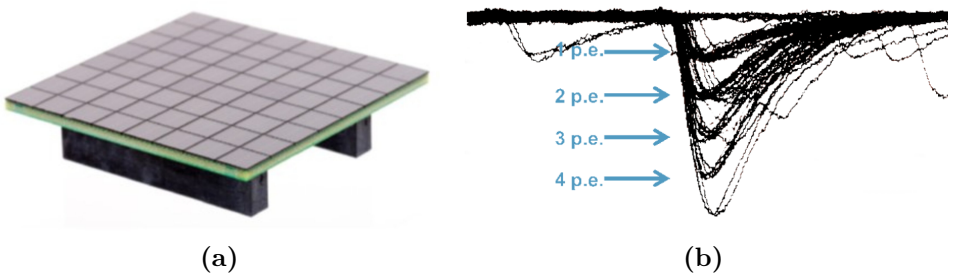

(a) **(b)**

Figure 4.1. Microcell structure of the SiPM surface (right) and oscilloscope signal showing discrete nature of the SiPM output as response of a light pulse.

A typical SiPM anode-cathode output pulse is shown in Figure 4.2. The rise time of the SiPM is determined by the rise time of the avalanche formation and the variation in the transit times of signals arriving from different points on the sensor's active area.
The recovery time of the sensor, or decay time of the pulse, is determined by the microcell recharge time constant, which is given by[32]:

$$\tau_{RC} = C_d(R_q + R_s \cdot N) \tag{4.1}$$

where C_d is the effective capacitance of the microcell, R_q the value of the microcell quench resistor, N is the total number of microcells in the sensor and R_s is any resistance in series with the sensor.

The sensor output is a photocurrent, and the total charge Q generated from an event is given by,

$$Q = N_{fired} \cdot G \cdot q \tag{4.2}$$

where N_{fired} is the number of fired microcells, G is the gain (discussed below) and q is the electron charge. The total charge is also equal to the integral of the photocurrent pulse.

Following parameters are very characteristic and the knowledge of them is necessary to understand the correct working of a SiPM: breakdown voltage and overvoltage, gain, PDE, dark count rate (noise), optical crosstalk and afterpulsing.

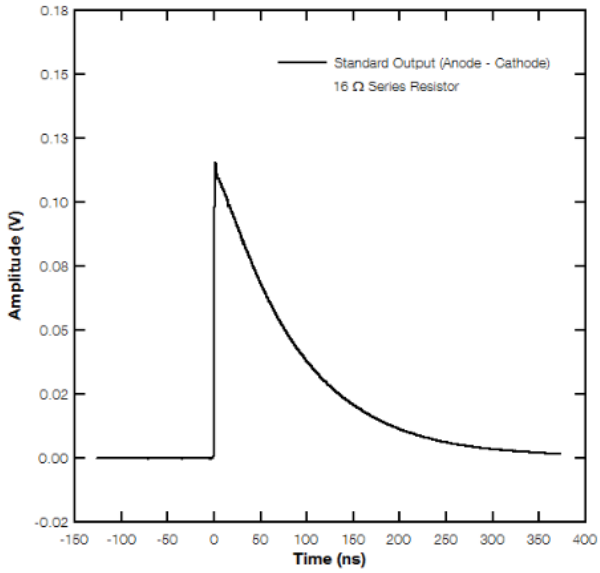

Figure 4.2. Output pulse read out from the anode-cathode.

Breakdown Voltage and Overvoltage

The *breakdown voltage* (V_{br}) is the bias point at which the electric field strength generated in the depletion region is sufficient to create a Geiger discharge. SiPM sensors are operated at a bias point that is typically 10% - 25% higher than the V_{br}. The difference between the V_{br} and the bias point is referred to as the *overvoltage* (ΔV). These values allow the user to calculate the Vbias to apply: $V_{bias} = V_{br} + \Delta V$[32].

Gain

The gain (G) is defined as the number of carriers contained in the single-cell current pulse since this is the number of carriers generated during the avalanche in response to an absorbed photon. It is a function of overvoltage and microcell size. Each microcell in the SiPM generates a highly uniform and quantized amount of charge every time an avalanche is generated by an absorbed photon in the active volume. The gain of a microcell (and hence the sensor) is then defined as the ratio of the charge from an activated microcell to the charge on an electron. The gain can be calculated from the overvoltage ΔV, the microcell capacitance C, and the electron charge, q[31]:

$$G = \frac{C \cdot \Delta V}{q}. \tag{4.3}$$

Each detected photon results in a highly quantized output pulse. If the charge from each pulse is mesured and a charge distribution is formed, the peaks due to certain number of photoelectrons will be visible. Such a spectrum was shown in fig. 4.3.b. The separation between each pair of adjacent peaks (in pC) is constant and corresponds to the charge generated from a single fired microcell. This can therefore be used to accurately calculate the gain, using the equation above.

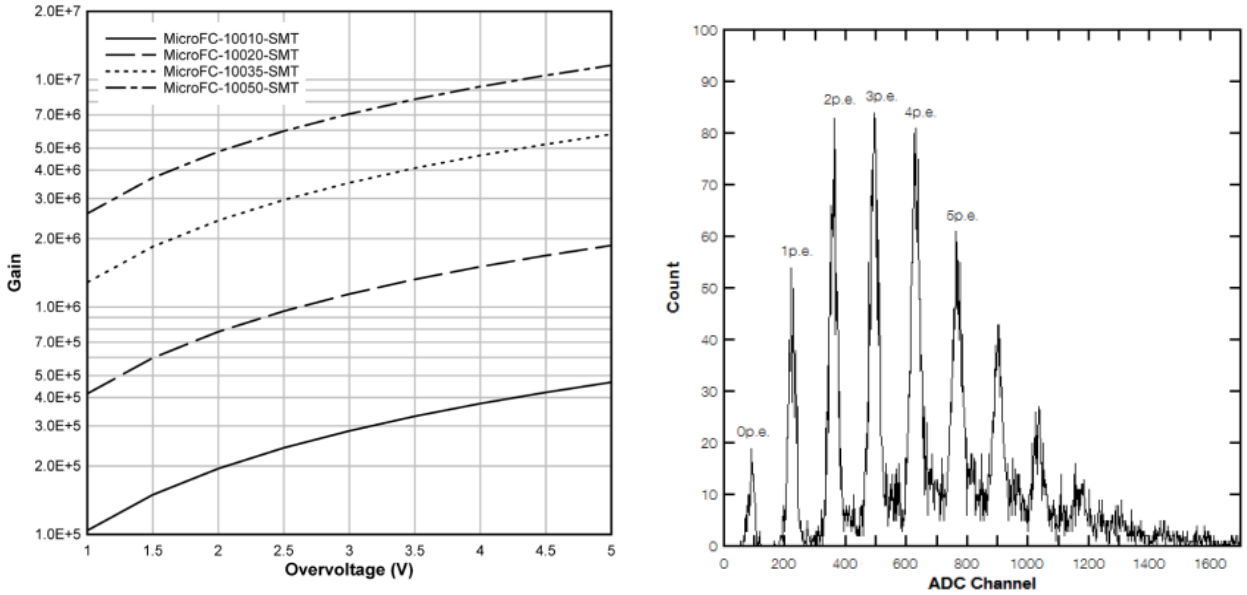

(a) **(b)**

Figure 4.3. Left: gain as a function of over-voltage for dfferent microcells size. Right: charge distribution of photoelectrons detected by a SiPM.

Photon Detection Efficiency

The *photon detection efficiency* (PDE) is a measure of the sensitivity of a SiPM and it is a function of wavelength of the incident light, the applied overvoltage and microcell fill factor. It is the statistical probability that an incident photon interact qith a microcell to produce an avalanche, and it is defined as:

$$PDE(\lambda, V) = \eta(\lambda) \cdot \epsilon(V) \cdot F, \tag{4.4}$$

where $\eta(\lambda)$ is the quantum efficiency of silicon, $\epsilon(V)$ is the avalanche initiation probability and F is the fill factor of the device. Quantum efficiency (Qe) expresses the probability that a photon impinging on the SiPM is actually transmitted to the silicon, absorbed in the silicon and finally converted in an electron/hole pair. The avalanche initiation probability is the probability that the generated electron/hole pair successfully initiates a self-sustaining avalanche process and thus an output current pulse. The fill factor is the ratio of active to inactive area on the SiPM, and is a result of the deadspace between the microcells and therefore depends upon the microcell size[31].

Dark Count Rate

Noise in SiPMs is represented by spurious output current pulses produced in absence of light. In silicon, there is a finite probability for carriers (electron and hole) to be generated by thermal agitation. If an electron or hole originates inside the active region an avalanche is initiated and an output pulse is observed. This is

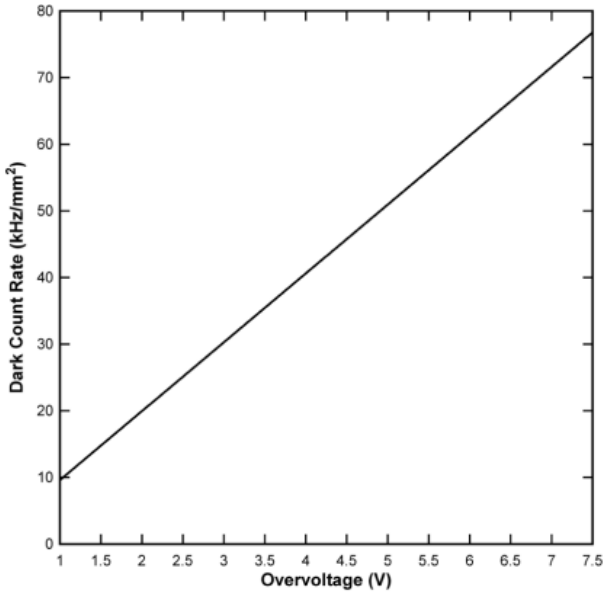

Figure 4.4. DCR as a function of overvoltage for a SiPM[32].

called a *dark event*. The number of dark events per unit time is the *dark count rate* (DCR). DCR if a function of active aerea, overvoltage (fig. 4.4) and temperature[31].

Afterpulsing, Optical Crosstalk

Besides the primary noise, in SiPMs there are other two sources of noise, i.e., *afterpulsing* (AP) and *optical crosstalk* (OC). Both AP and OC events originate from an existing current pulse (which can be either a photon-event or a dark-event) and for this reasons they are referred as to *correlated noise*. **Afterpulsing** is due to the carriers trapped in silicon defects during the avalanche multiplication that are released later on during the recharge phase of the microcell. The net effect is that we observed a new current pulse on the tail of the original current pulse (fig.4.5.a)

During the avalanche process, kinetic energy of avalanching carriers need not necessarily contribute to carrier multiplication. Through scattering collisions, a portion of that energy is lost as heat to phonon vibrations. In a less likely phenomenon, it is also possible for that energy to be emitted as photons. When that occurs, the resulting photons can travel to the neighboring microcells and initiate avalanches in them. This phenomenon is referred to as **optical crosstalk**. If a crosstalk photon produces an electron-hole pair in the depletion layer of a neighboring pixel and triggers an avalanche process as a result, this situation is called *prompt crosstalk*, whose output pulse appears simultaneously with the original pulse (double pulse in fig. 4.5). However, in the alternative scenario that the crosstalk photon creates an electron-hole pair outside a microcell's depletion layer, the resulting electron-hole pair can only trigger an avalanche process after successfully reaching the depletion layer by diffusion. This introduces a delay between the original pulse and its crosstalk noise, which is called **delayed crosstalk** (the third signal of fig. 4.5.b)[31].

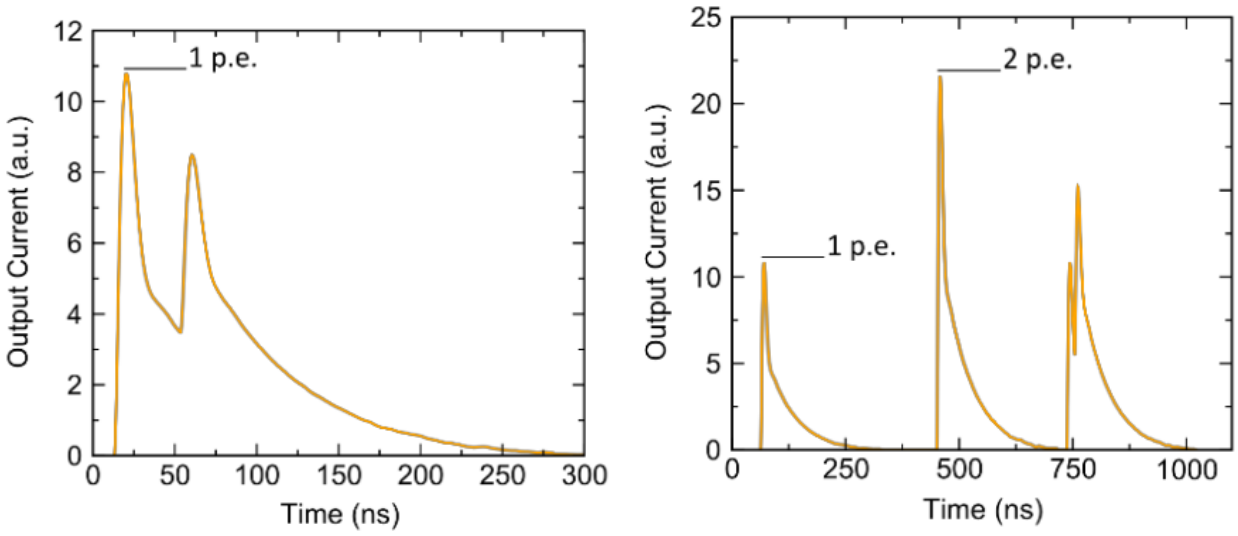

(a) (b)

Figure 4.5. Left: Afterpulsing in SiPMs. The pulse caused by this kind of noise comes few ns after the primary peak. Right: optical crosstalk in SiPMs. From left to right we obsere: a single-cell signal (1 pe), a direct crosstalk signal (2 pe, two cells firing at the same time), and a delayed crosstalk (a second cell fires few ns after a first one).

4.2 Ligh detection in DarkSide-20k

Silicon photomultipliers (SiPMs) are one of the key enabling technologies for large-scale LAr-based dark matter experiments. The experience from DarkSide-50, pushed to start an intense program for the development of innovative silicon-photomultipliers (SiPM) based photodetectors. SiPMs have a number of performance advantages over traditional PMTs, including higher photon detection efficiency (PDE) and much better single- photon resolution, all while operating at much lower bias voltage. SiPMs can also be efficiently integrated into tiles that cover large areas and feature better radio-purity than PMTs. Up to now, SiPMs are produced by FBK (Fondazione Bruno Kessler) developed in collaboration with DarkSide for low after pulsing and low dark rate operations in liquid argon. SiPMs are made of high purity silicon and are intrinsically radio-pure (electronic components are at the level of 60-100 μBq/kg).[33].
SiPMs are small size devices (tens to hundreds of mm^2) so in DS-20k they are grouped togheter in arrays of 25 cm^2, called tiles, with a cryogenic front-end board that pre-amplifies and aggregates all the signal to a single analog output. DarkSide-20k photosensor unit is a Photo Detector Module (PDM), consisting of a tile of 24 SiPM of the dimension of 12 mm x 8 mm covering a total area of 25 cm^2 operating as a single detector and working as a single channel (fig. 4.6). Besides the tile, each module will also contain a cryogenic preamplifier board that will amplify and shape the signal in the immediate proximity of the sensor. The output of the cryogenic amplifier will be passed on to a signal transmitter, also integrated into the PDM, and responsible for transmission of the signal through the cryostat penetration. The PDM

will also include the mechanical structure required to assemble all components. An intelligent power distribution system is also foreseen, capable of disabling individual PDMs in case of failure. Moreover, to avoid bubbling and excessive thermal load on the cryogenic system, the number of amplifiers for each PDM had to be minimised; the power dissipation for each PDM should not exceed 100 μW/mm^2. Considering all this, the DarkSide collaboration developed a custom made TransImpedence Amplifier optimised for an 87 K environment with parallel-series combination of SiPMs and decided a final configuration with a total of 4 TIA for each PDM. This hybrid ganging mode has been used to optimize the SNR, minimising the power dissipation[35].
In the final detector, there will be in total about 8280 PDMs (channels) which is equal to 198700 cryogenic SiPMs[36].

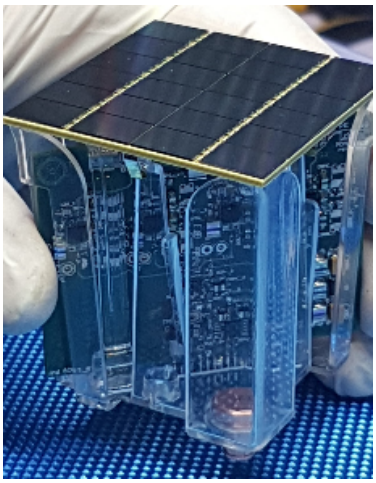

Figure 4.6. Picture of a DS-20k single channel PDM consisting of a 5 x 5 cm^2 tile of 24 SiPMs[36].

The main parameters of the SiPMs tile system for the TPC are given in table of fig. 4.7. The PDMs will be located above the anode and below the cathode, fully covering the top and bottom faces of the LAr TPC active volume, to detect both the S_1 and S_2 signals with high efficiency. The top and the bottom photon readout assemblies will consist of 4140 PDMs each. Multiple PDMs are mounted to a single motherboard to form larger basic mechanical units called the square board (SQB). The SQB is an array of 25 PDMs with an edge size of 25 cm. The SQBs are used to form the full readout planes (shown in fig. 3.8), for a total of 344 MBs covering the top and bottom of the TPC.
Following the successful construction of the first PDM in March 2018, the Photolectronics Working Group proceeded to the construction of the first motherboard, shown in fig. 4.8. SiPMs used for the construction of this MB are single dose cells of size 25 x 25 μm^2 and quenching resistor R_q value of 10 MΩ at 77 K. Each DS-20k motherboard, with PDMs biased at the same voltage, will be made of devices with similar R_q.
The tile and the front-end board PCBs were made with an Arlon 55-NT substrate. The tile PCBs were tested both at warm and at cryogenic temperatures to verify

the correct circuit impedance[34].

Parameter	Value
Number of PDMs	8280
Area covered by PDMs	$21\,m^2$
Area of one PDM	$50 \times 50\,mm^2$
Single PDM FE power consumption (specification/achieved)	250 mW/230 mW
Number of SiPMs per PDM	24
SiPM dimensions	$7.9 \times 11.7\,mm^2$
SPAD dimensions	$30 \times 30\,\mu m^2$
PDM overall photon detection efficiency	45 %
SiPM quench resistor R_q	5 MΩ
SiPM dark count rate density (specification/achieved)	$80\,mcps/mm^2/40\,mcps/mm^2$
SiPM total correlated noise rate (specification/achieved)	60 %/35 %
PDM fill factor (specification/achieved)	90 %/88 %
PDM SNR (specification/achieved)	8/24
PDM time resolution (specification/achieved)	10 ns/3.5 ns
PDM front end dynamic range (specification/achieved)	50 PE/100 PE
PDM dark count rate (specification/achieved)	200 cps/100 cps
PDM front end noise rate	<5 cps
Optical receiver power per channel	0.5 W

Figure 4.7. Photoelectronics design parameter for the TPC, produced by FBK[34].

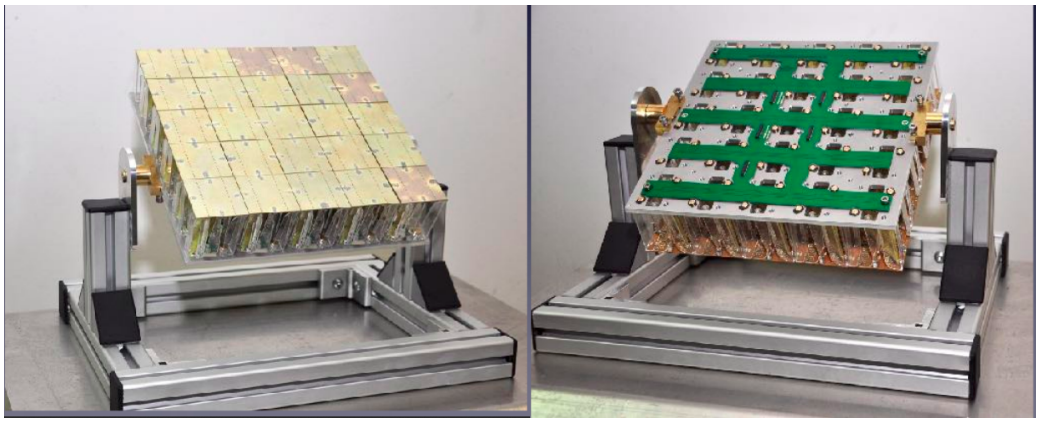

(a) **(b)**

Figure 4.8. Pictures of fron (a) and back (b) of DS-20k MB assembled with 25 PDMs.

The SiPMs will permit an higher Photo Detection Efficiency (PDE), an higher radiopurity and a more efficient assembly (i.e. better coverage, thanks to their compactness), if compared with standard PMTs. All these properties are fundamental for an experiment such as DS-20k, since the Pulse Shape Discrimination (PSD) is strictly related to the light yield. The SiPMs have also some limits like a high Dark Count Rate (DCR) and SNR, here defined as the ratio between the SiPM gain and the width of the baseline noise peak.

4.3 Darkside-Proto

The collaboration will benefit greatly from experience gained with DarkSide-50, however, DarkSide-20k will be more than two orders of magnitude larger in size and will use new technologies. The objective of the DS-Proto experiment is the construction and operation of a prototype detector of intermediate size (∼1 t), to fully validate the new DS-20k technologies for their integrity in both the mechanical and functional aspects. This prototype has the purpose to help to develop a better view of the overall project time-line and of the resources needed, both human and financial, and to help the integration of the various teams working on the different DarkSide sub-systems.
The program for DS-Proto consists of three different phases:

1. Design, construction and assembly at test site of the LAr TPC, with the size available for two motherboards integration;

2. Integration of 50 preproduction PDMs to the LAr TPC; assembly, commissioning, and operation of full read-out and DAQ for 50 PDMs; The xy resolution and S2 gas pocket optimization will be done during this phase.

3. Assembly and commissioning of full system, including 250 first production PDMs; full readout and DAQ operational; evolution towards final configuration.

In August 2017 the collaboration and LNGS reached and finalized an agreement with the Accelerator & Technology Sector of CERN to carry out the first surface operation of DS-Proto at CERN before moving the detector to LNGS[34].
A cryostat for DS-Proto has been built by Tecno Alarm, s.r.l., Roma, and delivered to CERN in August 2018. The 1 mBq/kg U/Th AISI 304 L Stainless Steel was procured from NIRONIT Edelstahlhandel GmbH & Co and it is good enough to be used for a possible physics run at LNGS. Assembly and test of the DS-20k cryogenics is taking place at CERN.
Full characterization of the prototype in terms of physics performance for both ionization and scintillation measurements for low energy events, relevant for dark matter searches, would require a dedicated commissioning run underground at LNGS. The detailed program of the activities to be carried underground and a plan for a temporary installation is under study.

4.3.1 DS-Proto TPC

The DS-Proto TPC mechanics, including the structural elements, the field cage, the reflector cage, the transparent cathode, the transparent anode (also serving as a diving bell for the containment of the gaseous phase), the SiPM PDM assemblies, the high-voltage feed through system, will all be built utilizing, on a scaled down overall dimension, the same design and construction techniques foreseen for the baseline of DS-20k (fig. 4.9).

The PDMs will be arranged to cover part of the top and bottom of the TPC in a cross pattern. Both top and bottom planes consist of 125 PDMs. e tested on a significant number of channels with this detector. The DS-Proto PDMs are

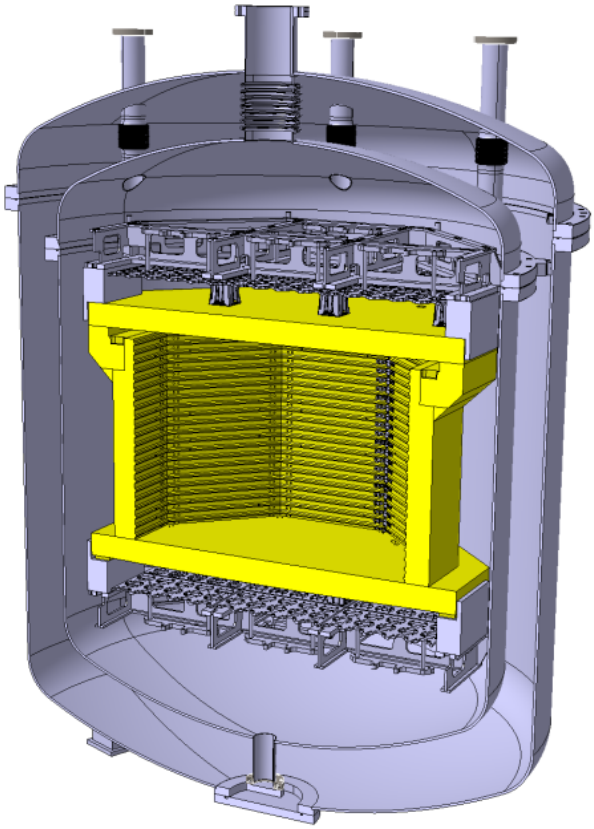

Figure 4.9. Design of the DS-Proto detector[34].

contained in 5 SQBs on top and an identical set on the bottom. With both planes, the DS-Proto TPC requires 250 PDMs. The first Motherboard, made of 25 PDMs, was just assembled.
Since DS-Proto is a test bench of DS-20k, it won't be used to demonstrate the material radio-purity requirements of DS-20k. However, it will be built with the goal of achieving the best radio-purity conceivable at the time of the construction, based on the current results of materials assay campaign. Additionally, DS-Proto can be used to assess the possible contamination related to the detector construction procedures (TPC and PE), evidencing material cleaning/handling issues.
The validation of the predictions concerning the neutron/gamma originated by the material contamination will be only possible through data taken underground with the DS-Proto deployed in a properly shielded environment.

4.3.2 Proto-0 at CERN

Upon successful completion of the test phases of the different parts, we plan to measure the overall performance of the DS-Proto through some key parameters, such as the S_1 light yield, the electron drift time, electro-luminescence field and gas pocket thickness uniformity for high resolution of S_2 signals and the xy position reconstruction. For the purpose of optimizing the S_2 signals, the first two Moth-

erboards will be assembled into a small TPC with reduced size drift length. This detector is referred to as **DS-Proto-0**. Currently a TPC equipped with only one mockup MB above the anode has been built and is undergoing test in LAr (fig. 4.10), at Building 182 of CERN. The TPC is 30cm x 30cm x 20cm, put in a liquid argon vessel. The height of the TPC is divided into 12 cm of drift volume containing liquid argon (10 kg), 1 cm the space between the wire grid and the anode (7 mm the gas pocket + 3mm the thickness of the liquid above the grid) and 1 cm between the TPC and the panels of the vessel. The trasparent panels are made of PMMA while the other are stainless steel[43]. The motherboard was built in 2019 and consists of two PDM families, made up of one dose and triple dose (size 25 x 25 μm^2 and R_q = 10 MΩ at 77 K) SiPMs. In fig. 4.11 and 4.12 pictures of the Proto-0 TPC from different angles are shown.

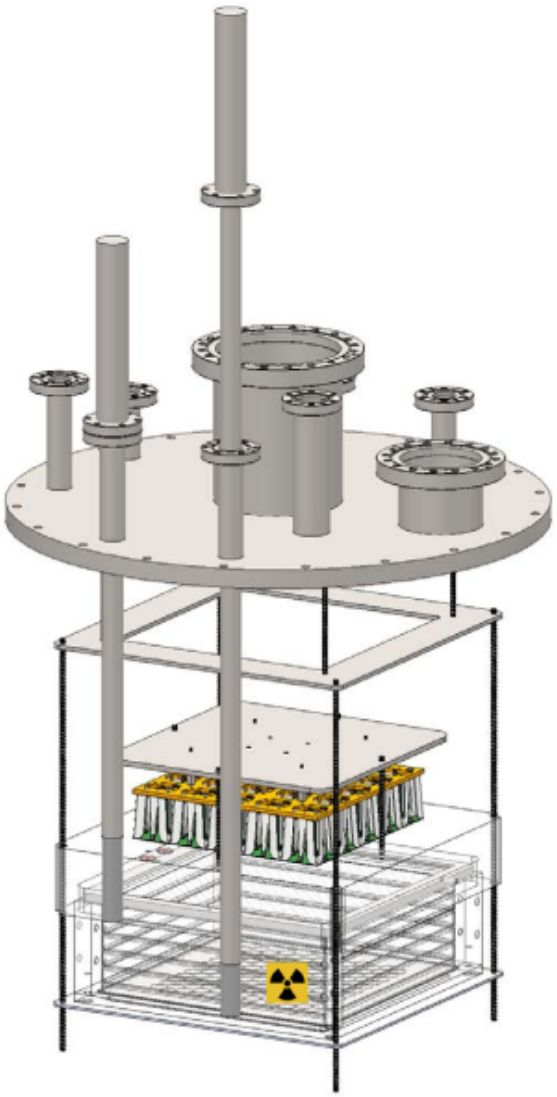

Figure 4.10. 3D model of the Proto-0 system at CERN. It is also shown the γ source for PDMs calibration is shown[43].

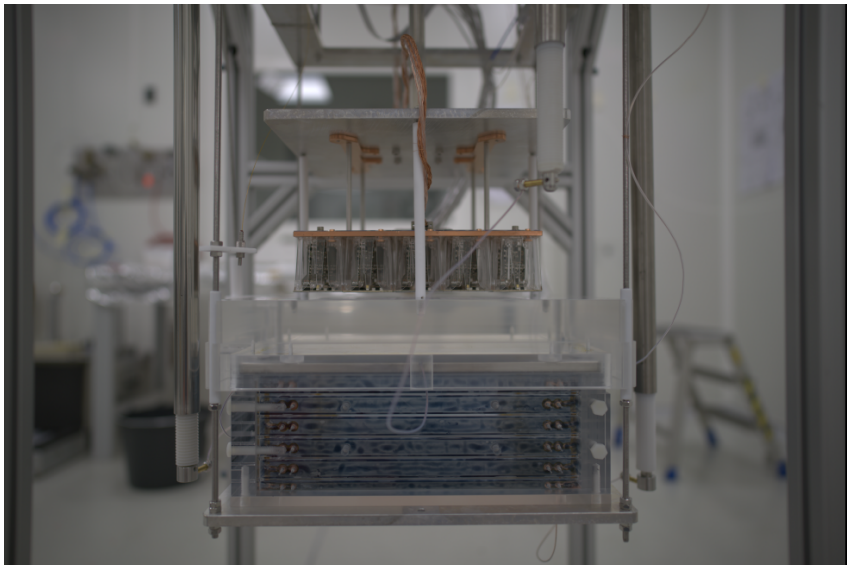

Figure 4.11. Picture of the Proto-0 TPC[37].

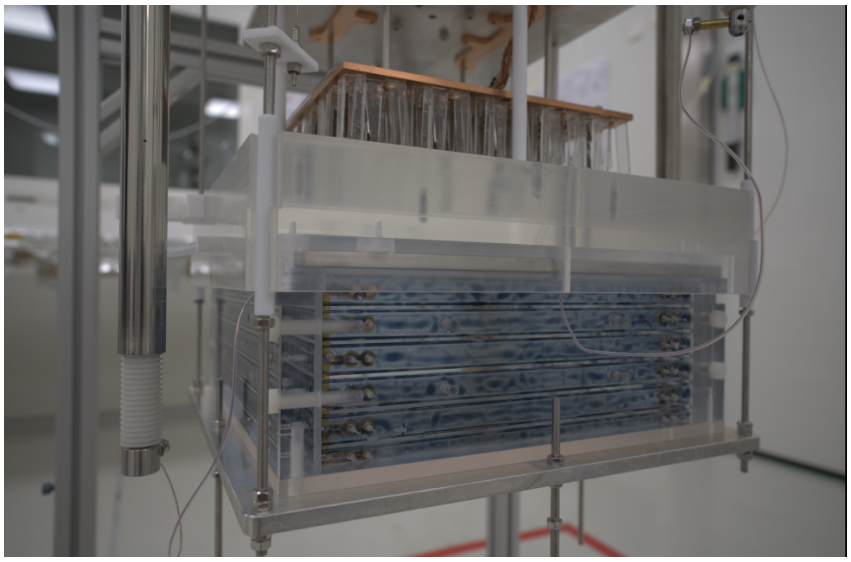

Figure 4.12. Finale scheme of Proto-0 with both motherboards[37].

Full tests of the S_1 response and therefore of the SiPM readout chain can be obtained at the surface by switching off the electroluminescence field. The configuration of the gas pocket (geometry and field) can be varied by changing the distance between the anode and the wire grid, the width of the gas pocket, as well as the electro-luminescence field. The S_2 pulse shape can be precisely studied along with different gas pocket configurations, aiming to provide us the best solution for the future LAr TPC design. This set-up will also allow for early studies of the S_2 formation and readout, to be carried out while the pre-production of the remaining Motherboards of the prototype is ongoing. The final set-up is shown in fig. 4.13[36], equipped with two MBs.

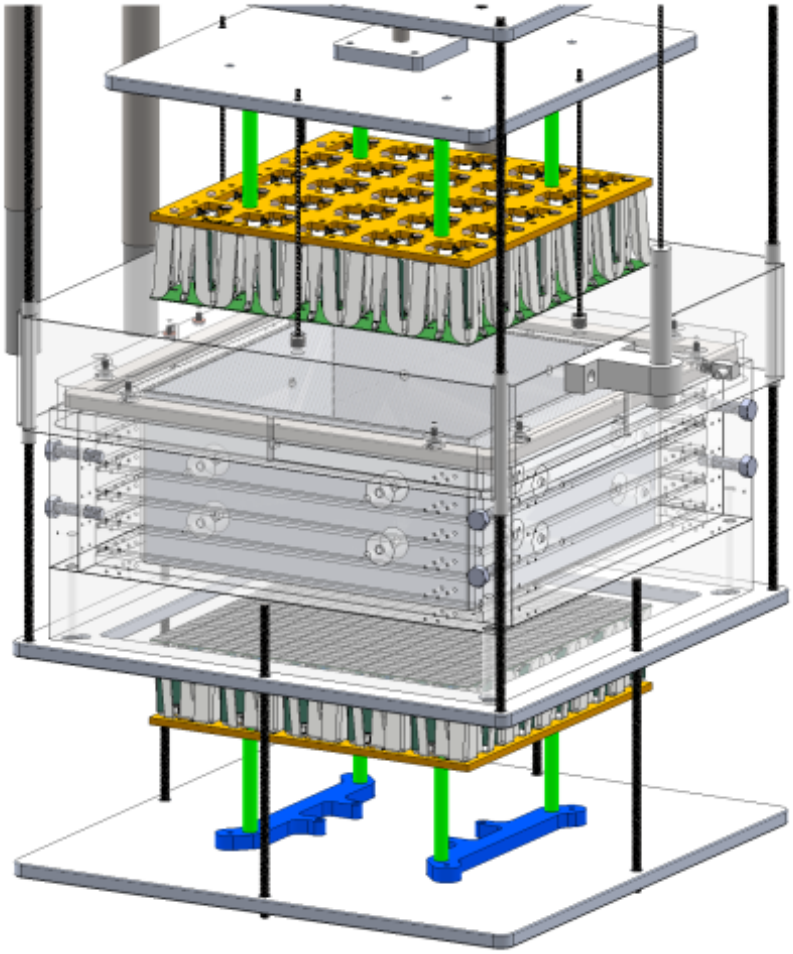

Figure 4.13. Final scheme of Proto-0 with both motherboards[36].

4.3.3 DAQ System

The current design for the DS-20k electronics and its data acquisition system (DAQ) accommodates both the large number of sensors and the long drift-time (expected maximum electron drift time is 4 ms) of the LAr TPC, as well as the readout of the Veto detector.
The baseline scheme for the TPC and Veto detector DAQ electronics hardware foresees an optical signal receiver feeding a differential signal to a flash ADC digitizer board that is connected to a large Field Programmable Gate Array (FPGA). The digital filtering capability within the digitizer board would allow the discrimination of single photoelectron signals and a first determination of the time and charge of the individual channel pulses. Data from signal pulses in the TPC and veto detector will be transferred to the front-end data processing units where further data reduction may be performed. Finally, the data will be passed to an online event building processor that will select interesting events and write them to permanent storage, performing additional data reduction to save finally on permanent storage a suitable

small set of data for each event yet not compromising physics performances.
In normal data-taking mode, an event could be identified by a coincidence of hits in the TPC within a specified time window. A coincidence of 7 hits in 200 ns would result in a random trigger rate well below 0.1 Hz. Nuclear recoil events at the trigger threshold, producing about 15 PE in 5 μs, would result in the collection of 6 pe to 8 pe within the first 200 ns. Thus, the trigger would be 100% efficient for the WIMP-like signals of interest. The event building and software trigger stage is realized with modern commodity CPUs and connected via Ethernet with the front-end DAQ processors.
Synchronization between the TPC and Veto DAQ is fundamental for the effectiveness of the design, and will be provided and maintained during the data taking. The clock source of the TPC DAQ will be used as reference and digital signals will be generated to uniquely identify each event regardless of the trigger origin or the detector. A pulsed signal distributed to all the modules will be used to check and correct the alignment of each channel among the TPC and Veto detectors.
The DAQ system will be located on top of penetrations on the roof of the AAr cryostat. The arrangement will allow personnel access while minimizing the length of the optical fibers used to transmit the data from the TPC and Veto to the signal receivers.

Digitizers

The basic readout element of the proposed DS-20k DAQ system is a multi-channel board hosting several flash ADCs (fADCs) linked to a large FPGA for digital signal processing. This will be connected to a host CPU for control, monitoring and data formatting using as an output channel through a 1 Gbit/s to 10 Gbit/s Ethernet connection to an external computer. The fADC will have 14 bits resolution and 125 MHz sampling speed.
A DAQ system for the initial prototype TPC tests has been deployed at CERN in order to acquire data from up to the PDM motherboard, amounting to 25 PDM channels.

DAQ Software

The Maximum Integrated Data Acquisition System (MIDAS)[34] has been chosen as a framework for developing the DAQ readout and related online control software for the DS-20k detector, and together with the CAEN hardware provides a nice baseline for the digitization and recording of the raw data. A collaboration between the MIDAS and CAEN developers has been established to ensure that the interfacing of the front-end hardware is compatible with the back-end hardware and software that will ultimately compile and write the data to permanent storage.
The DS-Proto readout will be, in the first phase, based on 5 CAEN VME-V1725 fig. 4.14 and a custom trigger module developed by the TRIUMF group. This system has been already installed at CERN in the first part of 2019 in order to provide the DAQ system for the first 25 channels (1 motherboard) of Proto-0. In a later stage, the readout for DS-Proto will be based on the new digitizer boards from CAEN, previously described.

Figure 4.14. 5 CAEN VME-V1725 module[38].

Chapter 5

Study of SiPM performance with Proto-0 data

Silicon photomultipliers (SiPM) have huge performance advantages compared to PMTs and for this they represent a fundamental tool in the search for new physics by the future DarkSide-20k experiment. As previously mentioned, these detectors are installed in Proto-0 and grouped in 25 PDM modules installed on a motherboard located above the anode of the TPC.
The SiPM calibration operation of the prototype is a crucial step, since the same procedure will then be repeated on the thousands of DS-20k modules, and its success will contribute to maximize the apparatus efficiency in detecting a WIMP signal. For this purpose, in November 2019, a data collection took place at CERN using laser and ^{241}Am as physical signal sources. First of all, it is necessary to fully understand the response of PDMs to these inputs by studying their characteristic parameters. An ARMA (AutoRegressive-Moving -Average) algorithm allows to filter the waveforms acquired with respect to the noise and therefore to reconstruct the peaks corresponding to signal events. In this context, it is very important to optimize the filter performance, so as to reconstruct the pulses released in the SiPM with the greatest efficiency: by means of the data acquired in laser mode, the filtered waveforms are subjected to an appropriate fit procedure in order to extract the parameters of the templates and assess them to study the *signal-to-noise ratio* (SNR) of all the channels of the motherboard.
A further check consists in observing the effect that the fit has on the measurement of the electrical charge of the signal and on the hits reconstructed by the peak finder. The study of the *dark count rate* (DCR) carried out on ^{241}Am runs with different power supply voltages of the PDM is subsequently described
. The chapter closes by observing the event characterized by the simultaneous occurrence of signals S_1 and S_2 from a run with source ^{241}Am.

5.1 Laser and ^{241}Am data

During the period between 31st October and 18th November 2019, the acquisition of many runs of data collected by the SiPM of the Proto-0 motherboard took place. Two different signal sources were used:

Laser : it is an Hamamatsu laser diode PLP-10, which emits pulses 50 ps long, with a wavelength of 403 nm. The light was inserted in the dewar through a bunch of optical fibers and then it was diffused bythe acrylic windows. An optical fiber enters from a passer-by and it is put in contact with the acrylic of the anode (above which the motherboard is positioned). The light bounces several times inside the acrylic (which works as a diffuser) and comes out hitting SiPMs[42]. Photons are emitted by the laser with the fixed frequency of 1 kHz, according to the Poisson distribution $P_\lambda(n) = \frac{\lambda^n}{n!}e^{-\lambda}$, where λ is the mean number of emitted photons that depends on the supply voltage of the laser and n the number of emitted photons. Runs with this source are taken to study single hit response of SiPM. Maximum and minimum laser intensity modes are avilable.

^{241}**Am** : is an highly radioactive americium isotope with an half-life of 432.2 years that decays mainly by α decay, with a weak γ-ray byproduct: $^{241}_{95}Am \rightarrow {}^{237}_{93}Np + \alpha + \gamma$. The α decay energies are 5.486 MeV 85% of the time, 5.443 MeV for 13% and 5.338 MeV for the remaining 2%. The γ ray energy is for the most part 59.5409 keV[39]. The source is deposited in a metallic collimator 2 cm thick on the mesh located at the bottom of the TPC (fig. 5.1.a). The mesh is 30 cm X 30 cm, 0.5 mm thick, made of stainless steel. The area for source deposition is only the center 25 cm X 25 cm, upper surface (fig. 5.1.b)[43]. The material surrounding the source shields the α particles produced by the decay so as to see only the signal due to the photons in the LAr. The interaction of the gamma with argon in the TPC gives rise to both excitation and ionization of atoms: primary scintillation signals are generated in the liquid (S_1) and secondary scintillation signals are originated in the gas due to the electrons that drift in the liquid afterionization of the LAr atoms (S_2), allowing the study of both. This source is always present for all acquisition runs.

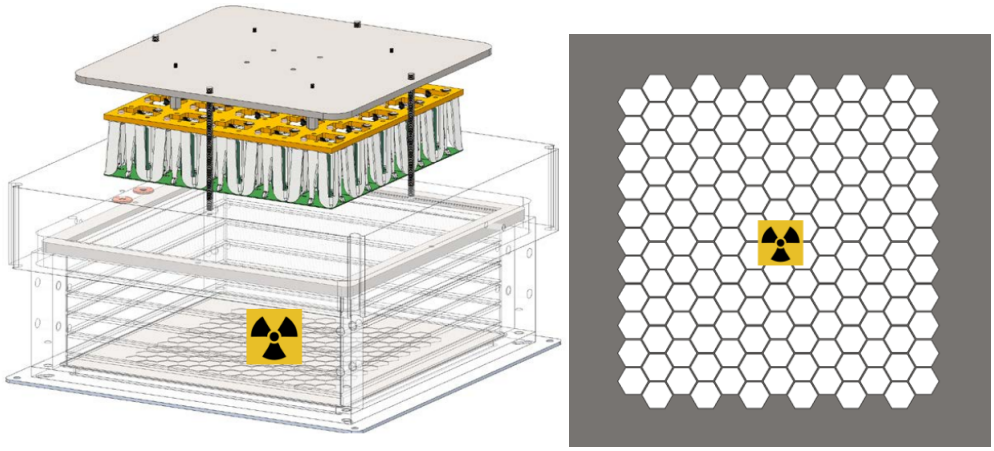

(a) **(b)**

Figure 5.1. 3D recostruction of TPC with the source on the bottom (a) and mesh where the source is located (b).

Data collection took place through the following operations that led to the acquisition of runs with specific characteristics:

Noise measurement : the source is ^{241}Am; they were acquired with runs with different voltage values: overvoltage (67 V), standard voltage (65 V) and below breakdown threshold (50 V); the trigger is at a fixed frequency of 50 Hz and the acquisition window is defined as 10 μs;

Laser run for 1 pe calibration : the acquisition window is fixed at 12 μs (5 μs pretrigger) and the trigger frequency is constant and given by the laser clock (1 kHz). Runs with both minimum and maximum laser intensity were acquired in order to illuminate all PDMs;

Single-phase TPC : the source is ^{241}Am; the goal is to determine the response of the PDMs to S_1 events (the gas pocket is off) for different values of the electric fields and different trigger thresholds; the acquisition window is 30 us (9 us pretrigger) and the supply voltage 65 V;

Dual-phase TPC : the gas gap is produced in order to produce the S_2 signal; the acquisition window varies from 100 to 1000 μs and the trigger is variable. The power supply voltage is fixed at 65 V; data have been acquired with different electric field values.

This large amount of data was acquired with the MIDAS DAQ system[40] and stored in EOS, the low-latency disk-based storage service available at CERN. Through the pyproto software framework written in python3 it is possible to reconstruct and subsequently analyze the data, both from lxplus and from Swan: the first is an interactive logon service for all CERN users, which consists of public machines made available to the department IT (Information Technology) for interactive work; the second is a data analysis platform that uses codes in jupyter notebook for more dynamic tests.

5.2 Parametrisation of SiPM response

A lot of data was acquired for different configurations of both DAQ system and the experimental setup, in order to allow a broad and detailed study of the signal collected by the SiPM.
First of all, it is important to understand the parameters that characterize the response of the SiPM to a laser pulse: this is the starting point to be able to reconstruct the photodetector templates. Figure 5.2 shows an event collected for the laser run 888: the single output pulse of the specific PDM 5 of the motherboard is observed in response to a certain number of photons emitted by the laser. This pulse is obtained after applying the *baseline subtraction*: the voltage received by the detector is negative (fig. 4.1.b, see cap. 4) and it has a certain offset: it is made positive and the offset is subtracted. Each PDM of the motherboard (see fig. 5.3) has been associated with a DAQ channel, according to the criterion shown in table 5.1. Time on the x-axis is expressed in samples. The sampling rate of the DAQ is

250 MS/s (Mega samples/seconds), therefore each sample corresponds to a time of 4 ns: from this it is deduced that the time window in 5.2 is 9 μs long. The signal voltage is in ADC units. The interval shown in figure 5.2 is divided into three time subintervals: an interval 0 - 850 samples before the peak; an interval 1900 - 2250 samples after the peak; the interval 850 - 1900 samples in which the peak is placed. The intervals on the side are far enough from the peak for the signal to be given only by the fluctuation of electronic noise around the value 0 ADC. This part of the waveform is called *baseline*. In the central interval, the effective response of the SiPM to the physics event is observed, in this case the photons emitted by the laser source.
The peak consists of two components: a very fast Gaussian part, which corresponds to the SiPM discharge phase; a slower part, corresponding to the charging phase.

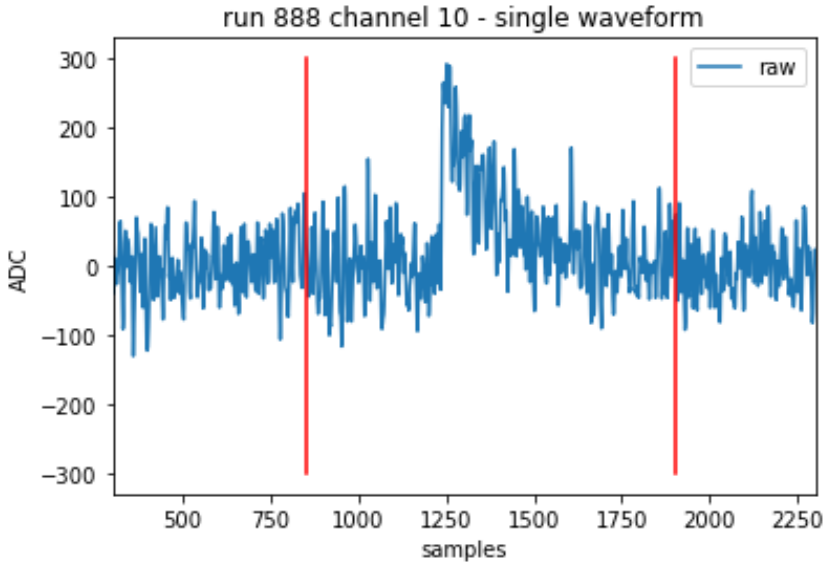

Figure 5.2. Response of DAQ channel 10 (PDM 5) of laser run 888. The two vertical red lines divide the time window of the event into three subintervals: on the side the baseline and in the center the peak of interest, with trigger time =1252 samples (5.008 μs) given by laser.

PDM id	0	1	3	4	5	6	7	8	9	10	11	12	13	14	15	16	17	18	19	20	21	22	23	23	24
DAQ channel	0	2	4	6	8	10	12	16	18	20	22	24	26	28	32	34	36	38	40	42	44	48	50	52	54

Table 5.1. Table of PDMs number with relative DAQ channel.

The function that well represents the SiPM response is a convolution of a Gaussian and a decreasing exponential:

$$g(\tau) = \int_0^\infty e^{-t/\tau} e^{\frac{(t-\tau)^2}{2\sigma^2}} dt. \tag{5.1}$$

The parameters that therefore define the response of the SiPM are:

- the τ decay time of the slow component;

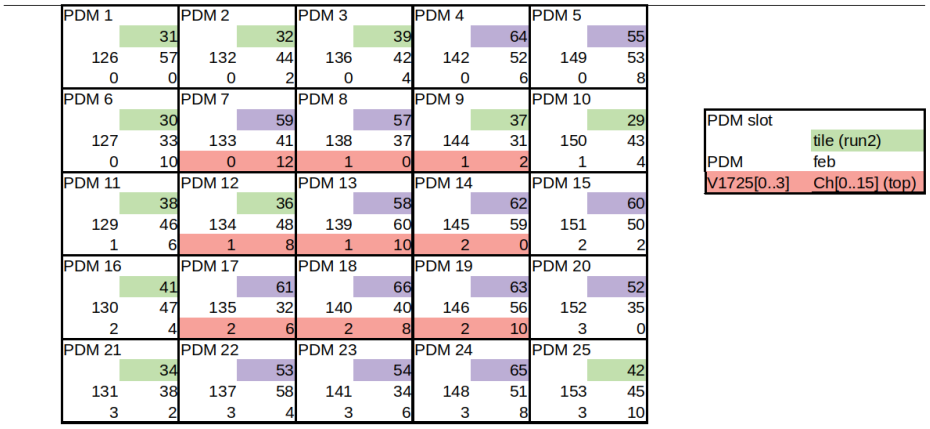

Figure 5.3. PDM matrix of Proto-0: green and violet indicate PDM of the two different families constituting the motherboard; in red are showed channels in coincidence used as 'OR' of the trigger[44].

- the σ of the Gaussian which represents the fast component;
- the fraction $fslow$ of the charge of the slow component, i.e. the fraction of the slow component of the waveform on the total integral of the waveform;
- the peak $offset$, i.e. its time position;
- the amplitude of the *baseline*, i.e. the average height of the waveform far from the peak;
- the *height* of the peak, calculated with respect to the baseline.

SiPM response parametrisation is a first step towards understanding the observed events, allowing their reconstruction and subsequent optimization of this mechanism, with the ultimate goal of determining the nature of the detected signal with maximum efficiency.

5.3 Hit finding

This section describes the SiPM waveform reconstruction algorithm. It is divided into two phases:

1. filtering of the raw waveform;
2. peak finding of the hits on the top of waveform.

Both operations are performed by an ARMA algorithm. First, the raw waveform output to a PDM for a given event is subjected to a filtering procedure: the aim is to reconstruct the original shape of the signal including noise so as to subsequently measure its characteristic parameters. The filter initialisation parameters are σ, τ, $fslow$ and the sampling rate, constant at 0.250 GS/s. The algorithm then simultaneously filters the Gaussian component with a Gaussian filter with sigma =

σ and the slow one with a filter using the information given by the input τ. The two filtered parts are subsequently rescaled appropriately through the parameter $fslow$ (slow part * $fslow$ and fast part * (1-$fslow$)) and finally the sum between them is done. Figure 5.4 shows waveform of figure 5.2 with the filter applied to it superimposed, obtained using the initial test parameters $\sigma = 7.5$ ns, $\tau = 565$ ns and $fslow = 0.94$.

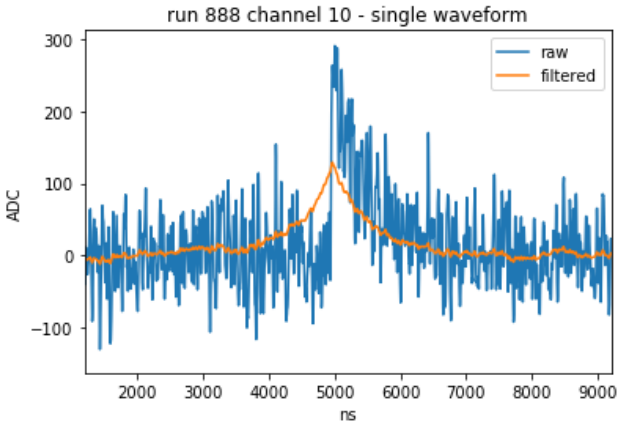

Figure 5.4. Response of DAQ channel 10 (PDM 5) of laser 888 with filter superimposed using template parameters $\sigma = 7.5$ ns, $\tau = 565$ ns and $fslow = 0.94$.

Now that the signal has been cleaned of noise, the goal is to find the hits on the filtered waveform, that is to reconstruct the events that give rise to the observed signal. The function that deals with this phase accepts as input the following parameters, which represent the identification requirements of an hit:

- *height*: only signals with a minimum height are classified as hits;
- *prominence*: it is the height of the peak in relation to its relative baseline (figure 5.5); it is a very useful parameter to identify hits very close to each other. Prominence and height are dimensionless because they are relative to the filtered waveform.

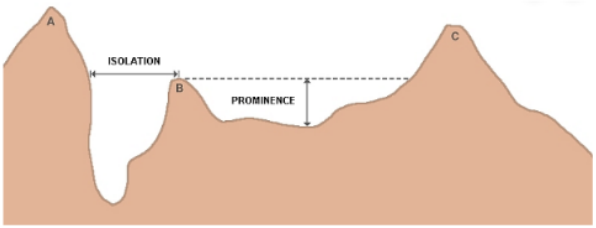

Figure 5.5. Illustration of the concept of prominence related to a peak[41].

- *distance*: two consecutive peaks must be at least a certain number of samples apart;
- *width*: minimum width of a peak, in samples.

Through these thresholds the peak finder recognizes in some points of the waveform the hits that respect the required selection, returning the information related to different parameters, including position, height and prominence.
Figure 5.6 shows the usual event of channel 10 of run 888 in which the hit identificated by the algorithm is plotted. The reconstruction of the hit took place by choosing as parameters of the peak finder *height* = 40, *prominence* = 10, *distance* = 1 , *width* = 1.

Peak finding turns out to be a very efficient algorithm when the signal is characterized by single hits or hits that arrive at times very distant from each other. The same cannot yet be said about the case in which peaks are very close to each other. In addition, the peak finder is applied to a filtered waveform: is it possible to optimize the filter, or to minimize the presence of noise from the waveform, in order to maximize the efficiency of the hit reconstruction process?
The following study tries to answer these questions.

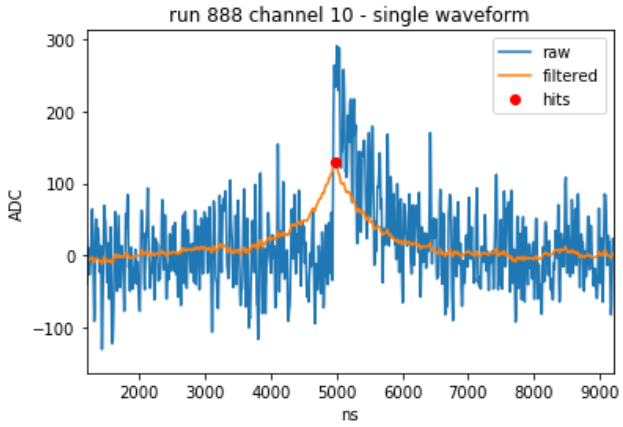

Figure 5.6. The peak finder algorithm identified an hit on this waveform of channel 0 of run 888; the parameters of the peak finder are *height* = 40, *prominence* = 10, *distance* = 1, *width* = 1.

5.4 Measurement of template parameters

An important study regarding the reconstruction of events is trying to improve the filter to reduce as much as possible the noise affecting the signal. As previously seen, it is possible to filter the waveform of a specific event detected by a channel using template parameters, up to now chosen arbitrarily. What is not known is how sensitive the filter is, compared to different template parameters and if therefore there is a way to find better parameters that allow more precise hit finding. For this purpose it was necessary to carry out a direct measurement of the template parameters proceeding according to the following strategy, applied to all the PDMs of the motherboard:

1. events are taken only from laser runs in order to study the response of the SiPM to the single photoelectron (pe) (figure 5.7);

run	SiPM tension (V)	laser intensity	trigger	trigtime (µs)	post-trigger (µs)	Time gate (µs)
888	65	MAX	external (500 Hz, laser at 1 kHz)	100	400	500
889	67	MAX	external (500 Hz, laser at 1 kHz)	5	7	12
891	67	MIN	external (500 Hz, laser at 1 kHz)	5	7	12
893	65	MAX	external (500 Hz, laser at 1 kHz)	5	25	30
892	65	MIN	external (500 Hz, laser at 1 kHz)	5	7	12
894	67	MAX	external (500 Hz, laser at 1 kHz)	5	25	30
963	65	MAX	external clock (laser set to 1 kHz)	5	7	30
964	65	MAX	external clock (laser set to 1 kHz)	5	25	30
966	65	MIN	external clock (laser set to 1 kHz)	5	25	30
978	65	MAX	external clock (laser set to 1 kHz)	5	7	12
979	65	MIN	external clock (laser set to 1 kHz)	5	7	12
1020	65	MAX	external clock (laser set to 1 kHz)	5	7	12
1021	65	MIN	external clock (laser set to 1 kHz)	5	7	12
1028	65	MAX	external clock (laser set to 1 kHz)	5	7	
1029	65	MIN	external clock (laser set to 1 kHz)	5	7	
1096	65	MAX	external clock (laser set to 1 kHz)	5	7	12
1097	65	MIN	external clock (laser set to 1 kHz)	5	7	12
1109	65	MIN		5	7	12
1110	65	MAX		5	7	12
1169	65	MAX	external clock (laser set to 1 kHz)	5	7	12
1170	65	MIN	external clock (laser set to 1 kHz)	5	7	12
1232	65	MAX	external clock (laser set to 1 kHz)	5	7	12
1233	65	MIN	external clock (laser set to 1 kHz)	5	7	12
1253	65	MAX	external clock (laser set to 1 kHz)	5	7	12
1254	65	MIN	external clock (laser set to 1 kHz)	5	7	12

Figure 5.7. Table with the list of laser runs used for the measurement of the SiPM response template parameters, with all the characteristics that specify them.

2. the filter is used to select waveforms with single hit events by initializing it with a set of approximate parameters;

3. a fit is made on the selected raw waveforms using different methods, with the aim of making them a measure of the characteristic parameters. The function designed for this operation is the convolution of a decreasing exponential with a Gaussian:

$$g(\tau) = \int_0^\infty \frac{1}{\sigma\sqrt{2\pi}} e^{-t/\tau} e^{\frac{(t-x_0)^2}{2\sigma^2}} dt. \tag{5.2}$$

   The input parameters of this function are σ, τ and $fslow$ and in addition the offset x_0, the baseline and the amplitude. The same parameters are then returned as output of the fit.

4. The stability of the parameters is studied in order to verify the goodness of the fit.

The fit procedures adopted are executed with five different techniques that fall in two different types of approach:

- simultaneous fit of 10 waveforms per channel;
- average waveform fit made on a large number of individual waveforms acquired by each PDM.

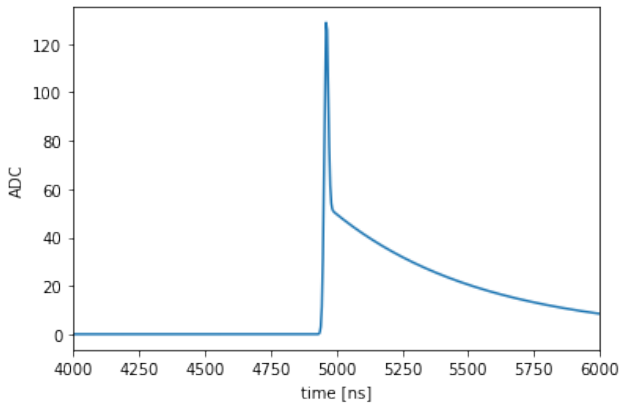

Figure 5.8. PDM template fit function with parameters $\sigma = 7.5$ ns, $\tau = 565$ ns, $fslow = 0.94$, $baseline = 0$ ADC, $offset = 4.96$ μs and $amplitude = 8000$.

Simultaneous Fit

This procedure is performed identically for:

1. low prominence events (50 - 100);
2. high prominence events (500 - 1000).

Figure 5.9 shows prominence distribution where it is possibile to see the correspondence between prominences and photoelectrons. The choice of different prominence thresholds is based on the desire to perform the best possible fit, and therefore the most complete analysis of the response of the PDM. Choosing a minimum prominence in the range 50 - 100 means requesting events with about one photoelectron, certainly present in all channels for each run of data, but affected by high electronic noise. Requesting events with a prominence threshold of 500 involves the selection of events with certainly more than one pe: the corresponding waveforms will be affected to a minimum by noise and this improves the quality of the fit, but these events will not be revealed in all channels due their position relative to the laser source. Furthermore, there may be the occurrence of *pileup*, two successive pulses separated by a too short interval, with a consequent deterioration of the quality of the fit.

Fit to average waveform

The methods conducted on the basis of this type of approach differ from each other in the nature of the waveform to which the average is applied:

1. individual waveforms;
2. individual waveforms after having shifted them by a certain amount, taking as reference the point where the cumulative function of the signal exceeds a chosen threshold;
3. individual waveforms after having shifted them by a quantity from a position x_0 extracted through a preliminary fit of the single waveforms.

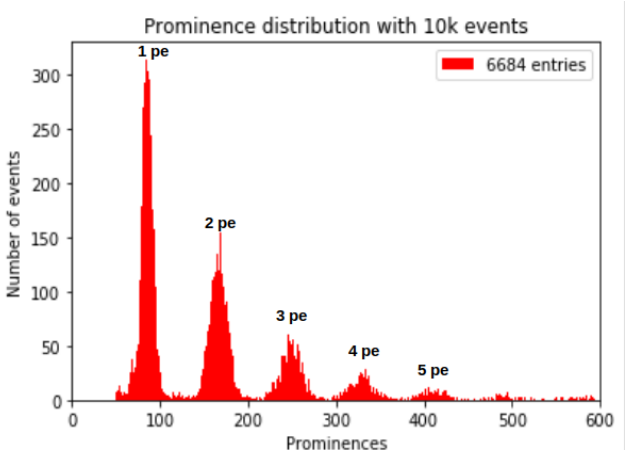

Figure 5.9. Prominence distribution: each peak has a mean value that corresponds to the prominence for a specific number of photoelectrons.

The idea behind bringing the individual waveforms to the same time position through shifting is trying to make the average waveform as clean as possible from noise fluctuations, and thus improving the quality of the subsequent fit.

Two of the five fit techniques adopted are described below, one for the two different types of approach:

- simultaneous fit for high threshold of prominence;
- fit of the average of waveforms shifted by x_0 obtained from a previous fit.

Simultaneous fit for high threshold of prominence

For the moment, only one channel of a particular run is considered.
The first selection of events occurs by initializing the filter with the approximate parameters $\sigma = 7.5$ ns, $\tau = 565$ ns and $fslow = 0.94$. 10 waveforms are then identified per channel in which there was only one peak, with a minimum prominence of 500 and at a time given by the laser clock, equal to 5.008 μs. Then the simultaneous fit of the waveforms that have passed the selection is performed, using the same filter parameters. Figure 5.10 shows the fit of a waveform taken from the DAQ channel 8 of run 888. We appreciate the high quality of the fit for this particular event.

Fit parameters	Measure	Errors	Initial
σ	2.04	0.049 (2.44%)	2
$fslow$	0.99	6.365e-06 (0.00%)	0.94
τ	116.55	0.056 (0.05%)	125
$\mathbf{x}_0$	1234.31	0.111 (0.01%)	1240

Table 5.2. Table of parameter extracted by fits of figure 5.10. Parameters are in samples.

However events with many photoelectrons can be affected by secondary peaks that occur in subsequent times little separated from the primary peak (figure 5.11). It is necessary to exclude these events from the statistics since they make the quality of the fit worse.

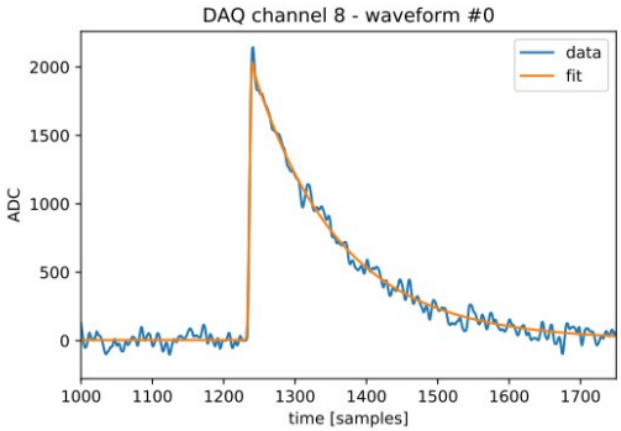

Figure 5.10. Waveform and superimposed fit for the DAQ channel 8 of run 888. The fit in this case is very good and follows the shape of the signal well.

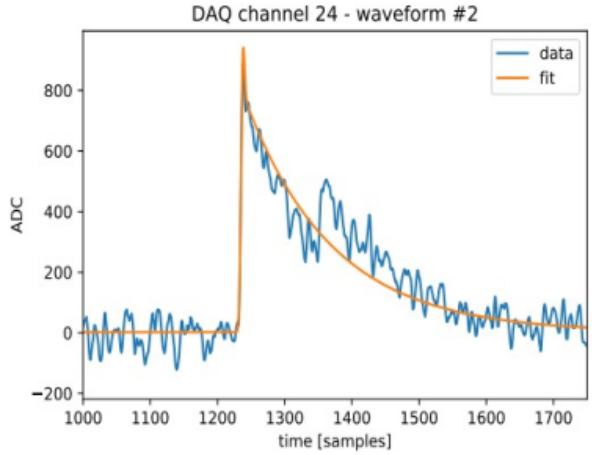

Figure 5.11. Waveform and fit superimposed on the DAQ channel 24 of run 888. The fit in this case does not have a good quality due to the secondary peak that occurs about 1000 samples later.

The fit returns σ, τ and $fslow$ for each PDM of the considered run. The procedure described so far for a specific channel of a specific run is repeated for all PDMs and all laser runs.
Figure 5.12 shows the distribution of σ, τ and $fslow$ in the PDM matrix, for the same run. The distribution appears rather random and does not give us any difference between the measurements based on the position of the PDM with respect to the source (arrow on the right).

The last step of the measurement procedure consists in studying the stability of the parameters over time, channel by channel. A constant trend with minimal fluctuations is expected. Figures 5.13 show the σ, τ and $fslow$ plots for the DAQ channel 8 as a run function. When a value deviates a lot from the flat trend, it gives the idea of a bad measure. However this condition is necessary but not sufficient about a possible problem with the fit: to see if something is wrong it is always good

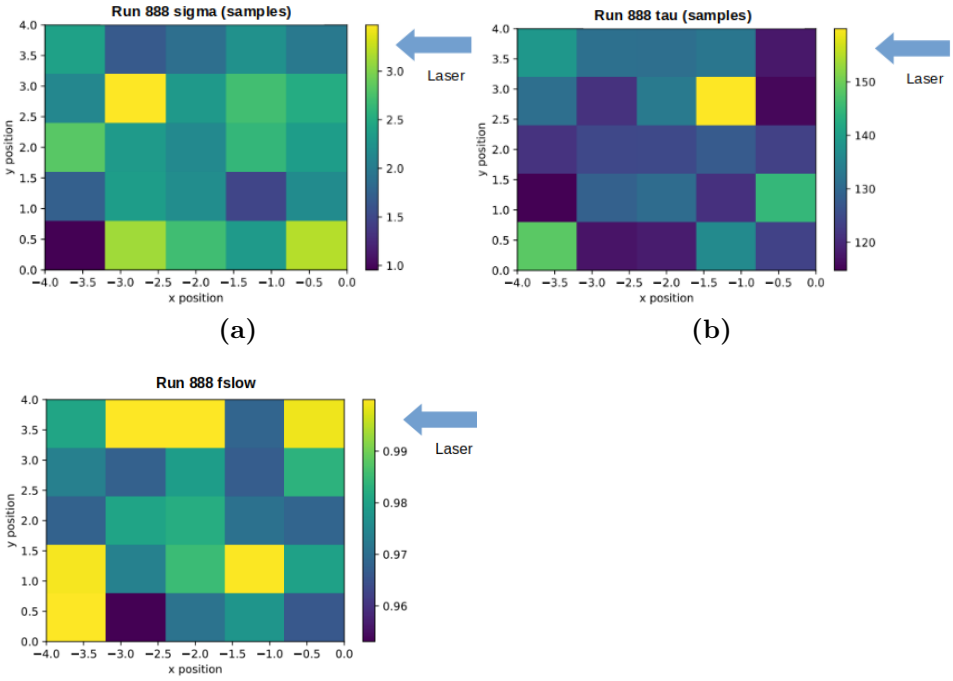

Figure 5.12. Distribution of σ (a), τ (b) and $fslow$ (c) on the PDM matrix, for run 888.

to carefully observe the waveforms plots with the superimposed fit.

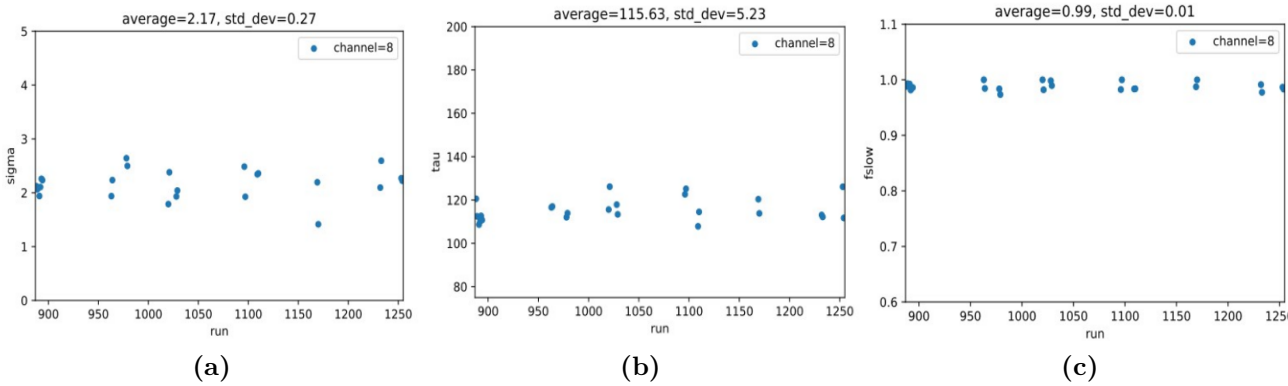

Figure 5.13. Plot of σ (a), τ (b) and $fslow$ (c) vs runs for DAQ channel 8. Above average and standard deviation are shown for every parameter. σ and τ are plotted in samples.

Ultimately, the plot of the average values of each parameter as a function of the PDM is generated, where the error bars are the standard deviations of the parameters (figure 5.14). An high value of the standard deviation suggests a bad measurement occurred for a given channel, but also in this case it is a necessary and not sufficient condition, since an high error could go back to only one of the runs for which there is a bad result. The two colors represent the two types of PDM

used for the Proto-0 motherboard: no substantial difference is observed between the two families of channels from the point of view of the stability of the measured parameters.

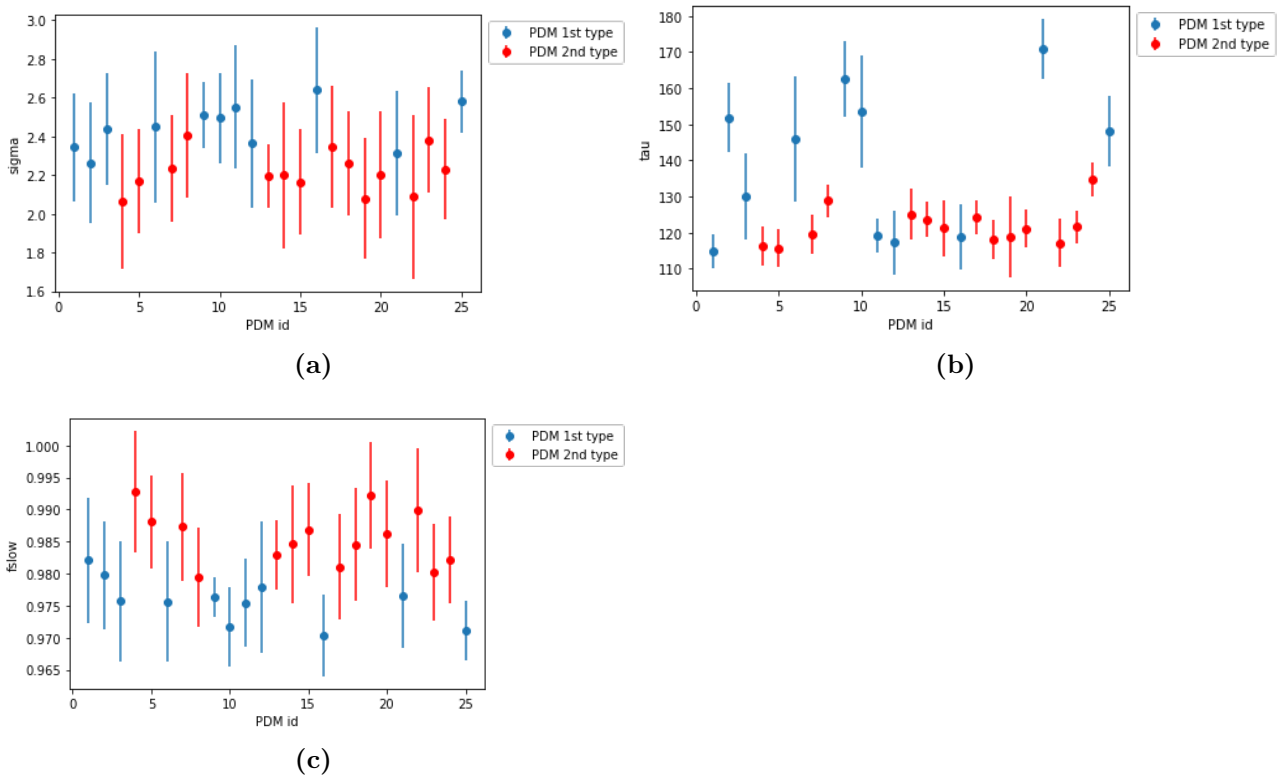

Figure 5.14. Plot of σ (a), τ (b) and $fslow$ (c) vs PDM id. Two different colors refer to two different families of PDMs used installed on the motherboard. σ and τ are in samples.

Fit of the average of waveforms shifted by x_0 obtained from a previous fit

For the moment, only one channel of a particular run is considered.
The first selection of events with the filter takes place using the approximate parameters $\sigma = 7.5$ ns, $\tau = 565$ ns, $fslow = 0.94$. An high number of waveforms is selected (40 - 560) requiring the presence of a single peak, with a prominence in the range 50 - 100 (events with 1 pe), with a trigger time given by laser (5.008 μs). Each waveform is fitted by initializing the parameters to the same values as the filter and the offset x_0 of each peak is then extracted. Each individual waveform is shifted by an amount x_0 - t, where t = 4.8 μs is an arbitrary time. The individual shifted waveforms are then averaged. Finally the average waveform is fitted with the same initial parameters and the final parameters are measured. This procedure is performed on all PDMs for all laser runs. The figure 5.15 shows the fit of the average waveform for channel 0 of run 1020.

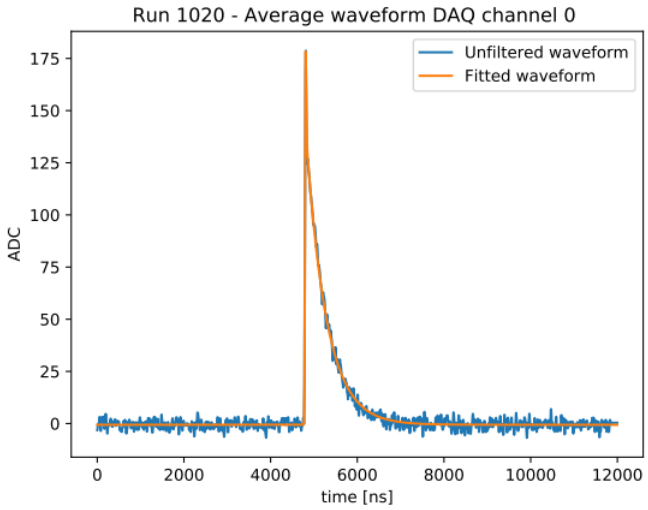

Figure 5.15. Average waveform and fit for DAQ channel 0 of run 1020.

Fit parameters	Measure	Errors	Initial
σ	2.91	0.042 (1.47%)	2
$fslow$	0.96	7.803e-04 (0.08%)	0.94
τ	116.71	0.504 (0.43%)	125
$\mathbf{x}_0$	1200.54	0.051 (0.00%)	1240

Table 5.3. Table of parameter extracted by fits of figure 5.15. Parameters are in samples.

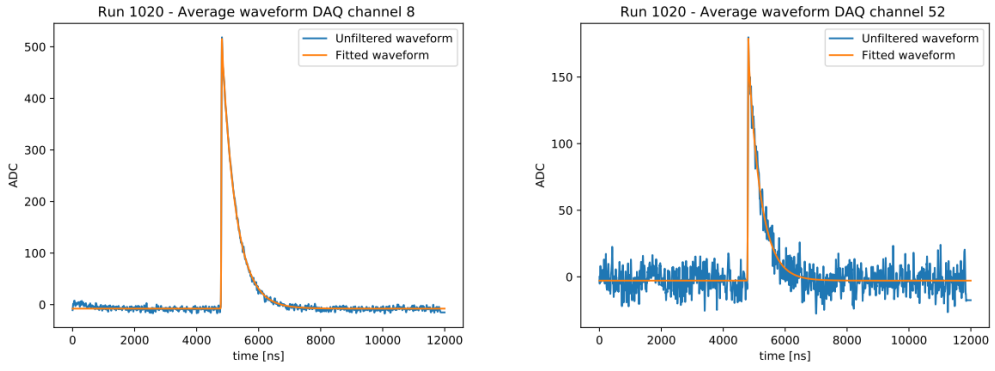

(a) **(b)**

Figure 5.16. Run 1020. Waveforms and fit for two high occupancy channels: for ch 8 (a) are selected high prominence events and many events are found (194 events); for ch 52 are selected low prominence events and for that few events are found (40 events).

It is observed that for some channels the waveforms are strongly affected by fluctuations: this is due to the few events found on them and the average therefore applies to a few cases. The cause of this lies in the fact that some PDMs have an high occupancy, i.e. they see an higher average number of pe than other channels and therefore, for such PDMs, events in a range of low prominence are observed less

frequently. For those channels, events with prominence in the range 200 - 300 are then selected (fig. 5.16).

Figure 5.17 shows the distributions of σ, τ and $fslow$ in the PDM matrix for run 1020. Also in this case one does not observe any strong correlation between the values of the measured parameters and the position of the PDM in the motherboard.

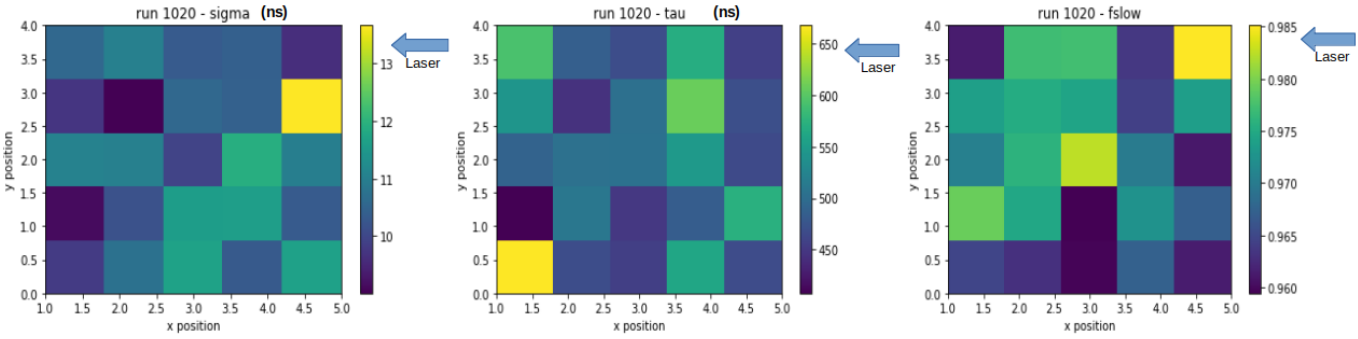

(a) (b) (c)

Figure 5.17. Distribution of σ (a), τ (b) and $fslow$ (c) on the PDM matrix, for run 1020.

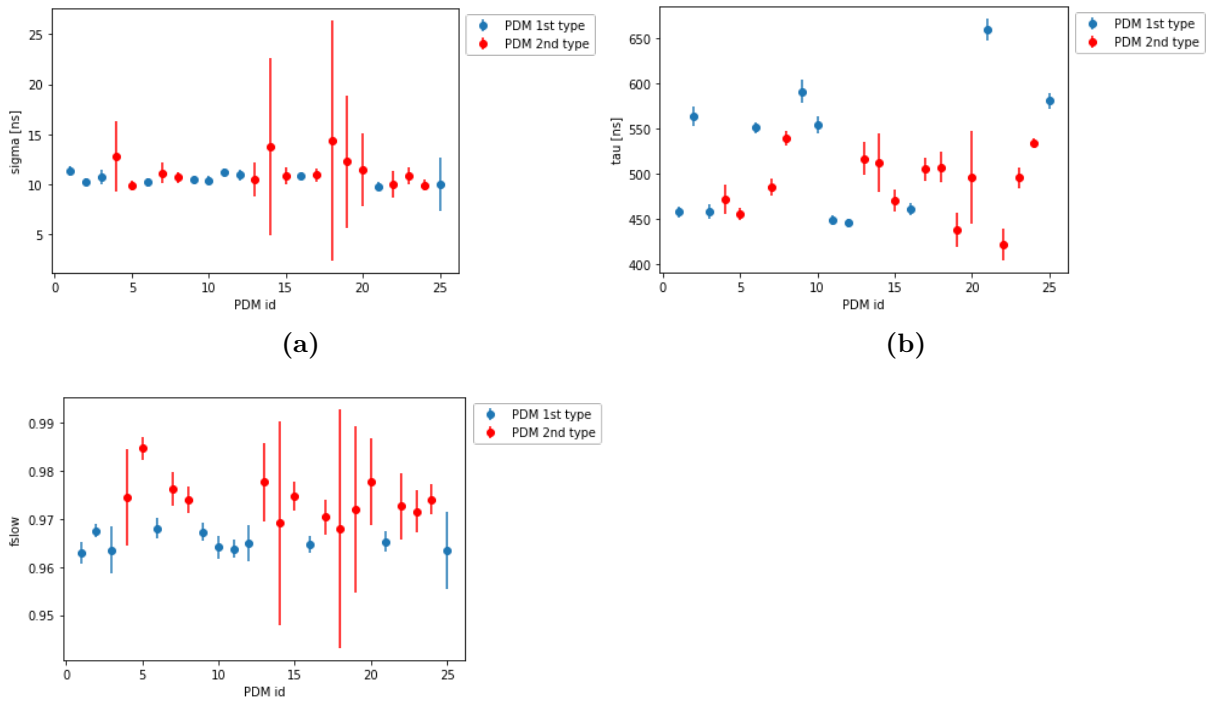

(a) (b)

(c)

Figure 5.18. Plot of σ (a), τ (b) and $fslow$ (c) vs PDM id. Two different colors refer to two different families of PDMs used installed on the motherboard. σ and τ are in ns.

The stability study of the parameters over time is carried out for each PDM, obtaining the plots of figure 5.18 on which it is possible to make the same considerations

made for the previously described method.

It has been observed with regard to this procedure that modifying the initial offset value in the preliminary fit used to extract the time x_0 the same fit turns out to change significantly. Two different offset values have been tested: $t_1 = 4.96$ μs and $t_2 = 4.98$ μs. Take two single waveforms from run 1020 as an example. Take the first waveform and fit to it with two identical templates which, however, differ only in the values t_1 and t_2 (fig. 5.19.a): the two fits coincide and in both cases the Gaussian part follows the true peak of the signal (fig. 5.19.b). The same measured values are obtained from both fits (tab. 5.4).

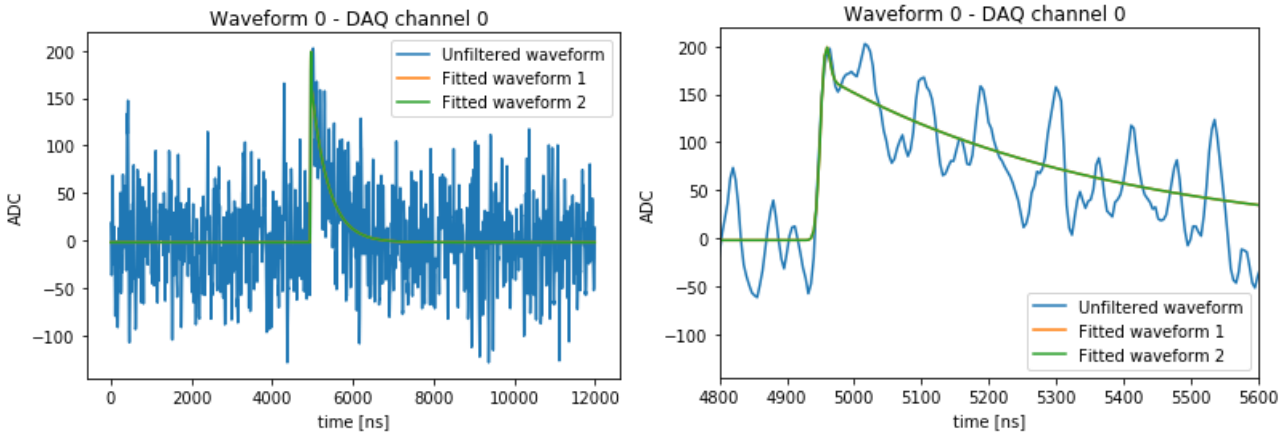

(a) **(b)**

Figure 5.19. Run 1020. Waveform from channel 0 fitted by two identical templates but different offset (a). Also the zoomed case is shown (b). Fitting procedures are equal and so fitted waveforms coincide.

Waveform 0	Measure (Fit 1)	Errors (Fit 1)	Initial (Fit 1)	Measure (Fit 2)	Errors (Fit 2)	Initial (Fit 2)
σ	1.626	0.63224 (38.88%)	2	1.631	0.62983 (38.59%)	2
$fslow$	0.978	0.01219 (1.25%)	0.94	0.978	0.01217 (1.24%)	0.94
τ	104.924	7.96854 (7.59%)	125	104.927	7.96628 (7.59%)	125
$\mathbf{x}_0$	1238.657	0.79279 (0.06%)	1240	1238.658	0.78829 (0.06%)	1250

Table 5.4. Table of parameter extracted by different fits of figure 5.19. Parameters are in samples.

By observing the fit performed with the two templates on the second waveform (fig. 5.20), it is clearly seen that for t_1 the function learns the true peak, while in the case with t_2 the Gaussian term fit to the fluctuation of the noise. The parameters returned by the two fits are now very different (tab. 5.5).

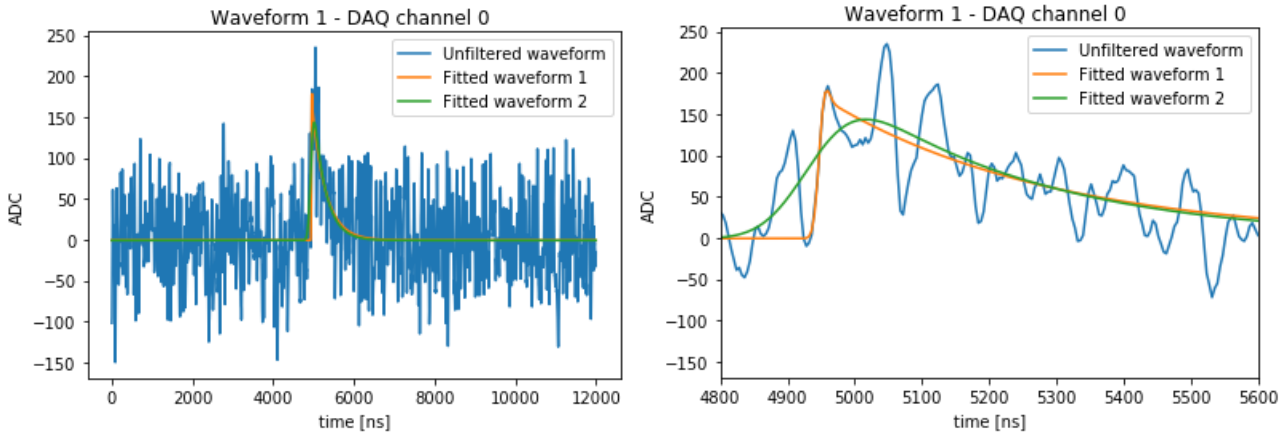

(a) (b)

Figure 5.20. Run 1020. Waveform from channel 0 fitted by two identical templates but different offset (a). Also the zoomed case is shown (b). In this case fitting procedures are different and so fitted waveforms don't coincide.

Waveform 1	Measure (Fit 1)	Errors (Fit 1)	Initial (Fit 1)	Measure (Fit 2)	Errors (Fit 2)	Initial (Fit 2)
σ	1.827	1.02834 (56.26%)	2	13.752	2063.976 (15007.76%)	2
$fslow$	0.979	0.02431 (2.48%)	0.94	0.999	19109.045 (1911203.18%)	0.94
τ	83.960	7.74317 (9.22%)	125	72.853	8.76458 (12.03%)	125
$\mathbf{x}_0$	1237.881	1.50362298 (0.12%)	1240	1233.725	1690204.47 (137000.07%)	1250

Table 5.5. Table of parameter extracted by different fits of figure 5.19. Parameters are in samples.

To understand the importance of this difference between the fit as the initial offset changes, the response of the filter to the different parameters that derive from the two measurements is studied: the parameters extracted from the fits to the first waveform, since practically identical, give rise to identical filtered waveforms, as seen in figures (5.21); the parameters extracted from the fits to the second waveform generate, because of their enormous difference, filtered waveforms that do not coincide with each other (fig 5.22).

Following what has been seen so far, it is confirmed that the fit procedure in general is not very stable if applied to waveforms with low prominence events, due to the non-negligible fluctuations in noise. However, one wonders if this procedure so sensitive at the level of the single waveform entails instability also to the shifting procedure and to the final fit of the average waveform. We have seen that the individual waveforms are shifted to the same point by taking them from a point x_0 measured with the first fit: is this x_0 really the maximum point? If not, a *smearing* is introduced and after shifting the global and local maximum points are in the same position. The average waveform will therefore be smeared and the final fit will be biased in turn. This can be observed by comparing the fit results with the same templates performed on two average waveforms obtained from the initial fits with t_1 and t_2 (fig. 5.23): the results are very different from each other (tab. 5.6). The initial difference then seems to compromise the whole procedure until the end.

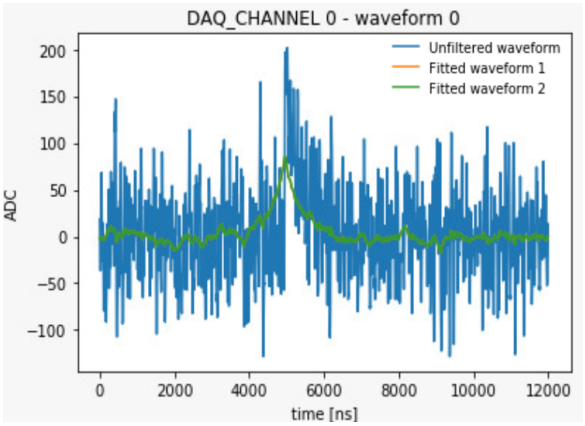

Figure 5.21. Run 1020. Waveform from channel 0 filtered with two almost identical template parameters derived from two different fits. Filtered waveforms coincide.

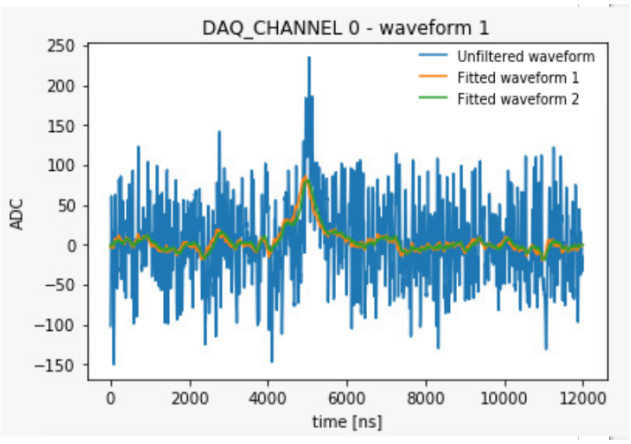

Figure 5.22. Run 1020. Waveform from channel 0 filtered with two very different template parameters derived from two different fits. Filtered waveforms do not coincide.

Average Waveform	Measure (Fit 1)	Measure (Fit 1)	Initial (Fit 1)	Measure (Fit 2)	Measure (Fit 1)	Initial (Fit 2)
σ	1.756	0.40730 (23.19%)	2	9.131	0.87439 (9.58%)	2
$fslow$	0.986	0.00785 (0.80%)	0.94	0.919	0.01819 (1.98%)	0.94
τ	106.077	2.95595 (2.79%)	125	104.138	3.73036 (3.58%)	125
$\mathbf{x}_0$	1200.672	0.65209 (0.05%)	1240	1201.514	1.35912 (0.11%)	1240

Table 5.6. Table of fit results for the two waveforms in figure 5.23. Parameters (samples) are very different from each other.

In order to be able to confirm the instability of the fitting even at the level of the average waveform, there is still one last check to be done: filter the same average waveform with the two sets of parameters obtained from the last measurement. Figure 5.24 shows the two filters and no substantial difference between them, allowing to conclude that the instability of the fitting at the single waveform level for events with low prominence does not compromise the filtering of the average waveform obtained following the shifting.

The problem just addressed concerned events with a single photoelectron. It is

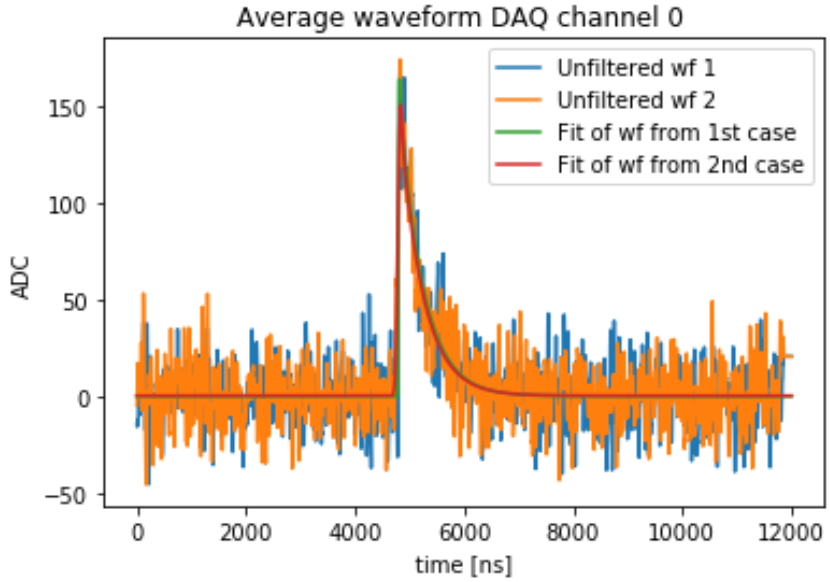

Figure 5.23. Channel 0, run 1020. Comparison between average waveforms and fits obtained either starting from $t_1 = 4.96$ μs or $t_2 = 4.98$ μs as initial fit parameters for the offset.

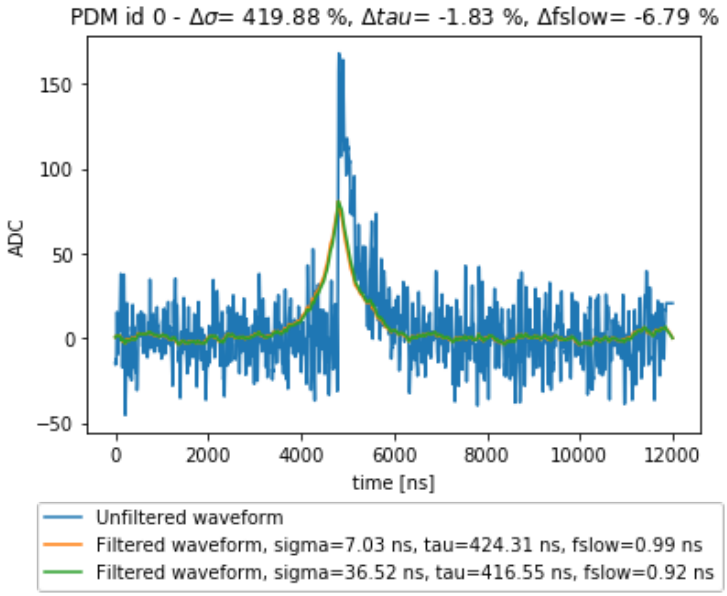

Figure 5.24. Channel 0, run 1020. Comparison between filters applied on the average waveform with very different initializing parameters: they almost coincide a this level.

fair to ask if the same also happens for events with a greater number of photoelectrons. The procedure for peaks with high prominence is therefore repeated. Two waveforms with prominence in the range 300 - 1000 ($>$ 3 pe) were selected for channel 0 of run 1020, and the first fit was performed with two very different initial offset values: $t_3 = 4.8$ μs and $t_4 = 5.2$ μs. The fits were identical for both waveforms

(fig. 5.25): the Gaussian part of the function easily represents the physical signal and it does not adapt to noise fluctuations, now very small compared to the peak. However, what happens in this particular case, as seen during the simultaneous fit of single waveforms with high prominence, is the occurrence of pileup that lead to a deterioration in the quality of the fit (fig. 5.25.d). What that second peak represents is still object of study.

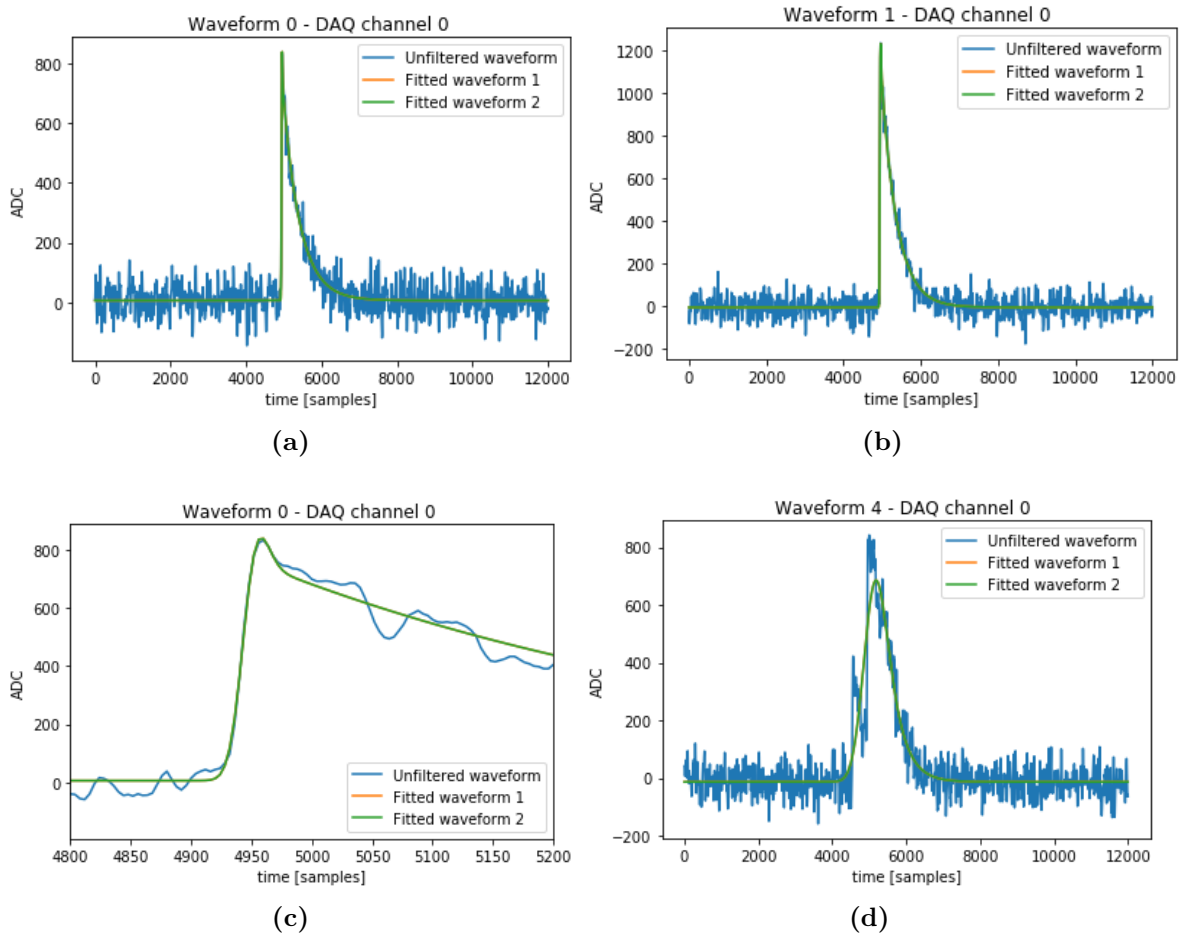

Figure 5.25. Run 1020. Two waveforms from channel 0 fitted by two identical templates but different offset. Fit is the same for both waveforms. A zoomed waveform is also shown (c): now the fit follows always the signal peak. (d) is a pathogenic case of waveform from channel 0 of run 1020: there is a second lower peak and the fit is not good.

The two methods outlined so far have been taken as examples not only because they represent two different types of approach, but also because they helped identify the limits of one of the standard procedures used in the characterisation of the filter template used in SiPM detectors.
However, it is necessary to briefly describe the other three fit techniques in order to have a complete picture of the situation and to be able to make a comparison among different methods. Again, only one channel of a single run is considered, but

each procedure is applied to all PDMs for all laser runs.

Simultaneous fit for low threshold of prominence

10 waveforms with $\sigma = 7.5$ ns, $\tau = 565$ ns and $fslow = 0.94$ are selected, having a single peak with prominence in the range 50 - 100. The trigger time is given by laser (5.008 μs). Simultaneous fit of the waveforms is performed, using same parameters of the filter: the ch 0 of the laser 1020 run is shown in the figure 5.26 and the returned parameters in the table 5.7. The case shown is a good example of a fit, but as mentioned above the large amount of noise fluctuations affecting the waveform can compromise the measurement.

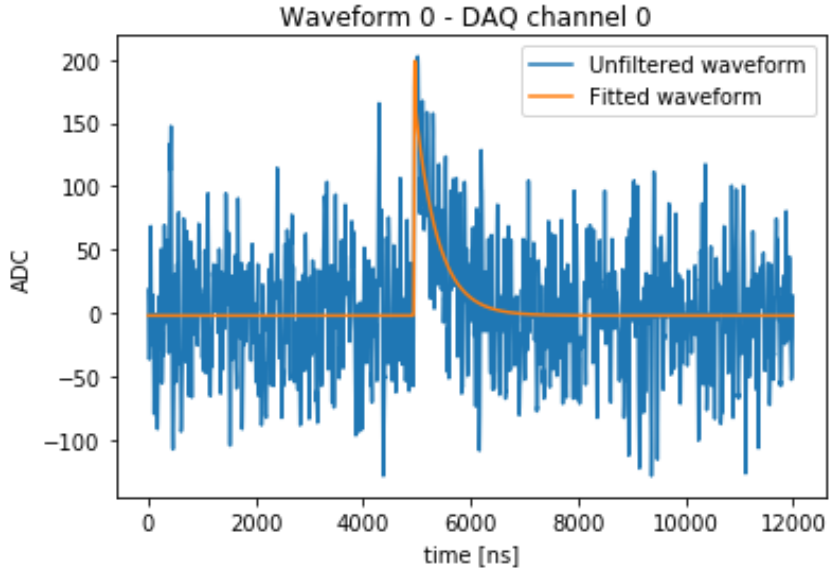

Figure 5.26. Waveform and superimposed fit for the DAQ channel 0 of run 1020, with low prominence method.

Fit parameters	Measure	Errors	Initial
σ	1.63	0.629 (38.58%)	2
$fslow$	0.97	0.012 (1.24%)	0.94
τ	104.92	7.966 (7.59%)	125
$\mathbf{x}_0$	1238.65	0.788 (0.06%)	1240

Table 5.7. Table of parameter extracted by fits of figure 5.26.

Fit of average of individual waveforms

500 waveforms are selected, with $\sigma = 7.5$ ns, $\tau = 565$ ns and $fslow = 0.94$. The second request is having only one peak with a prominence in the range 50 - 100. The trigger time is given by laser (5.008 μs). Waveforms are averaged, the the fit is performed using parameters above (fig. 5.27). The average of waveforms is cosnidered to decrease the presence of fluctuations, while peaks with low pominence are chosen so as not to have signs of pile up. This method is not very reliable since different time positions of the peaks cause a smearing in the average waveform.

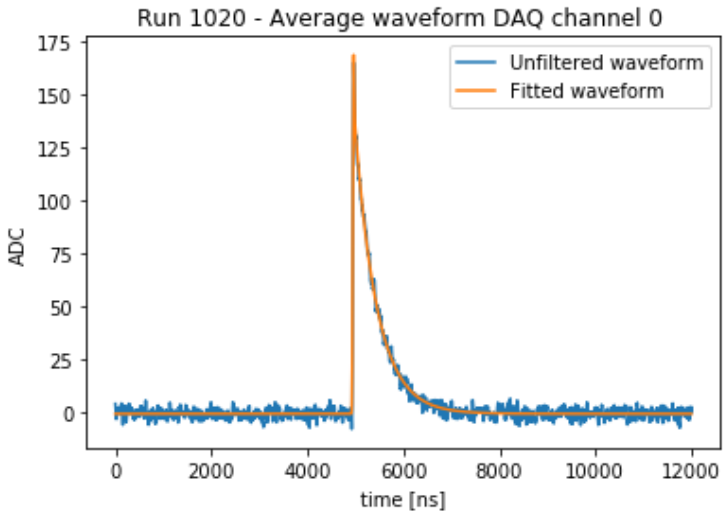

Figure 5.27. Waveform and superimposed fit for the DAQ channel 0 of run 1020, with the simple average waveform.

Fit parameters	Measure	Errors	Initial
σ	2.76	0.051 (1.82%)	2
$fslow$	0.96	8.872e-04 (0.09%)	0.94
τ	114.58	0.491 (0.43%)	125
$\mathbf{x}_0$	1238.66	0.06472830 (0.01%)	1240

Table 5.8. Table of parameter extracted by fits of figure 5.27.

Fit of average of individual waveforms shifted by a point from the cumulative function

500 waveforms are selected, with $\sigma = 7.5$ ns, $\tau = 565$ ns and $fslow = 0.94$. The second slection is single hit waveforms with a prominence in the range 50 - 100. For each single waveform the cumulative function is calculated. When the cumulative exceed a threshold of 20% of the total height of the waveform the corresponding time position t_0 is saved (5.28). Each waveform is then shifted by an amount of t_0 - t, where t = 4.8 μs is an arbitrary time value. The single waveforms shifted are fitted with the same parameter above (fig. 5.29).
This fit procedure is not very precise since the criterion with which t_0 is extracted has proved to be not very precise in turn, introducing a smearing in the average waveform.

Fit parameters	Measure	Errors	Initial
σ	9.32	11.521 (123.54%)	2
$fslow$	0.99	6.914 (692.15%)	0.94
τ	109.35	0.688 (0.63%)	125
$\mathbf{x}_0$	1146.01	835.323 (72.89%)	1240

Table 5.9. Table of parameter extracted by fits of figure 5.29.

In summary, the parameters of the SiPM response template were measured through five different procedures. Based on the complete study carried out and the

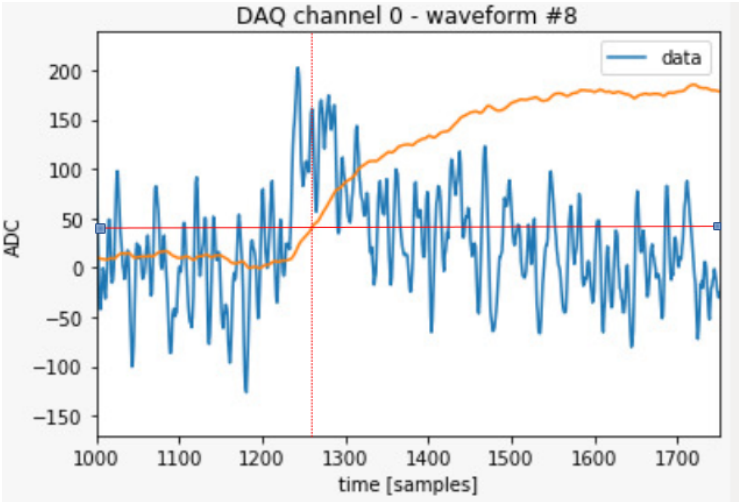

Figure 5.28. Raw waveform and superimposed cumulative for the DAQ channel 0 of run 1020. The red continuous horizontal line represents the height threshold for the cumulative and the red dotted vertical line indicates the position where the cumulative exceeds that threshold.

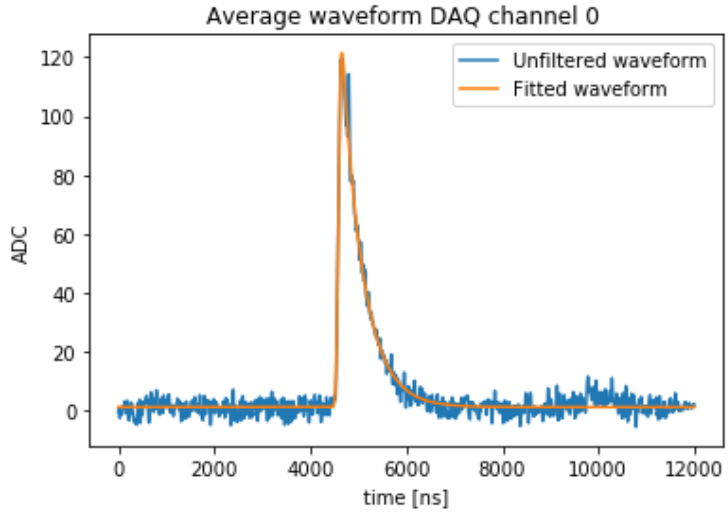

Figure 5.29. Waveform and superimposed fit for the DAQ channel 0 of run 1020, with cumulative method.

results obtained, it is not possible to affirm that one of these techniques is the most efficient in absolute, but comparing the stability plots among them it is observed that the case of simultaneous fit of a single waveform with high prominence brings less fluctuations in the measured parameters and therefore it was chosen as the standard procedure.

5.5 Signal-to-Noise Ratio

The work done so far has consisted in devoloping a robust techinque for determination of the parameters of the SiPM response template. To this end, five sets of parameters were measured through five different procedures. The results obtained so far are now very useful for checking if the filter is really sensitive to different initial configurations and if therefore it is possible to find a set of parameters that maximize its performance. The filter is an algorithm that aims to clean waveform from the electronic noise. To determine the quality of this operation, we use a very important parameter in electronics: the *signal-to-noise ratio* (SNR), a measure that compares the desired signal level with respect to the background noise level.
The SNR is defined as:

$$SNR = \frac{\mu}{\sigma}, \tag{5.3}$$

where μ is the average of the expected signal and σ standard deviation of the noise (RMS). In the specific case of SiPM μ can be considered as the average prominence of events generated by 1 pe, i.e. the *prominence gain* of the SiPM. An high estimate of the SNR therefore ensures high filter performance.
We proceed with the measurement of the SNR of each PDM by initializing the filter with the five different sets of parameters available.
The measurement took place in two stages:

- Gain measurement
- Standard deviation measurement of the filtered baseline

Gain measurement (for a single PDM)

Run 1020 is considered. Filter is set to a certain parameter configuration to perform the first waveform selection. About 5000 single hit events consistent with the laser trigger time (5,008 μs) are selected. The prominences reconstructed by the peak finder are histogrammed (fig. 5.30.a): each peak is centered in the average prominence associated with a certain number of photoelectrons, so that the first peak corresponds to 1 pe, the second to 2 pe, and so on. The first two peaks are fitted with Gaussians and the average values associated with p_1 and p_2 with each peak is extracted from the fit (fig. 5.30.b). The gain is then calculated as the difference of these two values: $GAIN = p_2 - p_1$.

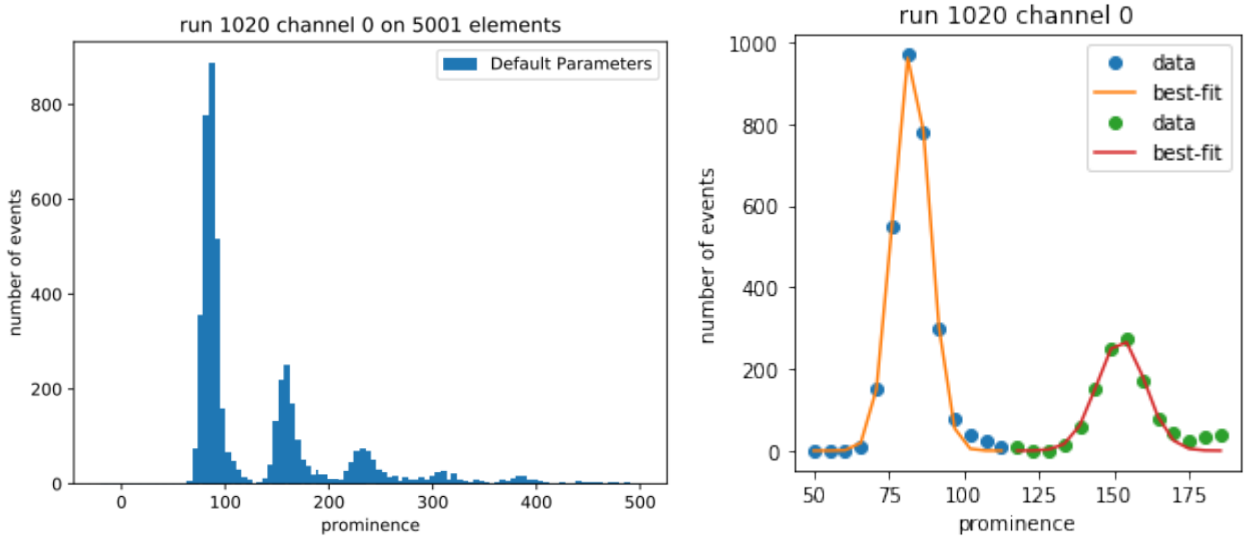

(a) (b)

Figure 5.30. Prominence distribution for channel 0 of run 1020 (a) and gaussian fit of firsts two peaks of the plot for gain calculation (b). Fit results: $p_1 = 81.4 \pm 5.2$, $p_2 = 151.6 \pm 7.8$.

Standard deviation measurement of the filtered baseline (for a single PDM)

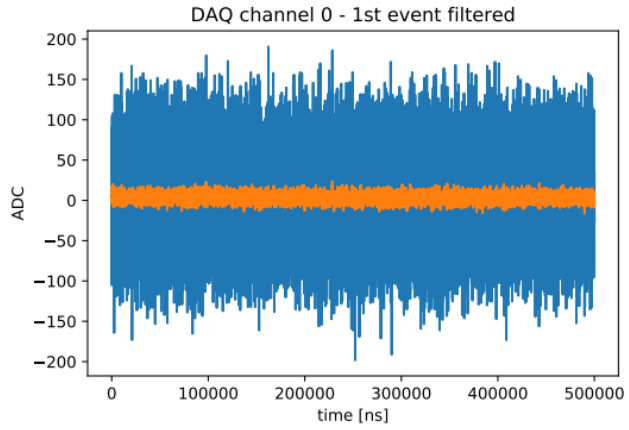

Run	886
Nevents (k)	
Edrift (V/cm)	200
Eextraction (kV/cm)	2.8
SiPM tension (V)	50
gas pocket	ON
laser intensity	
trigger	external (50 Hz)
trigtime (μs)	100
post-trigger (μs)	400
Time gate (μs)	500

(a) (b)

Figure 5.31. Baseline event for channel 0 of run 1020 with superimposed the filtered waveform (a) and parameters list of baseline run (b).

About 5000 events are selected from the baseline run 886, characterized by a bias voltage of 50 V that is sufficiently below the breakdown threshold. For this run the PDM 13 and 20 are off. The waveform is filtered (fig. 5.32.a) - the filter parameters

are indifferent, there is no peak to be reconstructed - and the standard deviation is calculated ($\sigma = \sqrt{\frac{\sum_{i=1}^{N}(x_i-\mu)^2}{N-1}}$, where x_i is the value of the waveforms in the i-th sample, N is the number of elements of the waveform - in this case 125000 - and μ is the average value of the waveforms). The approximately 5000 RMS calculated in this way are histogrammed (fig. 5.32.a) and the distribution is fitted with a Gaussian (fig. 5.32.b) so as to extract the average RMS value, to be used as denominator in equation (1.2).

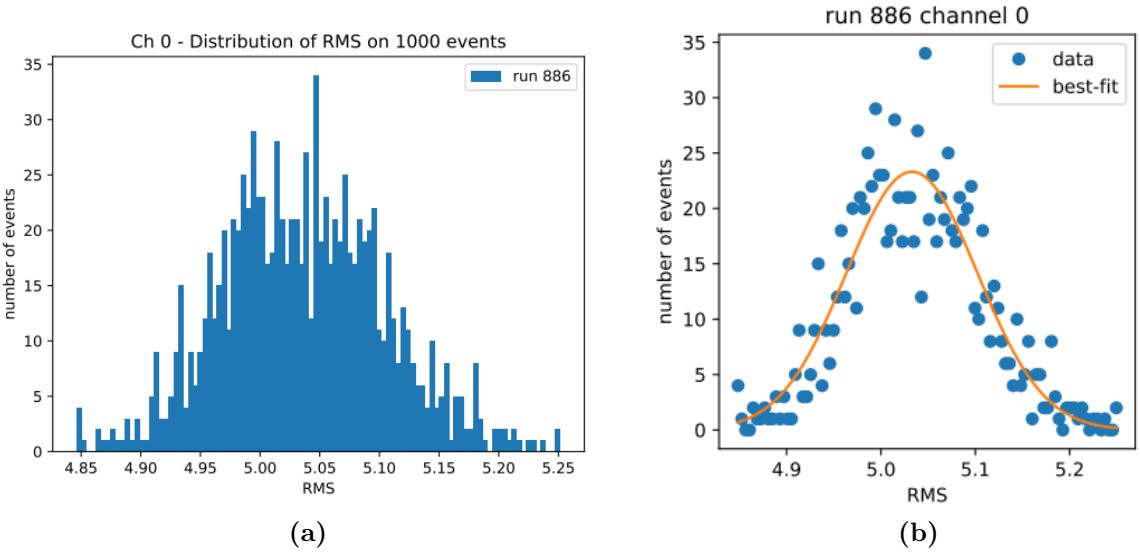

(a) (b)

Figure 5.32. RMS distribution for channel 0 of run 1020 (a) and gaussian fit of the plot to extract the mean value of RMS (b). Fit parameters: $center = 5.03 \pm 0.076$.

Gain and RMS measurements are then performed for all PDMs, being able to calculate the SNR. The plots below show respectively the SNR calculated for all PDMs by filtering the waveforms with $\sigma = 7.5$ ns, $\tau = 565$ ns and $fslow = 0.94$ (fig. 5.33) and using the five sets of previously measured template parameters (fig. 5.34).

From these plots it is observed that the SNR value does not vary significantly as a function of the filter parameters, and these values do not even differ from the approximate case. From this we come to the important conclusion that the filter is not sensitive to the different parameters which it is configured with and consequently it cannot be optimized through a particular template.
On the basis of last results it is expected that by averaging σ, τ and $fslow$ measured with a particular fit method the SNR for each channel will remain basically unaltered.

Figure 5.35 shows the SNR values for run 1020, for which σ, τ and $fslow$ are averaged for all PDMs, for each of the templates: the deduction that the SNR values have remained more or less unchanged is now confirmed, and then a lower dispersion of this quantity among the five cases is also observed. This leads to the important result for which, for the purpose of reconstructing the events seen by the PDMs of Proto-0, it does not matter which particular fit method is used to measure the parameters of the SiPM response: by averaging them the filter is applied to

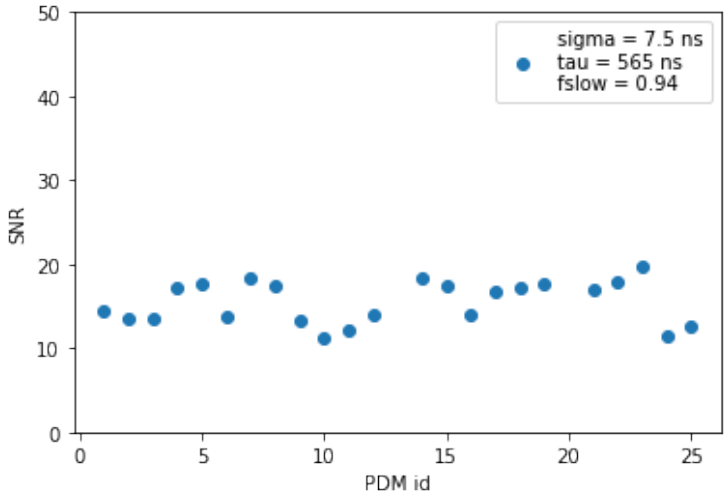

Figure 5.33. SNR calculated for all PDMs with approximative parameters.

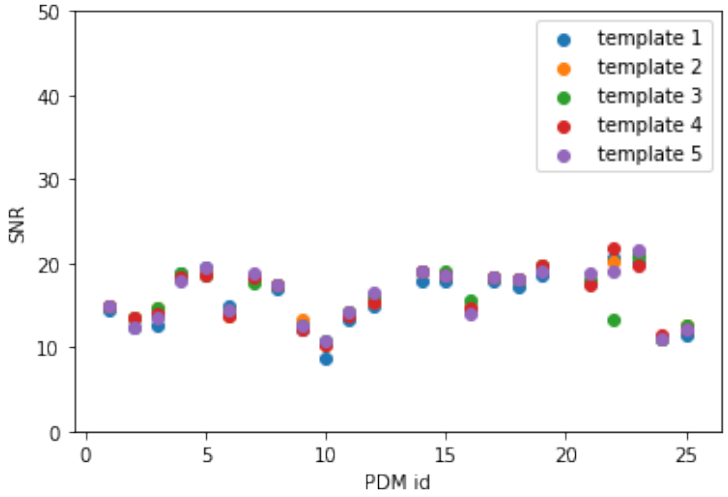

Figure 5.34. SNR calculated for all PDMs using five set of fit results.

waveform in the same way. So, also with a view to real-time data analysis compared to acquisition, a good strategy to optimize time is measuring the parameters with the fastest fit method and then average them for each PDM. This will be very important for DarkSide 20-k where PDMs will be almost 10000.

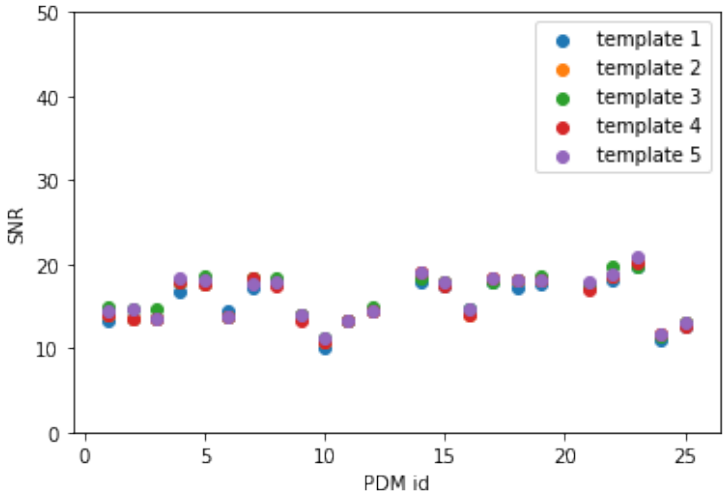

Figure 5.35. SNR calculated for all PDMs by averaging parameters for each of five set of fit results. There is not a substantial difference with fig. 5.34, but lower dispersion of SNR among methods is now observed.

5.6 Gain measurement

Up to this point an in-depth study has been carried out concerning the measurement of the parameters of the SiPM response template, obtaining as a result that the SNR does not vary if the filter parameters are obtained with the different techniques descibed in the previous section.
Now we want to evaluate the influence that a precise filter choice has on the measurement of the electric charge of waveforms and on the event reconstruction based on prominence.

Gain measurement with charge integration

The electric charge is linked to the current by the relationship:

$$Q = \int_{t_1}^{t_2} i(t)dt, \tag{5.4}$$

with t_1 and t_2 fixed instants.

To measure the charge associated with an electronic signal it is therefore necessary to define a time window and perform the integral of the waveform raw in it. We take into consideration the filter with known approximate σ, τ and $fslow$ and the one with the fit parameters from the high prominence threshold method (see section 4). Laser run 963 is considered as an example. 500 single hit events with both filters are selected for each channel. To measure the electric charge the range 4.9 - 7.9 μs - around the trigger time of 5.008 μs given by the laser - is chosen as the integration window, and then the integral of each waveform is calculated. An histogram is filled with the charge values obtained: the distribution is characterized by peaks in correspondence with the charge released by a precise number of photoelectrons in the PDM and for this reason it represents the *charge integral histogram* of that PDM on the basis of the electric charge.

Plots in figure 5.36 represent the charge integral histograms obtained from an approximate filter for channel 0 of laser run 963. The filter does not affect the measurement of the electric charge in any way since this quantity is linked to the underlying area of the raw waveform and therefore does not depend on the particular filter.

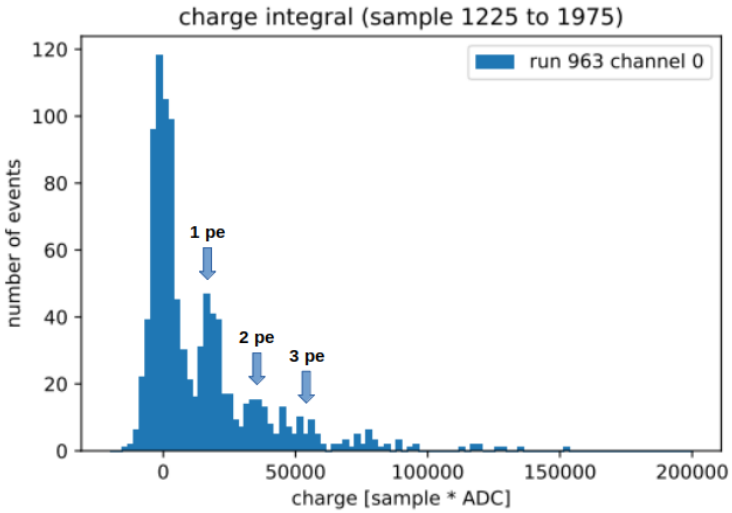

Figure 5.36. Charge integral histogram for channel 0 of laser run 963, derived from approximate parameters.

Gain measurement with hit-based reconstruction

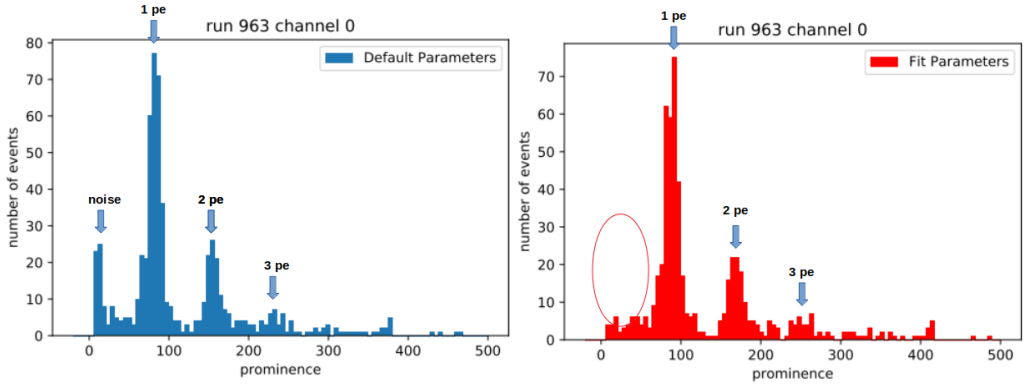

(a) **(b)**

Figure 5.37. Channel 0 of run 963. Prominence distribution derived from approximate template parameters (a) and measured template parameters (b). In the first case a very low prominence peak is occurred, due to noise, and then cut by the improved filter.

Run 963 is also considered for the prominence histogram. For each PDM, 500 single hit events with both filters are selected. The peak-finding algorithm - set with the parameters $height = 40$, $prominence = 10$, $width = 1sample$,

$distance = 1sample$ - identifies the hits and measures their prominence. The collected values are used in both cases to fill the gain plot.

The comparison between the two plots shows an important difference (fig. 5.37): the peak for low values of prominence present in the case of rough filter disappears almost completely when the filter is more precise. There is reason to think that that peak is due to noise events mistaken for signal in the first case and correctly identified in the second one. It can therefore be said that the choice of the filter has an impact on the peak finder algorithm and a suitable choice of the initial parameters can effectively optimize the process of reconstruction of the hits.
An in-depth study of peak finder efficiency is described in chapter 6, through the use of MC simulations.

We now proceed with the calculation of the gain starting from the charge and prominence distributions.
Consider channel 0 of run 1020. All single peak in the time window between 1240 and 1250 samples are selected. We use the prominence values obtained by the peak finder to fill the distribution, as seen in figure 5.38. We perform a Gaussian fit independently for each peak of the histogram (fig. 5.39), extracting the center and the σ (tab. 5.10). The fit is not very precise but only the calculation logic is discussed here. The method will be improved later.

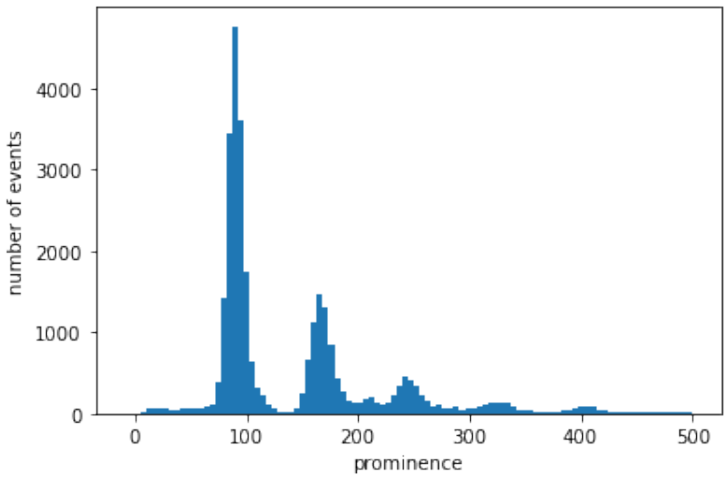

Figure 5.38. Prominence distribution for channel 0 of run 1020.

Peak Number	Center	σ
1	89.45	5.01
2	168.5	7.65
3	245.00	7.65

Table 5.10. Table of fit parameters extract by fit procedure of fig. 5.39.

We associate the each prominence peak position with its associated number of pe obtaining the plot prominence as function of number of photoelectrons in figure 5.40. The fit is done with the function $p = n_{pe} \cdot g + n_0$, where n_{pe} is the number of photoelectrons, p is the prominence, p_0 the intercept and g is the gain.

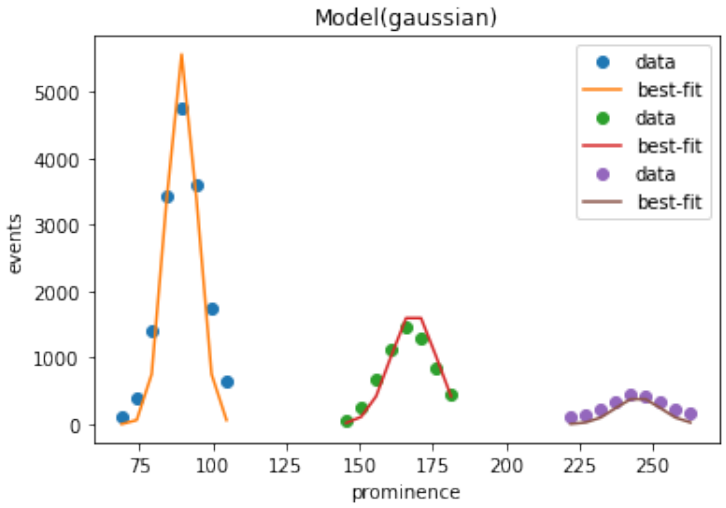

Figure 5.39. Gaussian independent fit of peaks of fig. 5.38.

So, from this linear fit is possible to extract the gain with the relative error for a particular channel, channel 0 in this case (tab. 5.11).

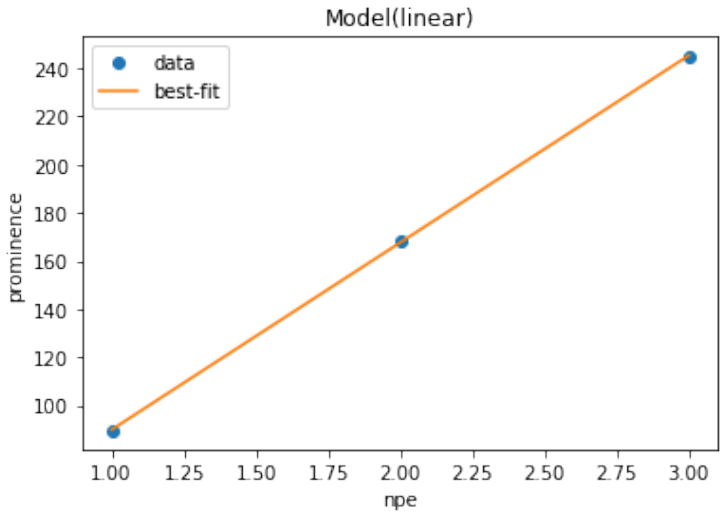

Figure 5.40. Linear fit of the dependence plot between prominence and number of pe.

Name	Value	Standard Error	Relative Error
Slope	77.774	0.7361	(0.95%)
Intercept	12.100	1.5902	(13.14%)

Table 5.11. Table of fit parameters extract by linear fit shown of fig. 5.40.

Now we want to compare this result with the one obtained in the same way for the charge integral histogram. The charge integrated in the 2 μs interval is histogrammed. The Gaussian fit is performed and the charge peaks associated with a certain number of pe are identified (fig. 5.41). Fit parameters *center* and σ of

each peak are extracted (tab. 5.12) .

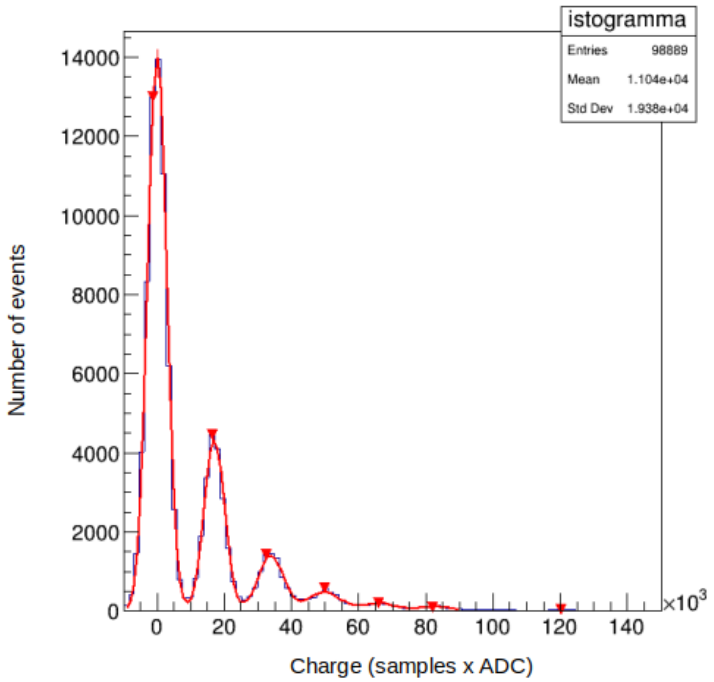

Figure 5.41. Charge distribution of channel 0 for laser run 1020. The superimposed red line is the Gaussian independent fit of peaks.

Peak Number	Center	σ
1	3.315e1	2.86e3
2	1.702e4	3.18e3
3	3.393e4	4.578e3
4	4.994e4	4.806e3
5	6.508e4	7.716e3
6	8.181e4	6.867e3

Table 5.12. Table of fit parameters extract by fit procedure of fig. 5.41.

The plot charge vs *npe* is done and it is linearly fitted by the function $c = npe \cdot g + c_0$, where n_{pe} is the number of photoelectrons, c is the prominence, c_0 the intercept and g is the gain. So, from the the gain with the relative error for a particular channel are extracted (tab. 5.13).

Name	Value	Standard Error	Relative Error
Slope	16881.41	15.613	(0.092%)
Intercept	45.95	0.937	(2.04%)

Table 5.13. Table of fit parameters extract by linear fit shown of fig. 5.42.

It is observed that the measure of gain is different, concluding that the two methods must not necessarily be equivalent.

The number of observed photoelectrons follows the Poisson distribution $P_\lambda(n) = \frac{\lambda^n}{n!}e^{-\lambda}$, where λ is now mean number of observed photoelectrons that is proportional

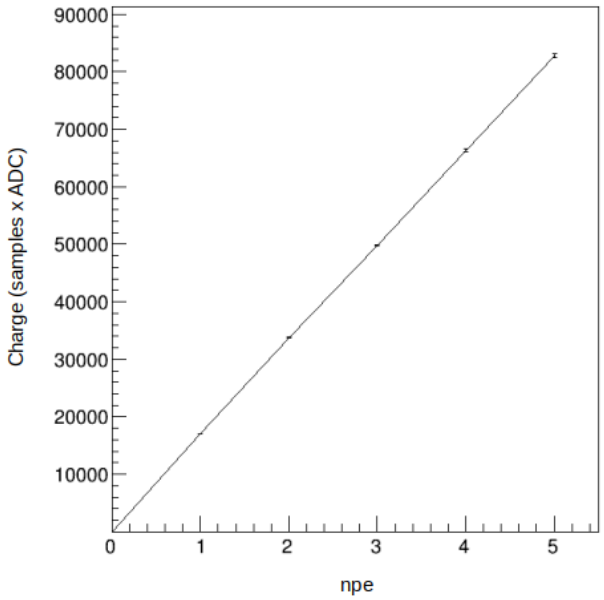

Figure 5.42. Linear fit of the dependence plot between charge and number of pe and charge.

to the mean number of emitted photons and n is the number of observed photoelectrons. As last step we want to obtain the average number of photoelectrons observed by a given channel, that is the λ of the distribution above. This parameter is called **occupancy** of the PDM. It is possible to calculate the occupancy starting from the charge peak relative to 0 pe: in this case the distribution of poisson becomes $P_\lambda(0) = e^{-\lambda}$ and we calculate λ through the inverse formula knowing the probability of having npe $= 0$. $P_\lambda(0)$ is given by the ratio of the the first peak number of events N_0 and the total number of events N, so we get:

$$occupancy = \log(-\frac{N_0}{N}). \tag{5.5}$$

For channel 0 this number is equal to 0.64. The 2D map of occupancy is shown in figure 5.43, relating to the Proto-0 MotherBoard: it is consistent with the positioning of the laser fiber with respect to the PDMs and it will be a fundamental diagnostic tool for the calibration of the DS-20k PDMs.

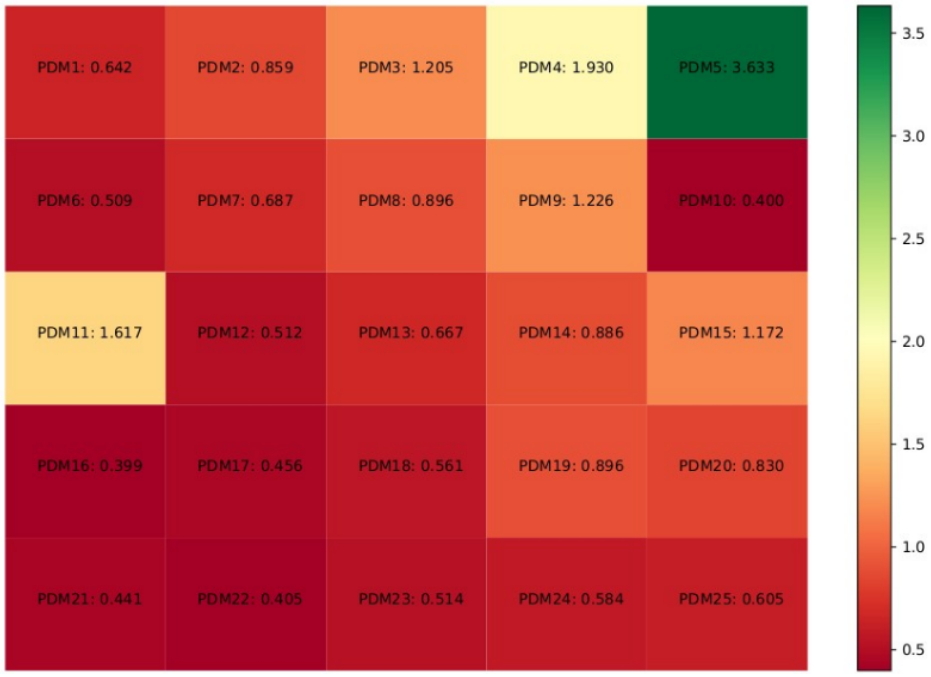

Figure 5.43. Occupancy 2D map of PDM matrix of Proto-0.

5.7 Dark Count Rate

The main source of noise in a SiPM is dark events, sporadic pulses of current produced in the absence of light due to carriers generated by thermal agitation. The number of dark events per unit of time is defined as *dark count rate* (DCR). In addition to increasing with temperature, the DCR increases with increasing bias voltage [32].
It is interesting to study the DCR in Proto-0 SiPMs, varying the supply voltage and checking the dependence of this parameter on the overvoltage. Runs 1122, 1125 and 1127 are considered for this purpose: these runs are taken using ^{241}Am source and for them the voltage of the PDM of the motherboard has been set to 63, 65 and 67 V respectively (fig. 5.46).

Run	1122	1125	1127
Nevents (k)	5	5	5
Edrift (V/cm)	0	0	0
Eextraction (kV/cm)	0	0	0
SiPM tension (V)	63	65	67
gas pocket	OFF	OFF	OFF
laser intensity			
trigger	external (50 Hz)	external (50 Hz)	external (50 Hz)
trigtime (µs)	600	600	600
post-trigger (µs)	400	400	400
Time gate (µs)	1000	1000	1000

Figure 5.44. Table with characteristics of americium runs 1122, 1125 and 1127 used for the study of dark count rate.

The SiPMs therefore have the possibility both of emitting electrons by thermal

agitation and of seeing the scintillation light generated in LAr. However the SiPM dark count has a much higher rate than the source and for this reason we only see that. A different DCR is therefore expected for the three runs, minimum for run 1122 and maximum for 1127.
A parameter that well reflects the dark count rate is the SNR. The higher the voltage, the higher the dark count rate but also the gain of the photoelectrons generated, and lastly the SNR. So for the runs in question we expect a minimum SNR for run 1122 and a maximum for run 1127.
In order to calculate the SNR it is necessary to filter the waveforms appropriately. To do it, it is decided to measure the template parameters with the high threshold prominence fit method, then making them the average of all PDMs, a convenient operation as seen previously (fig. 5.35). The measurement results are then used in the filter for the three runs (fig. 5.45). The calculation of the SNR is achieved as it was learned in the previous paragraph. The plot showing the trend of the SNR for the three runs is shown in figure 5.46, which shows what is expected: on average, the SNR increases with increasing supply voltage. The values are measured: $SNR_{1122} = 13.102$, $SNR_{1125} = 14.881$ and $SNR_{1127} = 17.209$.
What can be observed from the measurement of the SNR confirms the dependence of the DCR on the supply voltage of the SiPM, so this parameter increases with the increasing of the overvoltage.

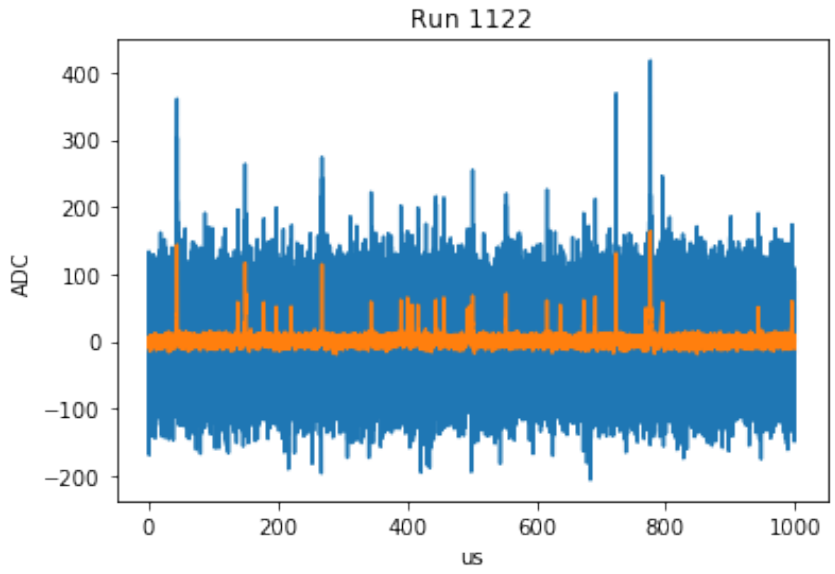

Figure 5.45. Dark counts events for a channel of run 1122, in the time window of 1 ms.

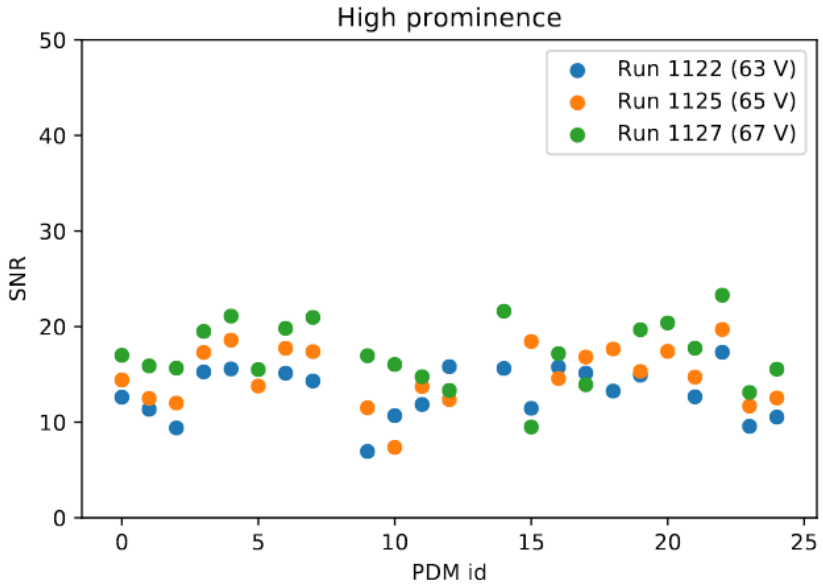

Figure 5.46. SNR vs PDM id for americium runs with different bias voltage. SNR increases with the increasing of the bias voltage.

5.8 Firts look at S_1 and S_2 signal with ^{241}Am source

The last point discussed in this chapter is the observation of the data in which there is the occurrence of an S_1 scintillation signal followed by an S_2 pulse that could be due to drift electrons from ionization in LAr. For this purpose, run 1195 with ^{241}Am source was considered, with gas pocket and the two electric fields turned on (fig.5.47).

Run	1195
Nevents (k)	20
Edrift (V/cm)	200
Eextraction (kV/cm)	2.8
SiPM tension (V)	65
gas pocket	ON(7 mm)
laser intensity	
trigger	500
trigtime (µs)	100
post-trigger (µs)	100
Time gate (µs)	200

Figure 5.47. Table with characteristics of americium runs 1122, 1125 and 1127 used for the study of dark count rate.

The strategy is as follows:

1. the waveforms collected by the PDM are filtered with the test parameters $\sigma = 7.5$ ns, $\tau = 565$ ns and $fslow = 0.94$;

2. since 250000 samples (1 ms) are collected for each event, to speed up the process the waveforms are downsampled with a frequency 20 times lower (12.5 Ms/s) and then reconstructed; this study was done to understand if, even if

we had to do a downsampling at the triggerlevel of DarkSide-20k trigger to quickly process S_2 signals, we would still be able to study this type of signals;

3. a first peak is selected around the trigger time, in the range 92 - 104 μs, with a minimum prominence of 300 ($\sim$3 pe);

4. the second peak is looked for in a time interval following the first peak (100 - 112 μs).

The plot in figure 5.48 shows an S_1 + S_2 event for channel 0, while figure 5.49 shows the same event seen by all the PDMs of the matrix.
However, as anticipated, the nature of the second peak has not yet been established. In-depth studies on this topic refer to further studies with new future runs taken with an upgraded version of the prototype.

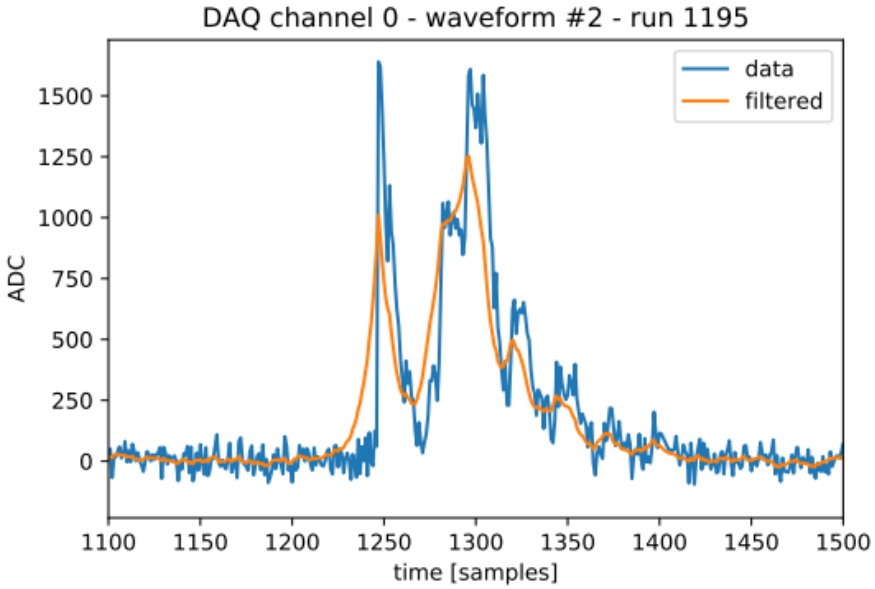

Figure 5.48. Waveform raw and filter superimposed for an event with both S_1 and S_2 for channel 0 of run 1195.

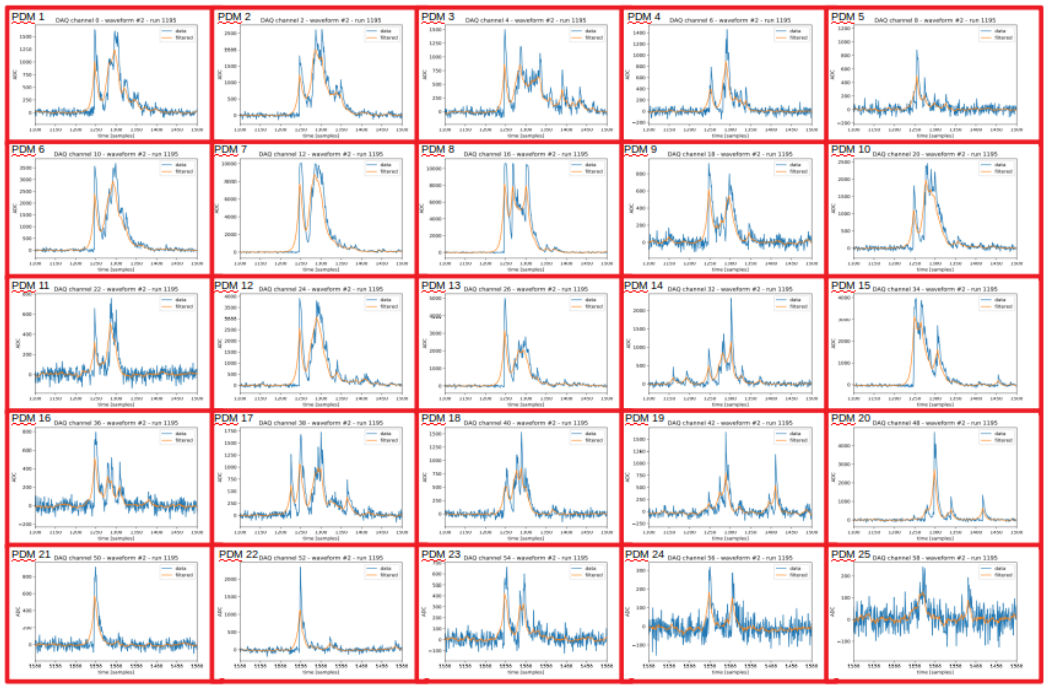

Figure 5.49. S_1 + S_2 event seen by all PDMs matrix, for run 1195.

Chapter 6

Optimisation of hit finding with Monte Carlo simulation

In this chapter we want to validate the study done so far on data through a Monte Carlo simulation. The simulation allows the generation of signals reproducing the real response of the PDM seen from the data. Events of different nature can be created, depending on the temporal distribution of the photoelectrons of the primary peak (electron recoils, nuclear recoils, laser events) and depending on the type of study to be conducted (noise and poisson distribution control to generate the photoelectrons).
The 25 channels of the MotherBoard are simulated and single hit events are reproduced with the aim of carrying out the same measurement of template parameters with the five fit methods examined in chapter 5. The results obtained are then used to reconstruct the events and calculate the SNR of each channel, measuring the noise from baseline events also generated by Monte Carlo. If the level of SNR measured in the data is reproduced, there is the confirmation that the procedure works.
Thanks to the simulation it is also possible to evaluate the efficiency of the peak finder both from the point of view of the temporal resolution of the hits, generating two single identical pulses and varying their mutual distance, and from that of reconstructing events for nuclear and electron recoils, modifying the prominence threshold with which to reconstruct them.

6.1 Simulation of the SiPM response

The simulation of a SiPM response aims to faithfully reproduce the real output signal of one of these photosensors.
First of all, the algorithm specifies how the response of a SiPM to a single photoelectron should be and what are the parameters that characterize the event to be analyzed:

1. **gaussian + exponential model**: the SiPM response to a single photoelectron can be modeled as the convolution of a Gaussian with a decreasing exponential; the parameters necessary to create this function are the σ of the Gaussian, the decay time of the exponential *tau* and the fraction of the slow

component $fsow$;

2. **gain**: peak height associated with a single pe; in the case of Proto-0 data this value is ∼150 ADC;
3. **sampling rate**: sampling rate, in MS/s; fixed a time interval determines the number of samples that fall within it; in the real case it is = 250 MS/s;
4. **gate**: time window in which the event is located;
5. **pretrigger**: interval preceding the position of the peak; this quantity specifies the position of the peak;
6. **signal-to-noise ratio**: determines the amount of noise fluctuations affecting the raw waveform; the real one is ∼5;
7. **baseline**: mean vertical position of the baseline (ADC).

To make the simulation even more realistic, it is possible to activate:

- *noise*, due to dark count (DCR), cross talk (CT) and after pulse (AP) in order to create additional peaks;
- *Poisson distribution* that regulates the number of photoelectrons of the primary peak: if the simulator is initialized with n photoelectrons, this will be the expectation value of the Poisson distribution.

Starting from the number of pe given as input, the operating principle of the simulation algorithm is described below:

1. each pe is subjected to a *charge spread*, or to it a charge is associated that is not fixed but follows a Gaussian distribution;
2. if DCR, CT and AP are on, a number of pe is added with a certain probability which depends exponentially on the distance from the first peak; this is a recursive phenomenon, so for example an AP pe can produce a CT pe, and so on;
3. a list of pe is then created starting from the input number of pe;
4. each pe of the list is smeared according to a decreasing exponential $e^{-t/\tau}$, i.e. for example the charge from 1 sample is spread to 3 successive τ samples (smearing);
5. each pe is then smeared according to a gaussian;
6. the resulting waveform is normalized to the gain, the baseline is added and then the noise is added according to a Gaussian of average 0 and $\sigma = snr/gain$;
7. each number of the waveform is converted from float to int;
8. saturation is simulated, i.e. a threshold is set to a certain number of bins inserted into the input.

Once the fundamental specifications of the signal to be created have been defined, it is necessary to specify the physics behind the signal itself. A signal may be due to the light of a laser that directly illuminates the SiPM, as has been the case for many runs acquired for the Proto-0 PDMs calibration. On the other hand, in general, particles of different nature can interact with the LAr atoms in the TPC by exciting them in a process involving the two singlet and triplet states: they lead to different time distributions of the photoelectrons in the SiPM, depending on whether it is due to electron or nuclear recoils. In light of this, the simulator is initialized with the scintillation parameters of the LAr: the singlet and triplet decay times $\tau_s = 9$ ns and $\tau_t = 1.6$ μs and the singlet probabilities for electron recoil and nuclear recoil $P_{ER} = 0.3$ and $P_{NR} = 0.7$. The number of photoelectrons to be simulated is then indicated and the type of recoil is specified in term of time distributions:

1. **Laser**: delta distribution of pe, since the light comes directly and the photoelectrons are all extracted at the same time (fig.6.1);

2. **Nuclear Recoil** : photoelectrons of the primary peak follow the decreasing exponential distribution given by the scintillation parameters of the LAr specified above; the peak decreases rapidly due to a greater presence of singlet states;

3. **Electron Recoil**: photoelectrons of the primary peak follow the time distribution of this physical event as specified above; in this case the signal decreases slowly due to a greater presence of triplet states.

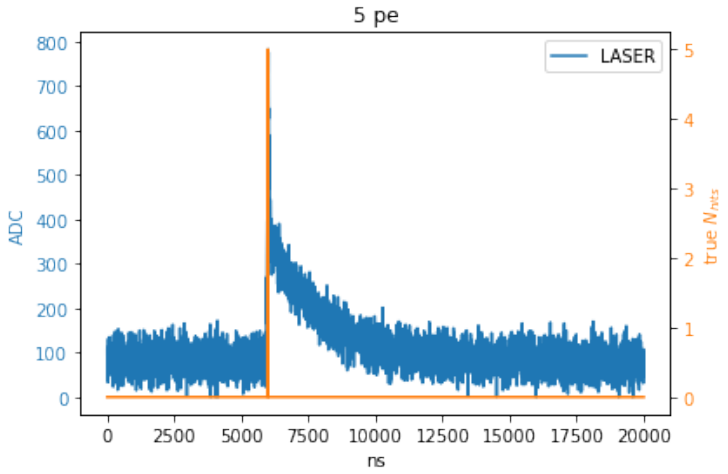

Figure 6.1. Waveform due to 5 pe simulating the laser source. The vertical axis on the right is the number of pe generated.

Now we proceed with the verification of the measurement procedures performed previously on the data and with the study of the efficiency of the hit reconstruction algorithm.

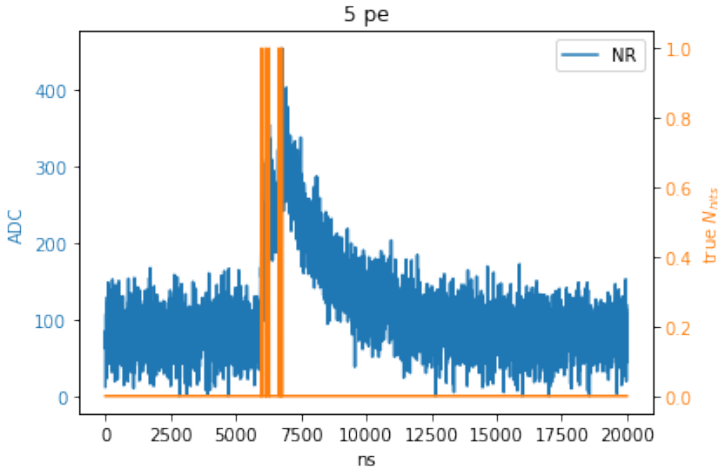

Figure 6.2. Waveform due to 5 pe simulating NR signal.

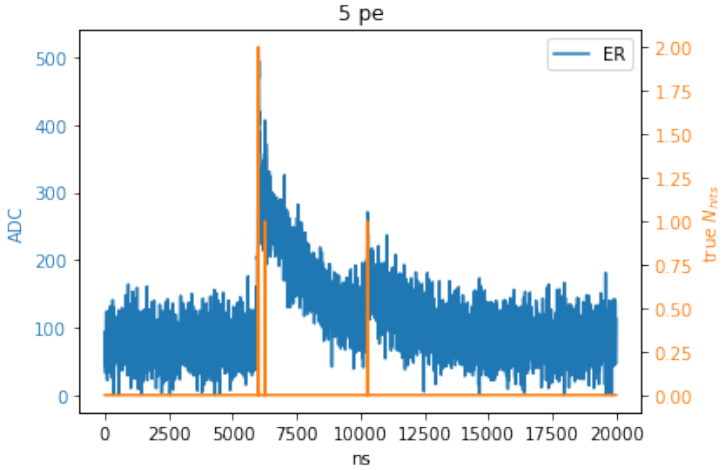

Figure 6.3. Waveform due to 5 pe simulating ER recoil signal.

6.2 Method

Now that we know the complete operation of the simulator, it is first used to validate the results obtained with regards to the study of the filter performance conducted with real data. The strategy is always the same: through the five fit methods the template parameters are measured which are then used to filter the waveforms and then finally calculate the SNR. The same results are expected to be observed with real data. For this purpose, events taken from laser runs are simulated, without crosstalk and afterpulse and for simplicity without Poisson fluctuations in the number of generated photoelectrons, in order to have all peaks more or less equal. The following parameters are initialized, kept fixed from now on: $gain = 140$, $pretrigger = 6$ μs, $snr = 5$, baseline $= 0$. The 25 channels of the motherboard are simulated: for each channel, events with σ, τ and $fslow$ taken from the template measurement of the laser run 1020 made with the high prominence threshold fit

method are reproduced (τ = 459.71 ns, σ = 8.69 ns, $fslow$ = 0.99). Now that the simulator is ready, we proceed with the fit methods applied to the data to measure the template parameters. The fit function is always initialized with τ = 565 ns, σ = 7.5 ns, $fslow$ = 0.98, $offset$ = 6 μs, $amplitude$ = 8000 and $baseline$ = 0. The following procedures have been performed on each channel:

1. simultaneous fit of 10 waveforms with 1 pe (fig. 6.4.a);
2. simultaneous fit of 10 waveforms with 5 pe (fig. 6.4.b);

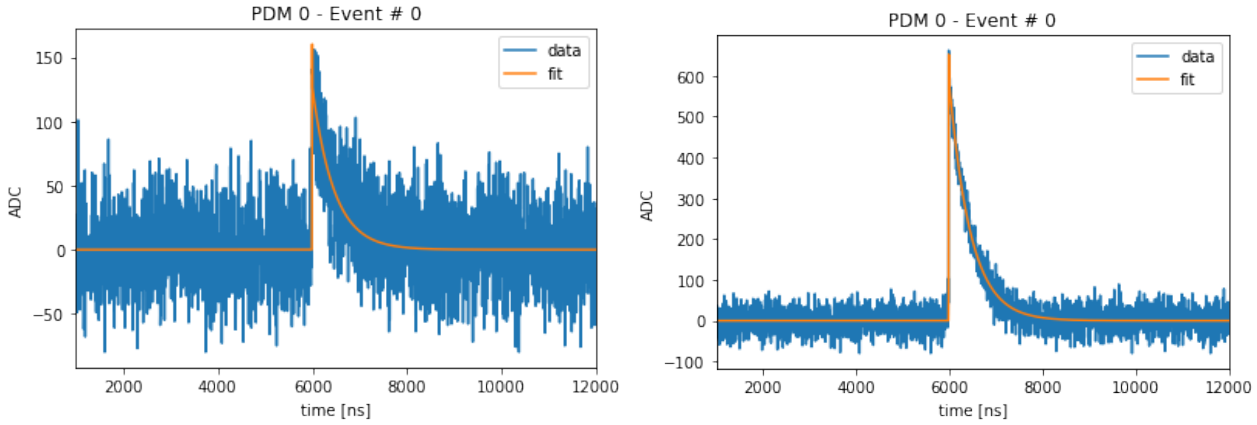

(a) (b)

Figure 6.4. Waveform and fit by method 1) (a) and 2) (b), for channel 0.

3. fit of the average of 500 individual waveforms with 1 pe (fig. 6.5.a);
4. fit of the average of 300 individual waveforms with 1 pe after having shifted them by a certain amount, taking as a reference the point where the cumulative function exceeds an arbitrary set threshold (fig. 6.5.b);
5. fit of the average of 500 individual waveforms after having shifted them by a given amount, from a position extracted through a preliminary fit of the individual waveforms (fig. 6.5.c).

Now we proceed with the calculation of the SNR. To estimate the gain, the parameters of a particular measured set are taken and averaged between the channels and the result is used as the filter input. 500 laser events are simulated for each channel, without noise, with the same simulation parameters, but this time the number of photoelectrons is distributed according to a Poissonian of average 1 pe. The peaks are filtered and their prominence is measured through the peak finder, set with $height$ = 40, $prominence$ = 10, $distance$ = 1, $width$ = 1 (fig. 6.6).

The gain plot is filled, with a Gaussian fit the average values of the first two peaks are measured and the gain is obtained from their difference (fig. 6.7). This procedure is performed for all fit methods.

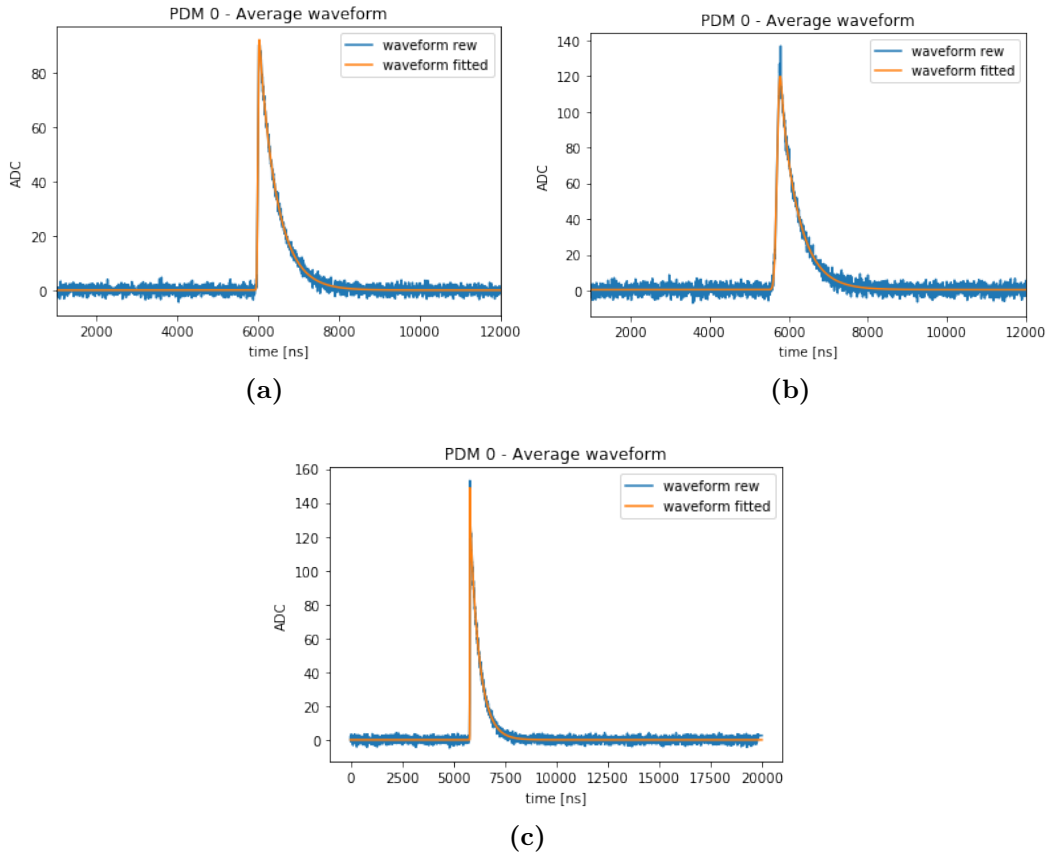

Figure 6.5. Waveform and fit by method 3) (a), 4) (b) and 5) (c), for channel 0.

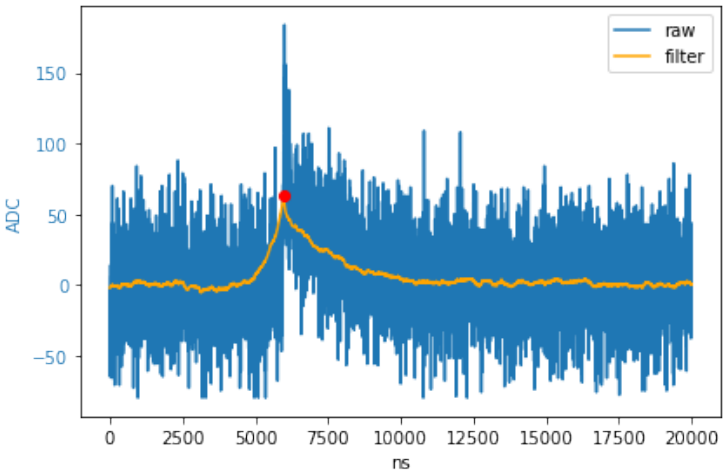

Figure 6.6. Waveform raw and filter superimposed simulated for an event of channel 0. The red point is the reconstructed hit by the peak finder.

Baseline events are simulated for the calculation of the standard deviation: in this case the poisson distribution of the generated number of photoelectrons is off

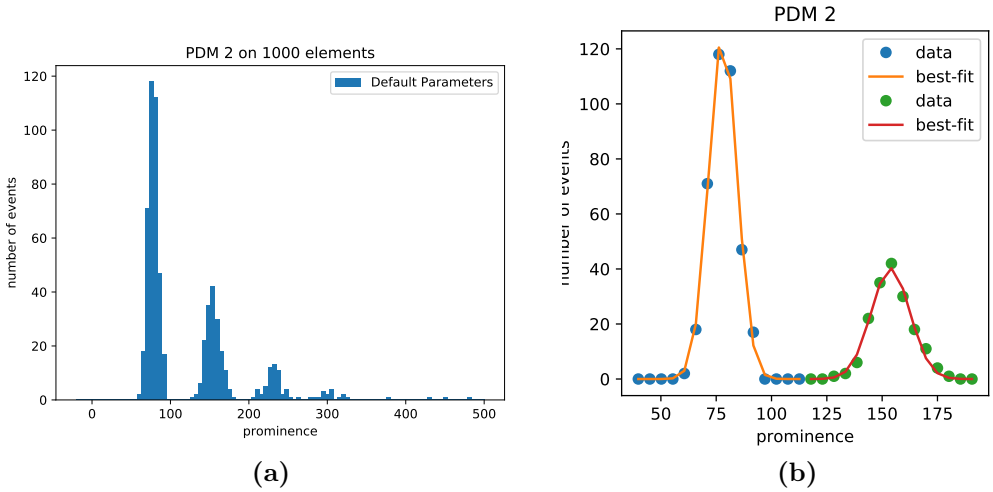

Figure 6.7. Prominence distribution (a) and gaussian fit to first peaks (b) to measure the gain, for channel 2. Fit results: $p_1 = 76.2 \pm 4.6$, $p_2 = 151.6 \pm 6.4$.

and the simulator generates 5000 waveforms with 0 pe, with $\sigma = 7.5$ ns, $\tau = 565$ ns, $fslow = 0.98$, $gate = 500$ μs. $snr = 1.7$ for the raw waveform simulated and such a low value is justified by the desire to best reproduce the snr of the waveform filtered in real data. (fig. 6.8).

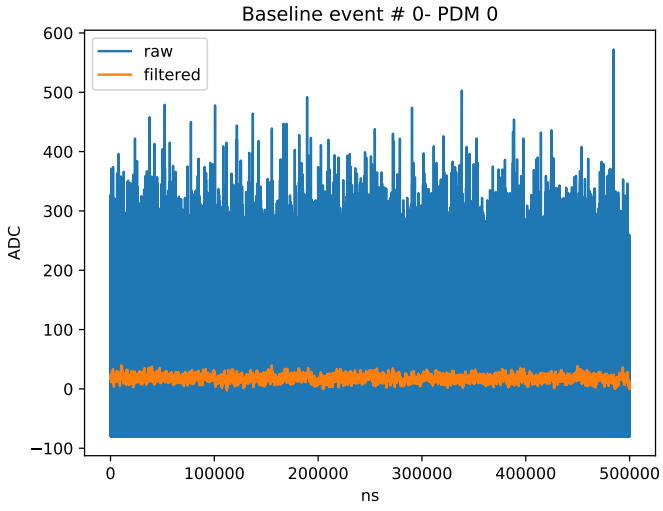

Figure 6.8. Baseline event simulated.

Each waveform is then filtered with σ, τ and $fslow$ of the simulator, then the RMS is measured: all RMS are histogrammed giving rise to the distribution of figure 6.9.a, which is finally fitted with a Gaussian (fig. 6.9.b) extrapolating the average value of the standard deviation. This quantity is used for all channels and all fit methods.

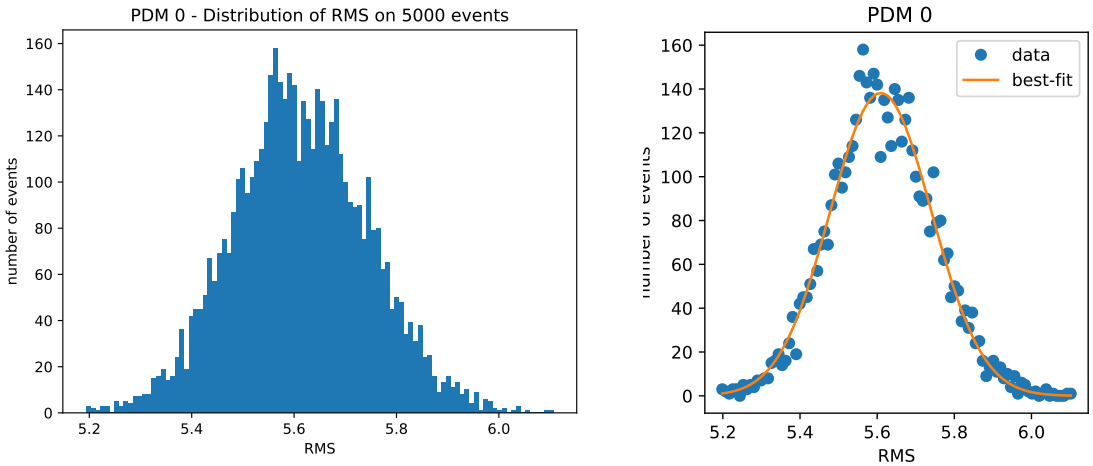

(a) (b)

Figure 6.9. RMS distribution (a) and gaussian fit (b) to measure the mean value of the standard deviation. Fit parameters: $center = 5.62$, $\sigma = 0.15$

The SNR is calculated for each of the five filters. A further calculation is done by filtering the waveforms with the average parameters of the simulator. These measurements are plotted as a fuction of the channels id (fig. 6.10). Note that there is no relevant difference between filters initialized with different templates. This observation, combined with the trend of SNR values, allows us to affirm that the five fit procedures give consistent results with the MC simulation that describes the truth, confirming the validity of this implemented methods.

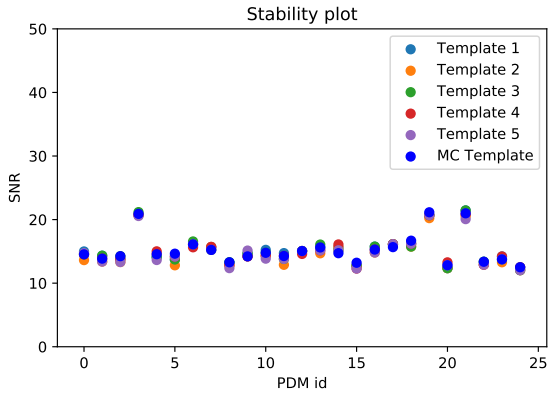

Figure 6.10. SNR vs channel id, comparing the five filters plus the one using simulator parameters.

6.3 Discrimination between subsequent hits

MC simulation is very useful for investigating the peak resolution efficiency of the peak finder. The question that arises is what is the minimum distance between two consecutive peaks so that they are correctly identified.
Two identical peaks are generated, with $\sigma = 8.8$ ns, $\tau = 480$ ns, $fslow = 0.98$, both due to a single pe. The gate of an event is 8 μs. The first peak is always generated at the time of 1 μs while the second is simulated at a random distance in the range 0 - 1 μs. Each waveform is filtered with the same template parameters as the simulator and the hits are reconstructed by the peak finder set with $height = 40$, $prominence = 10$, $distance = 1$ and $width = 1$ (fig. 6.11).

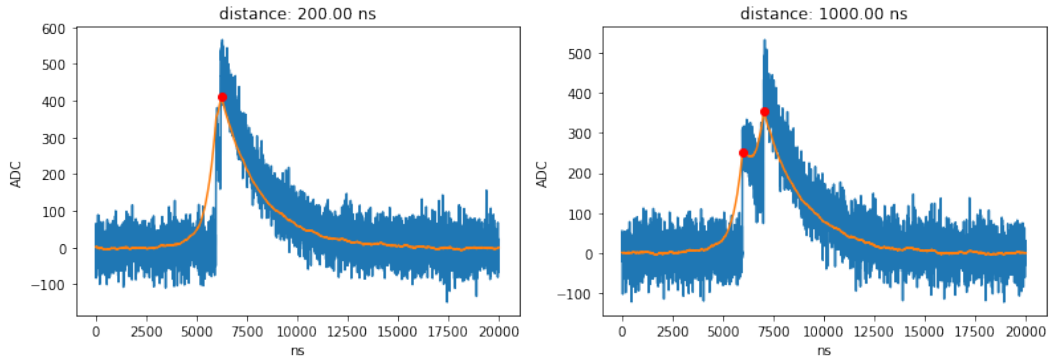

(a) **(b)**

Figure 6.11. Waveforms with peaks at small (a), and large (b) distances, with hits reconstructed by peak finder: in the first case peaks are too close each other and the reconstruction is hard, differently from the case of long distance.

When the peak finder identify an hit also measures its position, therefore we want to understand how well this reconstruction takes place when two peaks are very close to each other. 1000 waveforms are simulated. For each event the distances are measured with the algorithm, the reconstructed distances are saved, then the results fill an histogram which is compared with that of the real distances (fig. 6.12). The curve in red superimposed in the same figure is the bin to bin ratio between the histogram of the reconstructed distances and that of the real distances, and represents the efficiency curve of the time resolution of the peak finder: it is observed that when the peaks are very close to each other the algorithm hardly finds the hits and the efficiency is very low, but as the reciprocal distance increases, the impulses are distinguished more precisely and the efficiency grows up to stabilize at 1 for large distances, index of the maximum precision of the peak finding algorithm.

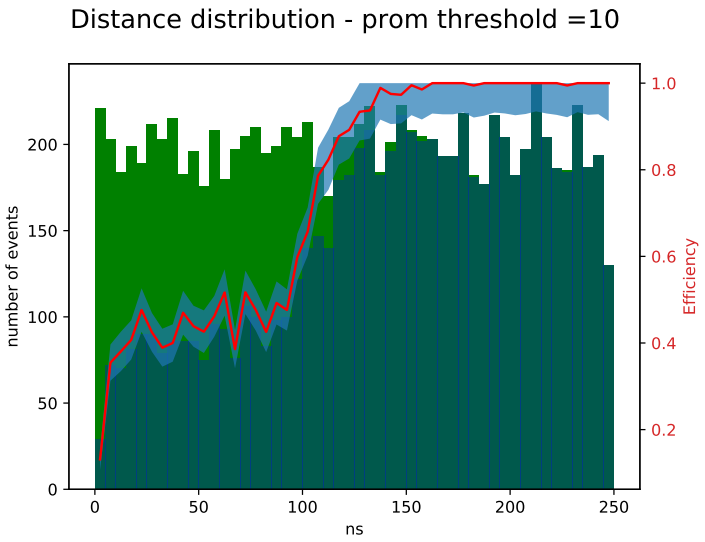

Figure 6.12. Distribution of true and reconstructed distances: for small distances much less events are reconstructed.The red curve is the efficiency for time resolution of peak finder, obtained from bin to bin ratio of true and reconstructed distances histograms.

6.4 Efficiency for NR and ER

After determining the efficiency of the peak finder time resolution as a function of the distance between two consecutive peaks, the goal is now to investigate the efficiency of this algorithm in reconstructing hits for events with many pe.
Waveforms are simulated that resemble those produced by scintillation in the detector, i.e. with photoelectrons that follow the ER time distribution. The simulator is now initialized with the following parameters: $gain = 140$, $\sigma = 8.8$ ns, $\tau = 480$ ns, $fslow = 0.98$. For the moment the noise and the poisson fluctuation of the generated number of photoelectrons are off. The peak finder is setted with *height* $= 40$, *prominence* $= 10$, *distance* $= 1$ and *width* $= 1$. In figure 6.13 an example is shown: a waveform with 10 pe is generated and it is observed that the peak finder finds three peaks in the filtered waveform. The height of these peaks determines how many pe they represent. If the efficiency were 100% the height of the peaks would correspond to 10 pe.

To determine the correspondence between peak and number of pe it is necessary to convert the prominence into a number of photoelectrons. 10k events are simulated, with the poisson with average 1 pe on and the noise off, following the delta time distribution. Events in which there is no peak are excluded and peaks with prominence <50 are ignored because they are caused by noise. Thus the prominence distribution in figure 6.14.a is obtained. With a Gaussian fit we extract the gain, measured equal to 86.43 (fig. 6.14.b). Based on this, since the distance between the peaks should always be the same, it is possible to convert the prominence into a number of pe, as shown in the table (6.1).

The number of pe is calculated using the function **ceil**: $npe = ceil(\frac{prom-50}{80})$, which means that a certain number of pe actually corresponds to a range of prominence and that, although the peaks found are few, the sum of their heights returns

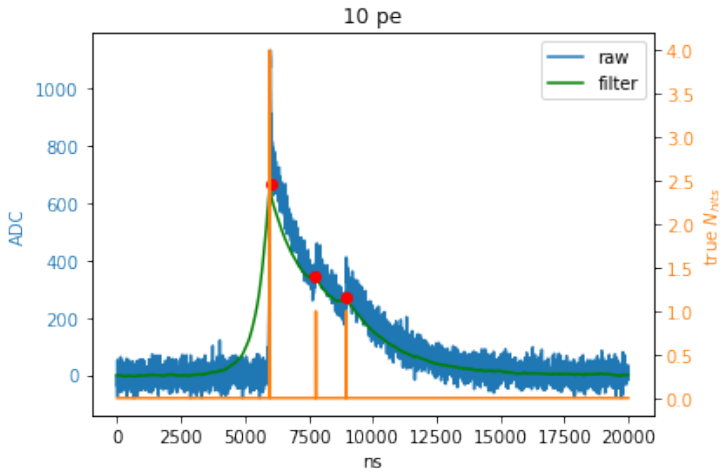

Figure 6.13. Waveform with 10 pe following ER time distribution: peak finder finds three peaks. There are two peaks of 4 pe at the same time.

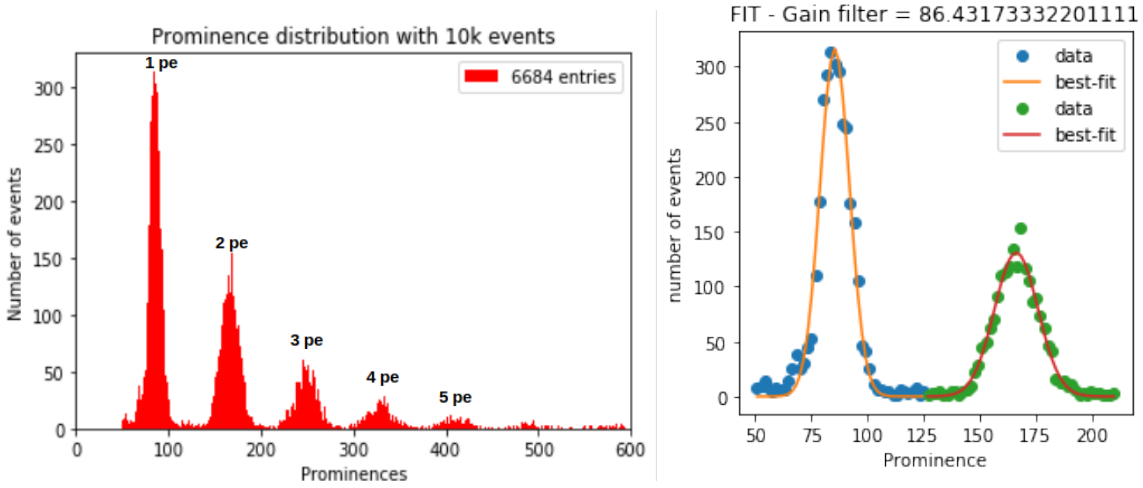

(a) (b)

Figure 6.14. Prominence distribution (a) and gaussian fit (b) to extract the gain.

npe	Prominence
1	86.43
2	172.86
3	259.29
4	345.72
5	432.15

Table 6.1. Conversion table between prominence (considered as the centre of the peak) and number of pe.

the number of pe.
At this point we want to know how well the peak finder can identify multiple peaks. As a preliminary operation we want to study the average number of pe reconstructed

for different values of pe in input: 50 ER events are simulated for each true number of pe, then the peak finder - with prominence threshold 10 - is applied and the number of reconstructed pe is plotted in function of the number of pe in input (fig. 6.15.a). If the plot obtained is normalized, you have a better idea of the efficiency of the peak finder (fig. 6.15.b). As could be expected, efficiency decreases with increasing number of pe in input, since the more pe there are in the event the more difficult it is to reconstruct them.

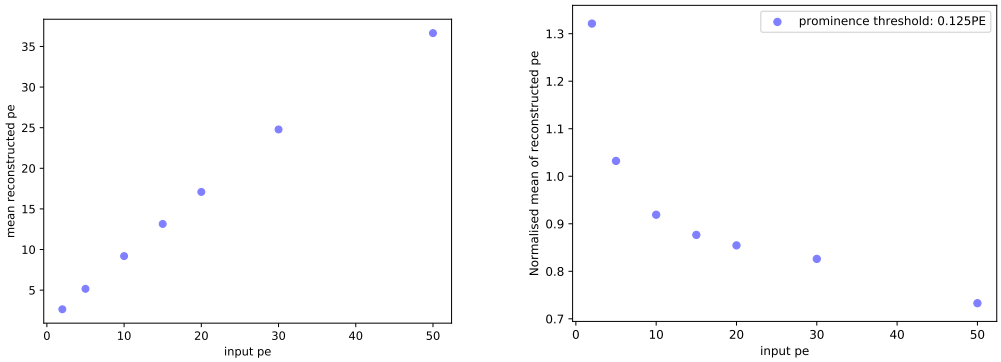

(a) **(b)**

Figure 6.15. Plot of number of reconstructed pe vs number of pe in input for different values (a) and the normalized plot to observe the efficiency of reconstruction (b): efficiency decreases with increasing number of pe in input.

The study conducted so far has been characterized by a prominence threshold of 10 to reconstruct the hits. It is expected that higher prominence values allow the reconstruction of a smaller number of peaks, while for smaller values they allow to find many more hits.
The next step is to investigate the effect of the prominence threshold on the peak finder efficiency for both NR and ER events. For this analysis, the following prominence values are considered: 55, 35, 25, 10, 5, 1. For each of these thresholds, for both ER and NR, 1000 events are simulated for different number of pe inputs. The waveforms are filtered and the number of pe is reconstructed, which is then averaged on the number of events. The average pe number is then normalized and plotted as a function of the number of pe input. Fig. 6.16 shows the two plots for ER and NR: it is noted that efficiency decreases with increasing prominence threshold (in number of pe), as expected. It is also observed that efficiency decreases more rapidly in the NR case than in the ER case: in the first case the photoelectrons are distributed with a much shorter characteristic time and the peaks will be closer and therefore it is more difficult to reconstruct them. This characteristic is seen mostly for low pe as for high values in both cases the reconstruction seems very hard. In DarkSide-20k $\sim$100 photoelectrons per PDM are expected, so it is very important to have high efficiency for high number of pe.

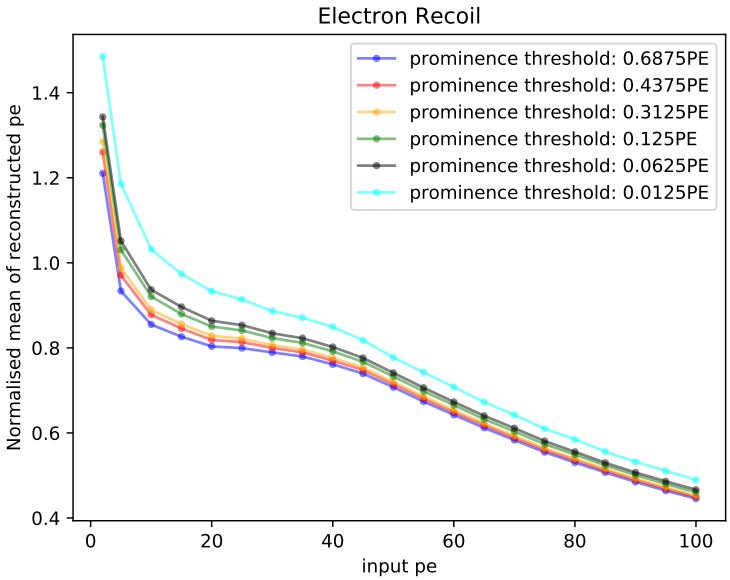

(a)

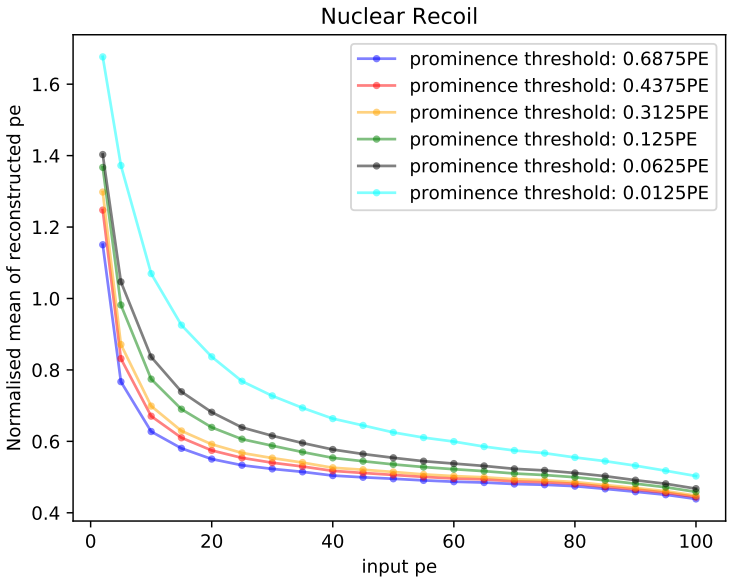

(b)

Figure 6.16. Reconstruction efficiency of peak finder for different prominence thresholds, for electron recoil (a) and nuclear recoil (b). Thresholds are expresser in number of pe, obtained by dividing prominence by gain.

Conclusions

This thesis focused on the study of the response of the silicon photomultipliers installed on the Proto-0 detector, currently located at CERN. Proto-0 is a small prototype of what DarkSide-20k will be, a detector designed for direct WIMP research equipped with a double phase TPC filled with argon that will take data from 2023 for a total exposure of 200 t yr for 10 years, mantaining an irreducible background level never achieved before (<0.1 events fot the total exposure). Proto-0 is actually a temporary and reduced version of DS-Proto, a prototype with a TPC containing $\sim$1 t of liquid argon which will be located at LNGS and it will aim to fully validate the new DS-20k technologies for their integrity in both the mechanical and functional aspects. During the DS-Proto preparation period, Proto-0 was projected to test the light response of the detectors with respect to the S_1 and S_2 signals, varying the TPC parameters such as the thickness of the gas pocket or the intensity of the external electric fields.
Proto-0 is characterized by the same design and the same materials foreseen for the future DS-20k. In particular, the prototype shares with DarkSide-20k the same type of light detectors used to detect liquid argon scintillation signals due to the interaction of particles with the target in the TPC. SiPMs are a revolution in this field thanks to their high radiopurity, their compactness and their great photon detection efficiency (PDE), so they make the pulse shape discrimination (PSD) technique already verified with DS-50 even more effective. Proto-0 is equipped with a MotherBoard consisting of 25 PDMs, in turn composed of 24 SiPMs each, positioned above the anode of the TPC. The study of the response of these detectors is of fundamental importance for their calibration, which will then be performed on DS-Proto and finally on DS-20k.
For this purpose, during my thesis period I different procedures to measure the SiPM template parameters and verify the effect they have on the algorithm used to filter the waveforms and reconstruct the events of physical interest. The proposed techniques proved similar performance in terms of stability of the fitted parameters response of the SiPM template, and in terms of SNR as evaluated comparing to a baseline run. By averaging the parameters between all the runs, a SNR vs PDM id plot is obtained in which the values measured from the five different configurations settle on the same trend as the unaveraged case and in addition the fluctuations are reduced. With regard to this study, it emerged that it does not matter which particular fit method is used to measure the parameters of the response of the SiPM: by averaging it, the filter is applied to the waveform in the exact same way. This is a very important result because it allows to speed up the analysis of data in real time compared to the acquisition, choosing the fastest fit method and averaging

it. In addition, it is a strategy that promises to be of great importance in terms of DS-20k, which will have thousands of PDM modules to be analyzed. This procedure was confirmed by the Monte Carlo simulation, through which laser-type events were generated, the same fit procedures were applied as seen with the data and the SNR was measured. The result obtained with the data was achieved by the simulation, thus confirming the validity of the work carried out.
Through the same Monte Carlo simulation the efficiency of the peak finder was studied from the point of view of temporal resolution and reconstruction of the number of pe by modifying the minimum prominence threshold as input to the algorithm. In the first case, by randomly varying the distance between two single pe laser-type peaks in the range of 1 μs, it emerged that the peak finder has difficulty in reconstructing the hits when their mutual distance is < 400 ns, while its efficiency increases up to 100% for longer distances. From the point of view of the reconstruction of the number of photoelectrons, ER and NR type events were generated, with the number of pe gradually increasing, varying the minimum prominence threshold of the peak finder: it emerged that for higher prominence values the algorithm reconstruction has a worse efficiency in identifying the correct number of pe compared to the number of pe in input to the simulator, while the efficiency increases with the decrease of the threshold. In all cases, however, it is true that for a low number of pe the efficiency is high while it decreases with the increasing of this number. In DarkSide-20k $\sim$100 pe per PDM are expected, therefore very high efficiency for high pe numbers is a crucial requirement.
The study of charge distributions and prominence in response to different filter settings, the calculation of gain and occupancy starting from these, the study of the dependence of the DCR on the bias voltage of the PDM and the observation of events with concurrent signals S_1 and S_2 have completed my work and allowed me to conduct the most in-depth analysis of the SiPM response of Proto-0 MotherBoard.
The next steps in the analysis of the response of the SiPM will concern the study of the resolution of pileup signals on PDMs, due to crosstalk and afterpulse, determining their dependence on the precise position of the modules on the MotherBoard. The Monte Carlo simulation will be very useful for this investigation.
Another important step will be developing hit-based recostruction clustering algorithms which can be used to identify S_1 and S_2-like pulses by an analysis of the total waveform (or the total hits in the case of the filtering algorithm) accross all PDM channels.
As anticipated, the prototype will be soon equipped with a second MotherBoard, according to the original design, in order to optimize the visibility of the S_2 signal: the S_2 pulse will be the subject of in-depth study in the future, investigating it along with different gas pocket configurations, aiming to provide us the best solution for the future LAr TPC design.
All these future applications will allow an even better characterization of the Proto-0 response of the SiPM, and they will improve the understanding we have with respect to the working of these detectors in order to make them definitively ready to operate in DS-20k and, why not, to observe one day a WIMP signal.

Bibliography

[1] Barbara Ryden, 2003, *Introduction to cosmology*, Pearson Addison-Wesley editor.

[2] *Researchers confirm EinsteinâĂŹs theory of relativity yet again*, https://sciexaminer.com/news/science/researchers-confirm-einsteins-theory-relativity-yet-5204.html,. https://sciexaminer.com/news/science/researchers-confirm-einsteins-theory-relativity-yet-5204.html

[3] Planck Collaboration. *âĂIJPlanck 2018 results. VI. Cosmological parameters.*

[4] Edward W. Kolb and Michael S. Turner. *The Early Universe*. Reading, Massachusetts: Addison-Wesley, Feb. 1990. Chap. 9.

[5] George R. Blumenthal et al. *Formation of galaxies and large-scale structure with cold dark matter*. In: Nature 311.5986 (Oct. 1984), pp. 517âĂŞ525.

[6] Volker Springel et al. *Simulations of the formation, evolution and clustering of galaxies and quasars*. In: Nature 435.7042 (June 2005), pp. 629âĂŞ636.

[7] M. Vogelsberger et al. *Properties of galaxies reproduced by a hydrodynamic simulation*. In: Nature 509.7499 (May 2014), pp. 177âĂŞ182.

[8] Pol Mollitor, Emmanuel Nezri, and Romain Teyssier. *Baryonic and dark matter distribution in cosmological simulations of spiral galaxies*. In: (May 2014).

[9] David Tytler et al. *Review of Big Bang Nucleosynthesis and Primordial Abundances*. In: Physica Scripta T85.1 (Jan. 2000), pp. 12+.

[10] Brian Fields and Subir Sarkar. *Big-Bang nucleosynthesis (Particle Data Group mini-review)*. In: J. Phys. G. 33.1 (Oct. 2006), pp. 1âĂŞ1232.

[11] Michele Maggiore. *Gravitational Wave Experiments and Early Universe Cosmology*. In: Phys. Rep. 331.6 (Feb. 2000), pp. 283âĂŞ367.

[12] Richard H. Cyburt et al. *New BBN limits on Physics Beyond the Standard Model from He4*. In: J. Astropart. Phys. 23.3 (Aug. 2005), pp. 313-323.

[13] Karsten Jedamzik. *Big Bang Nucleosynthesis Constraints on Hadronically and Electromagnetically Decaying Relic Neutral Particles*. In: Phys. Rev. D 74.10 (Nov. 2006), p. 103509.In: Phys. Rev. D 74.10 (Nov. 2006), p. 103509.

[14] . *Lezioni di Materia Oscura*, Dottorato a.a. 2014-2015, A.Pullia (Parte Sperimentale).

[15] V. Chepel and H. Araujo, *Liquid noble gas detectors for low energy par- ticle physics*, In: JINST 8 (2013), R04001. doi: 10.1088/1748-0221/8/ 04/R04001. arXiv: 1207.2292 [physics.ins-det].

[16] The DarkSide Collaboration. *DarkSide-20k: A 20 Tonne Two-Phase LAr TPC for Direct Dark Matter Detection at LNGS*. Submitted: July 27, 2017.

[17] P. Agnes et al. *Phys. Lett. B 743, 456 (2015).*

[18] P. Agnes et al. *Phys. Rev. D 93, 081101 (2016a).*

[19] T. Alexander et al. *Astropart. Phys. 49, 44 (2013a).*

[20] Jaco de Swart, Gianfranco Bertone, Jeroen van Dongen, 16 Maggio 2017, *How Dark Matter Came to Matter*

[21] Paolo de Bernardis *Corso di Astrofisica*, a.a. 2016/2017

[22] Elena Aprile, 2009, *Direct Dark Matter Searches: Lecture 1- 2*

[23] Abdelhameed, A.H., Angloher, G., Bauer, P. et al, *First results on sub-GeV spin-dependent dark matter interactions with ^7Li*, Eur. Phys. J. C 79, 630 (2019). https://doi.org/10.1140/epjc/s10052-019-7126-4.

[24] Jianglai Liu 1 , Xun Chen 1 and Xiangdong Ji, *Current status of direct dark matter detection experiments.*

[25] S.Focardi, I.Massa, A.Uguzzoni, M.Villa, *Fisica Generale, meccanica e termodinamica*, II edizione

[26] Matteo Cadeddu, *DarkSide-20k sensitivity, directional dark matter detection and the role of coherent elastic neutrino-nucleus scattering background*, PhD degree, Final exam. Academic Year 2016-2017. Thesis defence: February-March 2018 Session.

[27] The DarkSide Collaboration. *DarkSide-20k: A 20 Tonne Two-Phase LAr TPC for Direct Dark Matter Detection at LNGS*. Submitted: July 27, 2017.

[28] *Direct Search for Dark Matter with the DarkSide expeeriment*, Paolo Agnes.

[29] *Snowmass CF1 Summary: WIMP Dark Matter Direct Detection*, Priscilla Cushmann.

[30] *Studio e calibrazione dello spettrometro per neutroni dellâĂŹesperimento red per lo studio di scattering di neutroni su argon liquido.*

[31] *Introduction to SiPM*, Advanced Silicon Detectors.

[32] *Introduction to Silicon Photomultiplier*, Technical Note, SenseLight.

[33] *SiPMs for cryogenic temperature*, DarkSide Collaboration, 1 Apr 2019.

[34] The Global Argon Dark Matter Collaboration, *DarkSide-20k Technical Design Report*. Submitted: 21 Jan 2020.

[35] *Ligh Detection in DarkSide-20k*, F.Carnesecchi, 2020.

[36] *K-SiPM (SiPM at cryogenic temperatures*, M.Garbini, Centro Fermi.

[37] https://$drive.google.com/drive/folders/1zyvoPcPw$ – $r4FvfJa6wNZGYWX_fw5uEjx$, Yi Wuang.

[38] https://www.caen.it/products/v1725/ .

[39] *Americium-241*, Wikipedia.

[40] *http://midas.triumf.ca.*

[41] *Peak Finder Efficiency*, Sam Hill, Paolo Agnes.

[42] *Dark matter search with liquid argon inDarkSide: results with scientific andtechnological prototypes*, Bianca Bottino.

[43] *Source related info*, Yi Wang, Hanguo Wang.

[44] https://twiki.cern.ch/twiki/bin/view/Sandbox/DarkSideProto0 , DarkSide Proto-0 Operations.